

Electronic Detection of Molecules on the Exterior and Molecular Transport through the Interior of Single Walled Carbon Nanotubes

by

Chang Young Lee

M.S., Chemical Engineering
University of Illinois at Urbana-Champaign, 2007

B.S., Chemical Engineering
Seoul National University, Republic of Korea, 2003

Submitted to the Department of Chemical Engineering
in Partial Fulfillment of the Requirements for the Degree of

DOCTOR OF PHILOSOPHY IN CHEMICAL ENGINEERING

at the

MASSACHUSETTS INSTITUTE OF TECHNOLOGY

February 2010

© 2010 Massachusetts Institute of Technology. All rights reserved.

Signature of Author: _____

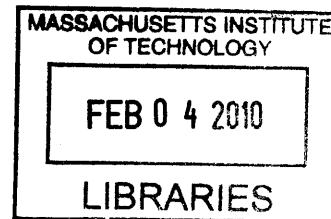
Department of Chemical Engineering
December 1, 2009

Certified by: _____

Michael S. Strano
Professor of Chemical Engineering
Thesis Advisor

Accepted by: _____

William M. Deen
Professor of Chemical Engineering
Chairman, Committee for Graduate Students



ARCHIVES

Electronic Detection of Molecules on the Exterior and Molecular Transport through the Interior of Single Walled Carbon Nanotubes

by

Chang Young Lee

Submitted to the Department of Chemical Engineering
on December 1, 2009 in Partial Fulfillment
of the Requirements for the Degree of
Doctor of Philosophy in Chemical Engineering

Abstract

Single walled carbon nanotubes (SWNT) are unique materials with high surface to volume ratio and all atoms residing on the surface. Due to their tubular shape both exterior and interior of the SWNT are available for interaction with other molecules. One-dimensional electronic structure of SWNT is readily disrupted even by a single molecular binding event. Hence, one of the promising SWNT applications has been sorption-based sensors utilizing the exterior. Conversely, the interior of SWNT can potentially be used as a frictionless molecular conduit due to graphitic surface where molecular corrugation is minimized by high density of atoms. However, only few experimental results on the interior exist due to difficulties in designing a reliable platform.

For the first part of this work we aim to utilize the SWNT exterior for reversible detection of nerve agents. Vast majority of the SWNT sensors exhibit irreversible sensor responses. The irreversibility is a major cause of sensor failure and also limits long term operation of the sensor. We show for the first time 1) the irreversible-to-reversible transition via simple surface amine chemistry, 2) integration with a micro-fabricated gas chromatographic (GC) column for selectivity. The platform benefits from the reversible SWNT sensor as well as from the separation capability of the GC, an analytical standard for the detection of diverse classes of organic molecules.

For the second part, we demonstrate first time experimental monitoring of *individual* ions translocating through the *interior* of the single walled carbon nanotube. By analyzing pore-blocking events caused by ions, we report for the first time 1) high ionic mobility through the SWNT interior, 2-3 orders of magnitude higher than the bulk mobility, 2) proton conductivity of $\sim 10^3$ S/cm through the SWNT interior, 4 orders of magnitude higher than the Nafion proton exchange membrane and the highest ever reported, 3) proton/alkali ion separation factor of $\sim 6 \times 10^7$, 4) evidence of stochastic resonance in SWNT ion channels.

Thesis supervisor: Michael S. Strano
Title: Professor of Chemical Engineering

*To my father and mother
To Jinju*

Acknowledgement

Without help from my friends, colleagues, and family, I wouldn't have been able to go through all the ups and downs during my 6.5 years of Ph.D. study.

First of all, I would like to thank my thesis advisor, Professor Michael Strano, for his constant help and encouragement throughout my study. He was not actually my first choice when deciding my thesis advisor back in 2003, but I was *luckily* very unfortunate enough to be assigned to his group. As a shy and quiet person who had rarely made any sound in English, being a part of a young and active research group was just a blessing. Discussion with him has been always fun and encouraging, especially when I was spinning wheels in frustration. He is a brilliant scientist as well as a well-rounded engineer, and his enthusiasm and energy have always motivated me so I work too much. Without him I wouldn't have enjoyed my research as much. Especially, the early days of my graduate life, during which we used to test gas sensors together and hug each other when things worked, will stay forever as good memories which I would like to pass on to my students (if I get to have my own research group) in the future.

I would also like to thank my thesis committee members at MIT, Professors Swager and Gleason, for their useful comments from different perspectives during the committee meetings. I would like to give special thanks to Professor Swager for supporting me during my post-doc and fellowship searches even if he has known me only for a short time period, and also for actually reading through my thesis and sharing his insight as a chemist.

I appreciate help from faculty members in Seoul National University, Seung Jong Lee, Jong-Chan Lee, and Hyun-Ku Rhee for allowing me to study in United States. Advice and guidance from Professor Kookheon Char during his short visit to MIT are also appreciated.

For unknown reasons only nice people joined our lab. They were cheerful all the time and just sitting or standing by them kept me happy. I am especially very grateful to early members of the group who spent nice old days at UIUC with me: Paul Barone, Monica Usrey, Esther Jeng, Rachel Graff, Daniel Heller, and Nitish Nair. Watching movies and football, going to conferences, playing Frisbee as well as working in the lab were all exciting and unforgettable. I would like to express my gratitude to Richa Sharma, who sat right next to me, for sharing all the small but enjoyable moments with me for the past 4 years. Help and support from the other members of the group, Hong Jin, Joel Abrahamson, Arde Boghossian, Geraldine Paulus, Andrew Hilmer, and Dr. Rajaseker are appreciated as well. I would like to thank Jingqing Zhang for organizing a farewell party so I spend another but obviously not final great moment with everyone above.

I absolutely have no idea how to express my gratitude to all the Koreans in our group. I was so lucky to be with them in the same group. Whatever I do inside/outside the lab, I was never alone and felt always supported by them. I would like to thank Seunghyun Baik for his guidance and patience while I was in total frustration and had no interest in research, Woo-Jae Kim, Jong Hyun Choi, Jae-Hee Han (and his family), Joon Hyun Baik, and Jong Ho Kim for being always supportive and taking care of me like their little brother, Taeyun Kwon for his constant encouragement and help with shaping my future, Changsik Song, Hyeonseok Yoon, and Jin-Ho Ahn for being good friends,

Moon-Ho Ham for nice discussion/conversation and help with lab chores and research, Wonjoon Choi for taking over my work so I graduate and also for helping with my everyday life, Sang Wook Kang for all the cheerful moments, and finally Byung-Seon Kong and Youn-Kyoung Baek for their kind wishes and support from Korea.

I wouldn't have overcome hardships for the first a few years of my Ph.D. study without encouragement from my friends at Illinois: Chang Yong Park, Sun Wook Kim, Sangeun Bae, Sungkyung Lee, Jae-Sung Moon, Kihyuck Kim, Jang-Ung Park, Eugen Mandrila, and Anthony Yew. Advice from my spiritual mentor, Hyeonseong Snim, is also appreciated.

Finally, my family...Without my parents' absolute trust and unconditional love, support, and devotion, I would not have accomplished anything in my life, and any of my accomplishments including the Ph.D. degree would have been meaningless. Help of my elder brother in Korea is also appreciated. He has encouraged me throughout my life, and taken care of all the family issues while I am away from home so I can focus on study. I would like to thank my wife, Jinju Kang, a recent addition to my life, for her patience and constant encouragement/support for the past 2 years of long distance relationship. I am also grateful to her parents in Korea for their care and support.

Table of Contents

Acknowledgement.....	4
Introduction	8
Chapter 1. Single walled carbon nanotubes (SWNT)	8
1.1. Basic structure.....	8
1.2. Electrical properties	10
Chapter 2. SWNT assembly on a surface.....	11
2.1. AC dielectrophoresis.....	12
2.2. Membrane transfer	13
2.3. Chemical vapor deposition: direct growth on a substrate.....	16
Part I. Exterior of single walled carbon nanotubes for reversible detection of nerve agents.....	20
Chapter 1. Introduction to single walled carbon nanotube gas sensors .	20
Chapter 2. Understanding the dynamics of signal transduction.....	22
2.1. Case I: Irreversible adsorption	22
2.2. Case II: Reversible adsorption	25
2.3. Application to literature data	28
Chapter 3. Charge transfer from metallic SWNT sensor arrays	32
3.1. Extracting the kinetic properties from the response	32
3.2. The role of electrode-nanotube contact in sensing	37
3.3. Charge transfer from large diameter metallic SWNT.....	38
3.4. Mechanism and modeling	40
3.5. Electrical transport measurement.....	42
3.6. Regeneration via analyte hydrolysis	43
3.7. Experimental	45
Chapter 4. Chemically tuning the molecular adsorption.....	48
4.1. Amine-functionalization tunes the reversibility.....	48
4.2. Conditions for reversible sensors.....	53
4.3. Sensing mechanism.....	58
4.4. Polymer coating for enhanced sensitivity	62
4.5. Application of reversible sensors: integration with μ GC column	64
4.6. Experimental	66
Part II. Interior of single walled carbon nanotubes for single molecule transport.....	69
Chapter 1. Background.....	69

1.1. Nanopore resistive sensing	69
1.2. Stochastic resonance	73
1.3. SWNT as a molecular transporter.....	76
Chapter 2. Preventing exterior transport of ions	80
2.1. Evidence of molecular transport on SWNT.....	80
2.2. Evidence of exterior molecular transport on SWNT	83
2.3. Problems caused by exterior transport of ions.....	84
Chapter 3. Interior transport of ions: stochastic resonance in SWNT ion channels	87
3.1. Reliable experimental platform for the study of interior transport	87
3.2. Interior transport of individual ions	90
3.3. Ion current oscillation due to rhythmic transport of ions.....	94
3.4. Understanding the current oscillation: stochastic resonance	101
Conclusion	108
References	111

Introduction

Chapter 1. Single walled carbon nanotubes (SWNT)

Single walled carbon nanotube (SWNT) is a 1 dimensional tubular carbon material with diameter of only 1-2 nm and length as long as several cm. SWNT was first discovered by Iijima group¹ in 1993 using high resolution transmission electron microscope (HRTEM). They were also the first to access the interior of the tubes by demonstrating that multi-walled carbon nanotubes can be opened and filled with molten materials.² Early theoretical studies predicted that the SWNT could be either metallic or semiconducting depending on the orientation of hexagonal lattice relative to the tube axis.³⁻⁵ This prediction was experimentally verified for the first time in 1998 using scanning tunneling microscopy (STM).^{6,7} Field effect transistor with on/off current ratio of $\sim 10^6$ can be fabricated using semiconducting nanotubes.^{8,9} With its high carrier mobility, chemical and physical stability, and mechanical flexibility, SWNT can potentially replace the silicon and contribute to extend the Moore's law.¹⁰ Metallic nanotubes have been considered as interconnects between electronic devices or transparent electrodes with low sheet resistance which can replace the brittle indium tin oxide (ITO) electrodes.^{11,12} Recently many researchers turn their attention to energy applications such as photovoltaic solar cells where the efficiency higher than the thermodynamic limit can possibly be achieved by generating multiple electron-hole pairs.¹³ SWNT also provides ample spectroscopic information such as strong Raman scattering¹⁴ and near-IR band-gap fluorescence¹⁵, both of which have been heavily utilized not only for SWNT characterization after chemical/physical treatment^{16,17} but for optical labeling¹⁸ and sensing^{19,20}.

1.1. Basic structure

The structure of SWNT is most easily described as a rolled-up graphene sheet as shown in Figure 1a. Graphite is a 3D material with stacks of 2D graphene sheets. By rolling up a single graphene sheet we can conceptually form a single walled carbon nanotube. Most of the structural, optical, electrical, chemical, and mechanical properties of SWNT are determined by how the graphene sheet is rolled up. Figure 1b shows a

honey comb lattice of a graphene sheet. All the points in the lattice can be described as a linear combination of two vectors \mathbf{a}_1 and \mathbf{a}_2 . The sheet can be rolled up into a SWNT by connecting two points (0,0) and (n,m). The chiral vector \mathbf{C}_h with chiral angle θ is defined.

$$\mathbf{C}_h = n\mathbf{a}_1 + m\mathbf{a}_2$$

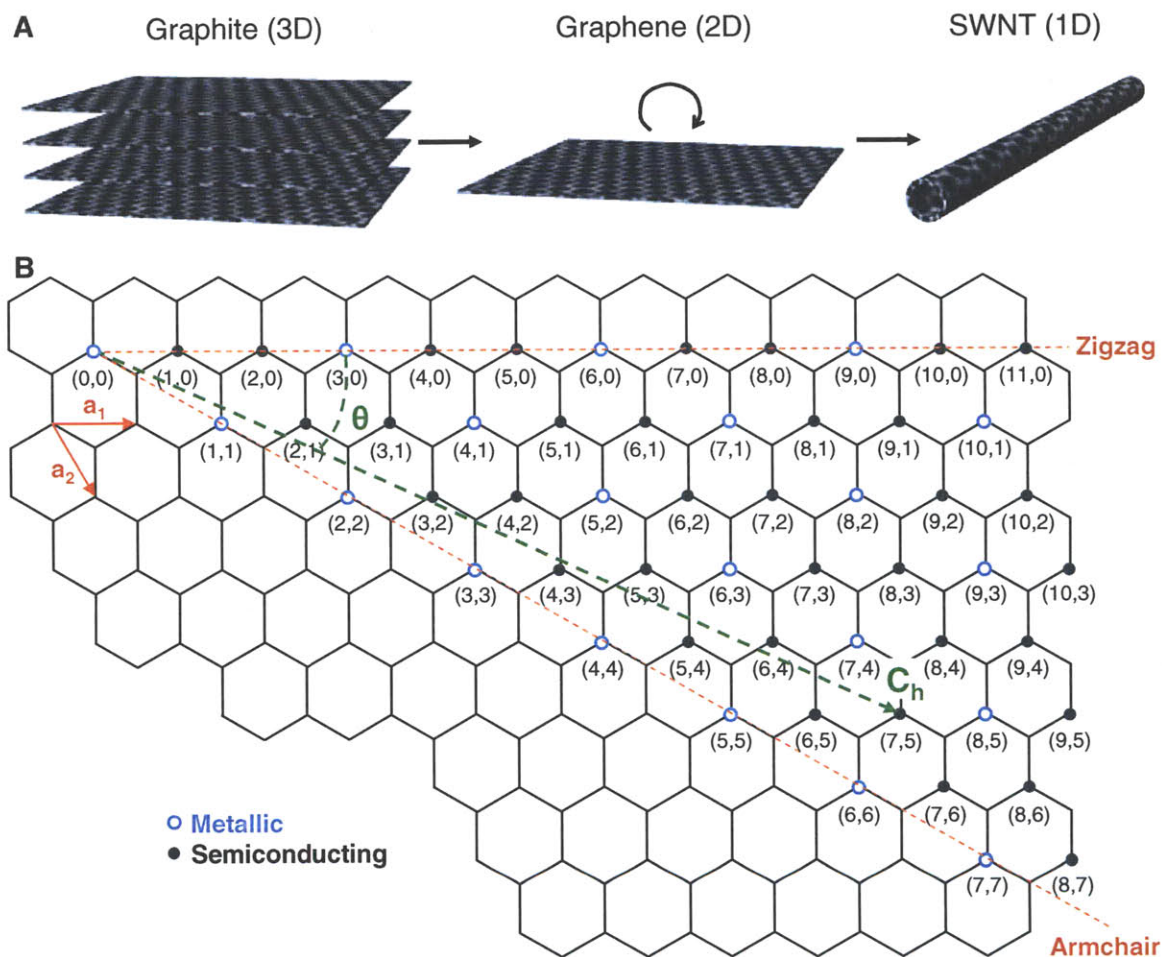


Figure 1. Formation and structure of single walled carbon nanotubes. a) Single sheet of graphene from graphite is rolled up into a tube to form a single walled carbon nanotube. b) Graphene lattice. A chiral vector, $n\mathbf{a}_1+m\mathbf{a}_2$, determines the structure and properties of SWNT.

Vectors (n,0) and (n,n) represent zigzag and armchair nanotubes, respectively. Diameter, d, of the SWNT defined by \mathbf{C}_h is,

$$d = \frac{\sqrt{3}}{\pi} a_{C-C} \sqrt{n^2 + nm + m^2} = \frac{C_h}{\pi}$$

where a_{C-C} is carbon-carbon bond length (=1.42Å). The chiral angle can be calculated by

$$\theta = \tan^{-1} \left(\frac{\sqrt{3}n}{2m+n} \right)$$

For the armchair nanotubes (n,n) the chiral angle is 30°. The chiral angle for the zigzag nanotubes (n,0) is 60°. Considering the symmetry, we can limit the angle between 0° and 30°, and therefore $\theta=0^\circ$ for the zigzag.⁵

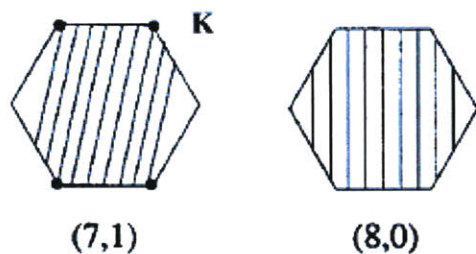
1.2. Electrical properties

Graphene is a zero band gap semiconducting material whose valence (π) and conduction (π^*) bands meet at K points in Brillouin zone. When the graphene is rolled up into a tube with (n,m) chiral vector, the periodic boundary condition allows only quantized wave vectors in the circumferential direction. The spacing between the neighboring cutting wave vectors and the length are determined by K_1 and K_2 , respectively.²¹

$$|K_1| = 2/d$$

$$|K_2| = 2d_R/\sqrt{3}d$$

where d_R is the greatest common divisor of $2m+n$ and $2n+m$ for (n,m) SWNT. When the cutting lines of a (n,m) SWNT pass the K points in Brillouin zone, the SWNT is metallic. If the K points are located between two cutting lines, the (n,m) nanotube is semiconducting. Examples are shown below for metallic (7,1) and semiconducting (8,0) SWNT (from Dresselhaus et al.²¹)



General rules to determine the electronic type for (n,m) nanotubes are, 1) (n,n) armchair nanotubes are always metallic, 2) (n,m) nanotubes with $n-m=3p$ (p: non-zero integer) are tiny-gap semiconductors, and 3) (n,m) nanotubes with $n-m \neq 3p$ are large-gap semiconducting. The tiny-gap in 2) is opened up due to curvature effect, but in practical situations the tiny-gap semiconductors with $n-m=3p$ are considered as metals at room temperature. Due to its symmetric structure the (n,n) SWNT is always metallic regardless of curvature. The band gap for the large-gap semiconducting nanotubes scales with $1/d$.

Chapter 2. SWNT assembly on a surface

SWNT are hydrophobic but can be easily suspended individually in water using surfactants²², polymers²³, or even DNA²⁴. Photoluminescence from semiconducting nanotubes has been used both to identify (n,m) species and to characterize the tubes after chemical treatment performed in solution.²⁵ A wide spectra from various (n,m) species also enables applications of the SWNT aqueous suspension in optical cell-labeling¹⁸ and biosensing²⁶. However, for many other applications such as in electronics or when mechanical robustness is required, nanotubes must be assembled on a substrate. There have been numerous reports on how to deposit nanotubes on substrates. Drop-drying the suspension on a substrate is an easy option although the array suffers from large aggregation and non-uniform surface coverage. The most common approach is to treat silicon or glass substrates with self-assembled monolayer (SAM) of amines^{27,28} on which the SWNT with negatively charged surfactants are assembled. An aligned array can be obtained by spinning the substrate during the assembly process²⁸, and patterning/aligning the array is possible via deposition on a pre-patterned SAM²⁹. Flowing gas during the deposition aligns the array along the direction of the gas.^{30,31} Nanotubes in a blown bubble can be also aligned as shown by Lieber group.³² In this chapter, I will discuss two

techniques that are relevant to our study: AC dielectrophoresis³³ and direct growth on a substrate by chemical vapor deposition³⁴.

2.1. AC dielectrophoresis

Depending on the surfactants used to suspend the nanotubes charges on the SWNT can be negative, positive, or neutral. As mentioned above amine-treating the substrate works only with negatively charged SWNT, and mechanical methods such as gas flow or spin-coating does not allow deposition on a desired region on the substrate (i.e. across electrodes for electronic applications). Therefore, it is important to have a deposition technique which works regardless of the SWNT charges, and allows assembly on a specific location.

AC dielectrophoresis³³ uses dielectrophoretic force shown below to separate/assemble particles suspended in solution according to their dielectric constant with respect to the dielectric constant of the solvent.

$$\vec{F} \sim \epsilon_{\text{solvent}} \frac{\epsilon_{\text{tube}} - \epsilon_{\text{solvent}}}{\epsilon_{\text{tube}} + 2\epsilon_{\text{solvent}}} \nabla E_{\text{rms}}^2$$

The Clausius-Mossotti (C-M) factor³⁵, $(\epsilon_{\text{tube}} - \epsilon_{\text{solvent}})/(\epsilon_{\text{tube}} + 2\epsilon_{\text{solvent}})$, determines the sign of the force. ϵ_{tube} and $\epsilon_{\text{solvent}}$ are frequency-dependent dielectric constants of the nanotube and the solvent, respectively. $\epsilon = \epsilon_d - j(\sigma/2\pi f)$ where ϵ_d , σ , and f denote dielectric constant, conductivity, and frequency, respectively. E_{rms} represents the AC electric field. Note that the force is independent of the charge of the particle, and is only a function of dielectric constant, frequency, and electric field. When the applied frequency is higher than the cross over frequency ($f > f_c$), the C-M factor is positive meaning that the particle experiences positive (attractive) force toward high electric field. When a droplet of nanotube suspension is place across electrodes, nanotubes are aligned along the electric field and deposited across the electrodes, making an electrical connection between the electrodes (Figure 2). Using the technique, researchers have fabricated devices including field effect transistors^{36,37} and gas sensors^{38,39}. Krupke et al.³³ showed that preferential deposition of metallic nanotubes occurs due to high dielectric constant of metallic

SWNT. The finding can be used to separate nanotubes by their electronic type. Recently Shin et al.⁴⁰ demonstrated that the technique is scalable using continuous microfluidic separation.

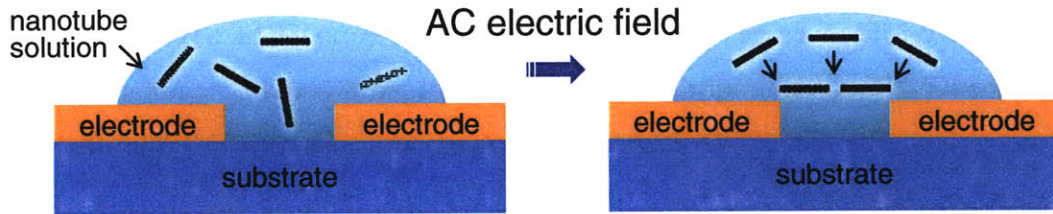


Figure 2. SWNT deposition using AC dielectrophoresis. SWNT suspension is dropped between electrodes. When AC field is applied, nanotubes are aligned along the electric field and attracted to the electrodes.

2.2. Membrane transfer

Since the deposition takes place only where the electric field is applied, the dielectrophoresis is not desirable when the deposition on a large area with uniform coverage is required. Membrane transfer⁴¹ can be an option in this case. The procedure is shown in Figure 3. First step is to make a nanotube film by vacuum-filtering SWNT suspension through a membrane filter (alumina, cellulose acetate, etc.) with small pore size (25 nm - 500 nm). Next, the film is transferred onto a substrate. The transfer procedure varies depending on the porous membrane: 1) dissolve the membrane filter and pick up the floating SWNT film with a receiving substrate, or 2) transfer the whole SWNT film and membrane onto a substrate and then dissolve the membrane.

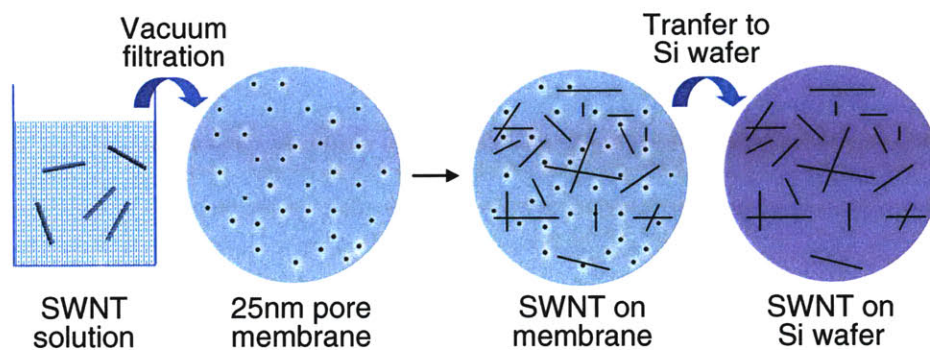


Figure 3. Membrane transfer technique. SWNT suspension filtered through a small-pore membrane is transferred onto a substrate to form a uniform network.

There are several advantages of the membrane transfer. First of all, it is easy to scale up without increase in processing time by simply using a large membrane filter. Secondly, SWNT coverage can be easily controlled. Amount of SWNT per unit area equals the SWNT concentration in suspension \times volume filtered / membrane area. Third advantage is the uniform SWNT coverage over an entire film. SWNT flux through low coverage regions of the membrane filter is higher than the high-coverage regions so the coverage is constantly adjusted and remains uniform.

Figure 4 shows SEM images of SWNT films made by the membrane transfer technique. SWNT prepared by laser ablation method are suspended in water using sodium cholate surfactant. The suspension was then filtered through a mixed cellulose acetate membrane. SWNT side of the filtered membrane was then contacted with a receiving silicon substrate at 70 °C for an hour. Dissolving the membrane in acetone leaves a SWNT film transferred onto the substrate. As shown in Figure 4a, coverage is fairly uniform over large area, and it is clear that SWNT networks made by filtering the same volume at 10x (left) and 100x (right) dilution differ in coverage.

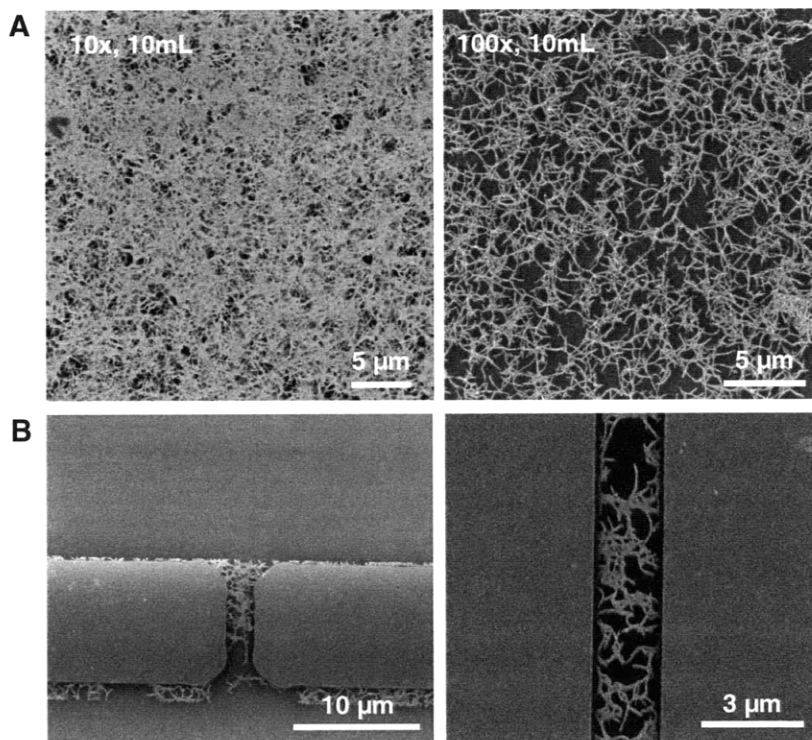


Figure 4. SWNT network prepared by the membrane transfer technique. a) SWNT coverage can be controlled by changing the amount of the filtered SWNT. Network on the right is made using 10 times less SWNT. b) Electrodes patterned onto the network (left), and zoomed in gap region (right).

We can make electrical connection between two electrodes using this SWNT network. Figure 4b (left) shows electrodes patterned above the SWNT film. SWNT outside the electrode region are etched using oxygen plasma. Shown on the right is a zoomed-in image of the gap. The device can find applications in electronics once the electrical connections are made above percolation threshold, which can be controlled by varying the SWNT coverage and the electrode gap size. Figure 5a show transfer characteristics of a field effect transistor made by the technique. The device has 10 μm -gap electrodes patterned on a network of HiPco⁴² SWNT. The device turns on at negative gate bias, suggesting that nanotubes in the network are p-doped. On/off current ratio is $\sim 10^3$. The technique can be also used for gas sensors. Figure 5b is a current response to nitrobenzene vapor from a network of SWNT prepared by laser ablation. Interdigitated electrodes are used to increase the active sensing area for analyte adsorption. The

resonances is negative and reversible. As shown in these examples, the technique works with various types of nanotubes to fabricate useful electronic arrays.

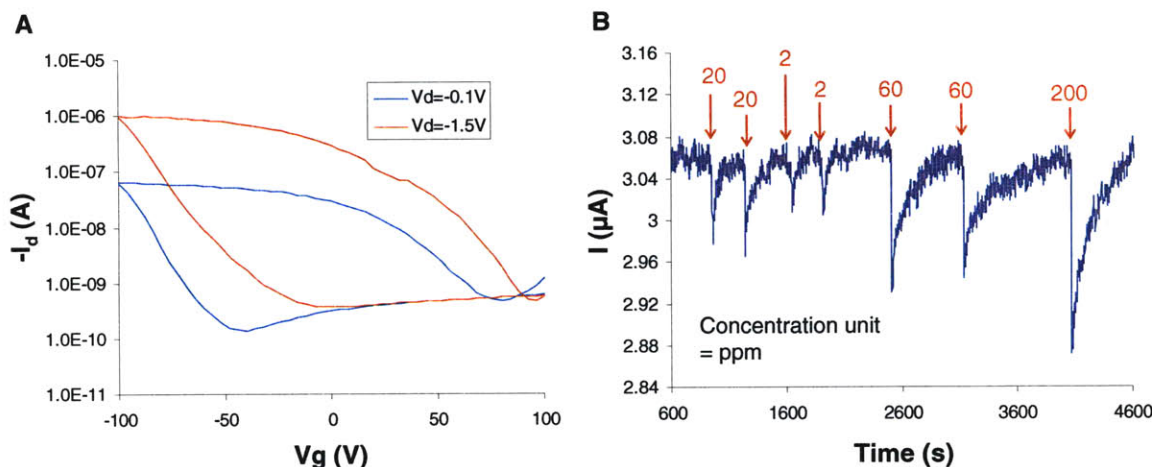


Figure 5. Applications of the membrane-transferred SWNT electronic network. a) Field effect transistors. Network of HiPco⁴² SWNT across 10 μm -gap electrodes, b) Gas sensors. Network of laser SWNT across 5 μm -gap interdigitated electrodes responds to nitrobenzene vapor at various concentrations. The sample was tested at 0.1 V.

2.3. Chemical vapor deposition: direct growth on a substrate

SWNT can be individually dispersed in water, but nanotubes tend to form bundles during deposition onto a substrate. The problem is generic in most deposition techniques including assembly on SAM²⁹, dielectrophoresis³³, and membrane transfer⁴¹. Upon aggregation SWNT loses many of their unique properties. SWNT sensors with bundles are not sensitive due to reduced surface-to-volume ratio. A SWNT bundle, if made out of unsorted nanotubes, behaves as a metallic wire, and semiconducting portion cannot be utilized. Intensity of the near-IR photoluminescence also decreases upon aggregation, limiting applications in optical probes/sensors.

SWNT, when deposited from solution, have lots of residual surfactants which cannot be completely removed even by extensive rinsing or annealing. For instance, Raman spectra of a membrane-transferred SWNT array show several features from the cellulose membrane, suggesting residual cellulose are trapped between nanotubes. When integrated into an electrical device, the residues act as major scattering centers thereby

reducing the mobility of charge carriers by several orders of magnitude. The residues also cause poor adhesion between nanotubes and metal electrodes, not only increasing the contact resistance of the device but causing poor yield during lift-off process.

Using catalytic chemical vapor deposition (CVD) carbon nanotubes can be grown directly on a substrate.⁴³ CVD-grown SWNT are of the highest quality one can get on a substrate with properties comparable to the theoretical limit. Three elements are required in the growth process: 1) carbon source (CH_4 , C_2H_4 , EtOH, etc.), 2) high temperature (700-1000 °C) to decompose the carbon source, 3) catalyst nanoparticles (transition metals, or silicon) on which the carbon materials are decomposed. It is believed that decomposed carbon dissolves into the liquid phase metal catalyst, and nano-“tube” grows from super-saturated catalysts since the tubular form is thermodynamically most stable.⁴⁴ However, detailed mechanism is still under investigation.

There are numerous advantages of the CVD-growth. First, nanotube aggregation and tube-tube junctions can be minimized when tube density is kept low. Properties of the nanotube bundles and tube-tube contact are largely unknown, and therefore the system becomes more complex and harder to study when bundles and networks are present. For this reason, CVD-SWNT is ideal for studying mechanisms and comparing with theory. Second, there is no surfactant involved in the process, so the electrical carrier mobility is several orders of magnitude higher compared to the devices made from solution-processed nanotubes. Performance of electronic devices has always been better with CVD-SWNT. Third, tubes can be grown not only horizontally but also vertically. Vertically aligned array with high tube density can be prepared only by CVD and has been used when high-speed chemical/physical communication is needed in a vertical direction (e.g. membrane for fast molecular transport⁴⁵, (electrical) connection between stacks of devices⁴⁶). Forth, CVD-SWNT are much longer than the solution-processed tubes, and therefore more compatible with micro-fabrication technology. Solution tubes are short (~500 in average, 3 μm at most) because long tubes do not suspend well in solution, and sonication step for ripping the bundles apart is known to cut nanotubes⁴⁷. Conversely, CVD-SWNT can be as long as 18.5 cm.⁴⁸ Nanotubes can then be cut/patterned into desired length/shape and electrically interfaced with other devices without using tedious e-beam lithography.

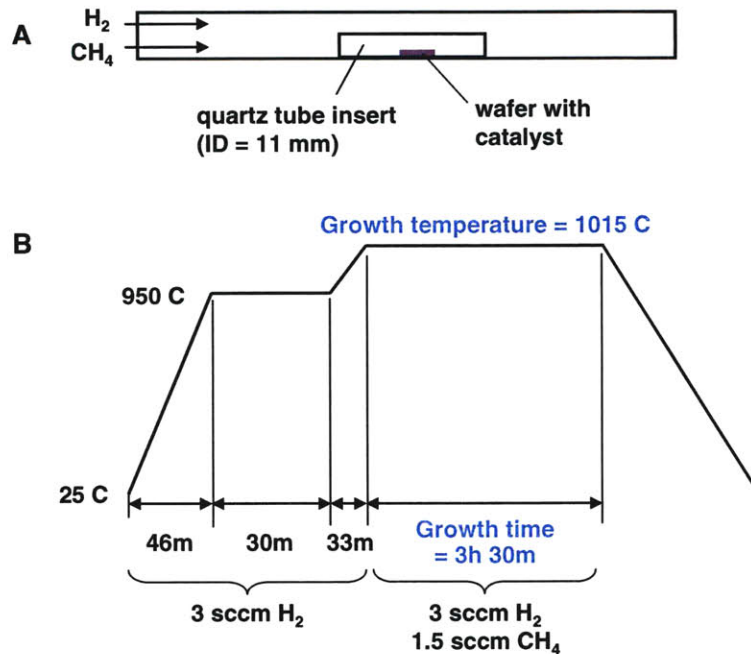


Figure 6. SWNT growth using chemical vapor deposition (CVD). a) experimental setup. Substrate with catalyst is placed in a small quartz tubing to minimize turbulence around the sample. Laminar flow of H₂ and CH₄ are used for alignment. b) Detailed growth conditions.

A simple diagram of our CVD setup is shown in Figure 6a. A silicon substrate with Fe nanoparticles as catalyst is placed in a quartz tubing insert with 11 mm inner diameter. The insert is then placed at the center of a 22 mm-ID quartz tubing. In order to align the nanotubes along the gas flow, the flow rate is kept low at 3 sccm of H₂ and 1.5 sccm CH₄. The insert further stabilizes the gas flow near the substrate.⁴⁹ Growth temperatures vary between 970 °C and 1015 °C. Detailed growth conditions are shown in Figure 6b. SEM images of the grown nanotubes are shown in Figure 7. Tube density is high in the catalyst region, and portions of the tubes grow out of the catalyst region and are aligned along the gas flow (Figure 7a). Zoom-out image in Fig 7b shows continuous growth of perfectly aligned nanotubes. During the growth end portions of nanotubes at the downstream are detached from the substrate and fly over obstacles (kite mechanism).⁵⁰ This enables growth over trenches or slits of hundreds of microns (Figure 7c-d), which cannot be easily done when deposited from solution.

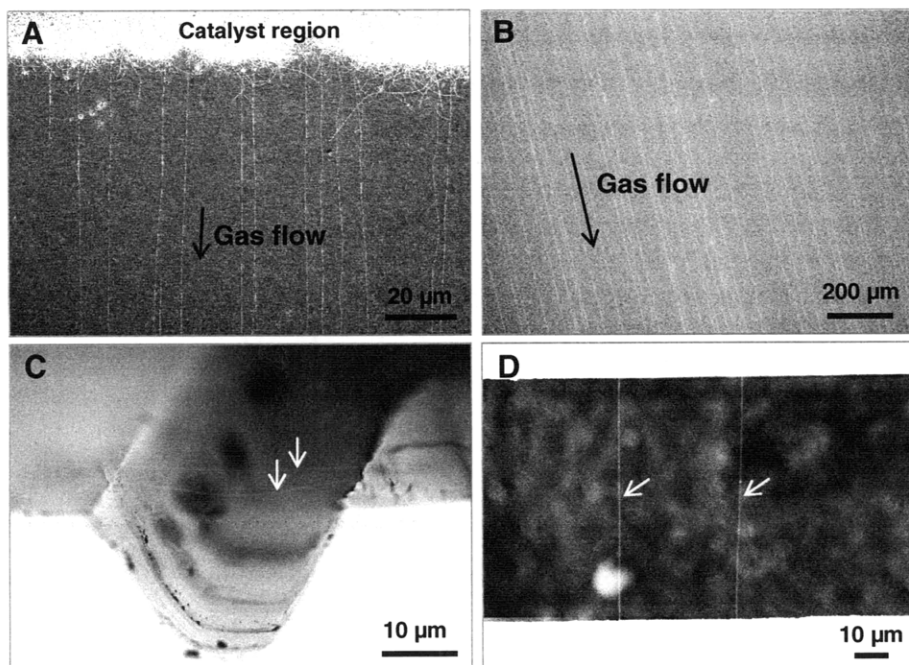


Figure 7. SWNT grown by chemical vapor deposition (CVD) a) SWNT grow from a catalyst region and are aligned along the flow direction of feed gas. b) SWNT can be as long as several cm. c) SWNT grown on a silicon trench. d) SWNT grown on a silicon slit.

Part I. Exterior of single walled carbon nanotubes for reversible detection of nerve agents

Chapter 1. Introduction to single walled carbon nanotube gas sensors

Single walled carbon nanotubes (SWNT) can be conceptually formed by rolling a graphene sheet.⁴⁴ Depending on the rolling angle and the diameter, SWNT can be either metallic or semiconducting.⁴⁴ The diameter is around 1 nm, and the length can be as long as a few cm.

SWNTs have several advantages as sensor elements such as large surface to volume ratios, one dimensional electronic structure, and a molecular composition consisting of only surface atoms.⁵¹⁻⁵⁶ SWNT gas sensors are one of the only materials to electrically transduce molecular binding to their surface directly at sub-ppb level of analyte concentration.^{51,57} The 1-D electronic structure of SWNT is easily disrupted even by a single adsorption event.^{54,58} Hence, sorption-based sensors from these materials have become a promising application.⁵⁹ Recent versions utilize a change in dielectric constant⁵⁶, but typically the change in conductivity of a single or array of nanotubes is used for such applications. Early prototypes have been utilized as a field effect transistors (FET)^{51,60-62} where drain currents are modulated by the adsorption of electron withdrawing/donating molecules that change the charge carrier density. Since the undoped metallic SWNTs have a lower density of states at the Fermi level compared to the valance band edge of the semi-conductors,^{63,64} the latter are considered to play a larger role in the sensor operation.^{53,54}

Sensor elements can be either individual SWNT^{59,65} or multiple SWNT array.^{51,57} Polymer functionalization has been used to improve the sensitivity and selectivity of the sensor^{51,57}. In case of irreversible sensors, several methods were demonstrated in order to regenerate the array, including venting under ambient conditions⁵⁹, annealing⁵⁹, applying electric field⁵⁷, and UV irradiation.^{51,66} Various analytes have been tested to benchmark the performance: oxygen⁵⁵, nitrogen dioxide^{51,59,67}, ammonia^{51,57,59,68}, methane⁶⁹ for environmental monitoring, and a nerve agent simulant dimethyl methylphosphonate (DMMP)^{57,70}. Sub-ppm detection capability was demonstrated for all these analytes. High sensitivity and selectivity can be achieved by polymer coatings^{51,57,62,68}, or doping⁵³ the

nanotubes. Due to the nature of signal transduction, it has been difficult to detect analytes with no apparent electron-withdrawing or donating properties. For the detection of these molecules, SWNTs loaded with transition metal nanoparticles are used.⁶⁹ Peng and Cho⁵³ have predicted, in their *ab initio* study, the possibility of detecting molecules that do not bind to a nanotube such as CO and H₂O. They suggested doping of impurity atoms (boron, nitrogen, etc.) into SWNTs or the use of composite B_xC_yN_z nanotubes. Han et al.⁷¹ demonstrated the technique experimentally.

Although recent studies by Snow et al.^{72,73} have utilized a capacitor arrangement, most nanotube sensors operate as chemiresistors, where the conductance change upon molecular adsorption to the nanotube sidewall is monitored. Sensitivity and selectivity have been enhanced by applying selective binding ligands such as polymers⁵¹, DNA⁷⁴, or metal nanoparticles.⁶⁹ Oxidation defects apparently increase sensitivity as well.⁷⁵ The sensitivity of SWNT gas sensors scales with the exposed surface area⁷⁶ and typically reaches the ppb level for several systems in the literature.^{51,57} The typically cited mechanism for the electrical response is the adsorption-induced change in nanotube Fermi level and density of electronic states.⁵⁹ The role of the SWNT-electrode contact has been studied by contact-passivation, showing discrepant results to date.⁷⁶⁻⁷⁸

The nature of molecular adsorption onto SWNT remains poorly understood in several respects. Strong electron donors or acceptors appear to adsorb onto single nanotube or network devices irreversibly at temperatures near ambient. Consequently, the majority of SWNT gas sensors reported to date have an irreversible component in their responses.^{51,57,68,69,72,76,77,79} Subsequent data from the same systems occasionally demonstrate reversible sensor responses for the same analytes^{73,74,80,81}; however this contradictory behavior is not acknowledged or discussed in previous reports. Incidentally, such systems are typically regenerated manually, using methods including UV irradiation⁸², annealing⁵⁹, applying electric fields⁵⁷, and hydrolysis of analytes.⁷⁶ Even a novel gas sensor based on carbon nanotube capacitance⁷⁰ exhibits irreversible changes in its impedance upon molecular binding.

Chapter 2. Understanding the dynamics of signal transduction

It has not been clear as to how the performance of different sensor types should be benchmarked appropriately. In the case of reversible gas sensors, the magnitude of sensor response at steady state is related to the analyte concentration. For the carbon nanotube gas sensors reported to date, however, molecular binding to SWNT array is at least partially irreversible. This is true for a wide range of analytes and sensor configurations. Integral accumulation of analytes due to this irreversible adsorption provides nanotube sensors with the ability to detect small analyte concentration. The presence of irreversible binding sites, however, changes the dynamics of such a sensor and introduces a trade-off between analyte detection and total transduction time.

In this chapter, we develop a very simple model that describes the signal transduction in SWNT sensors in order to define parameters that benchmark the performance of different geometries or array types. The appropriate application of our model is restricted to sensors that involve direct transduction of the binding event via electrical modulation of the sensor surface. A straightforward analytical test from transient curves was demonstrated to distinguish between reversible and irreversible analyte binding. Within the context of the model, data in the literature are examined, and agreement is demonstrated for seemingly diverse sensing platforms and analytes.

2.1. Case I: Irreversible adsorption

Molecular adsorption to most SWNT sensor array is either partially or completely irreversible as suggested in the literature.^{51,55,57} On a timescale several times the original transduction timescale, removing the analyte molecules above the sensor does not regenerate the surface. Various active regeneration strategies discussed earlier are sufficient to restore the sensor. However, we focus on the molecular binding event itself in this work. Therefore, *irreversible* is defined as a response which cannot be completely restored simply by removing the analyte from the sensor, on the timescale of the initial transduction. We consider a general sensing array as shown in Figure 8.

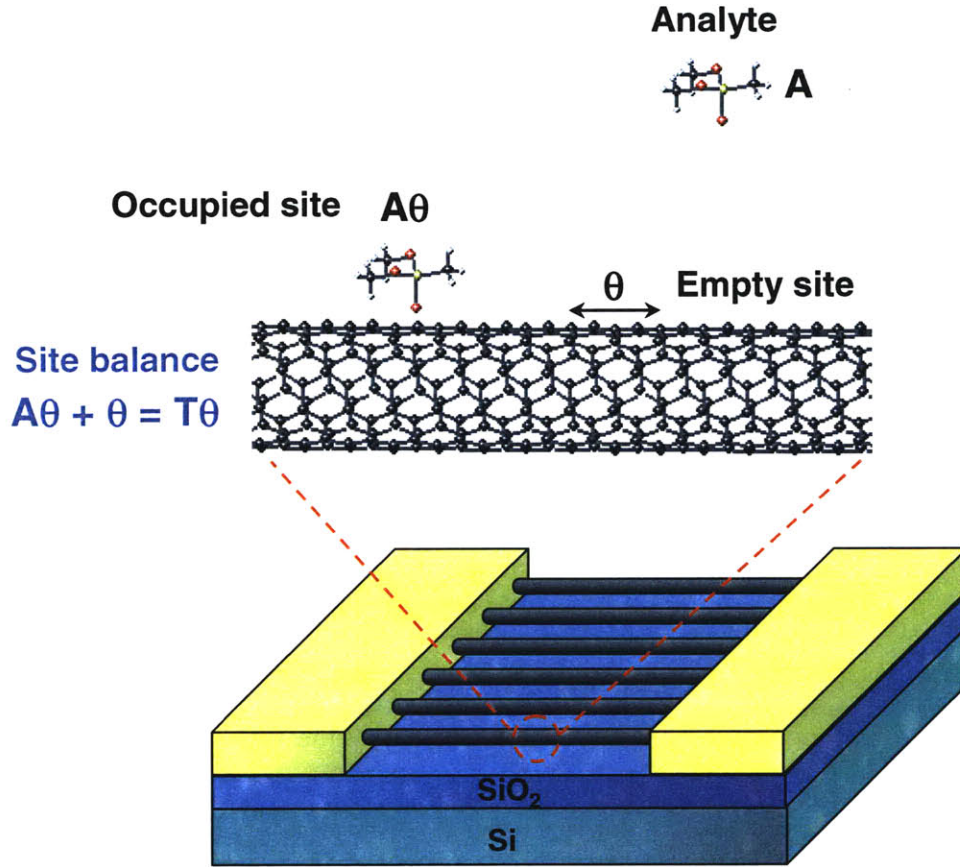
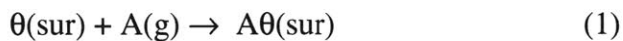
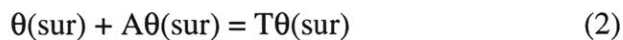


Figure 8. Prototypical nanotube gas sensor array illustrated. Analyte gas (A) adsorbs on the nanotube surface and occupies $A\theta$ sites, leaving θ sites empty. From the site balance, the total available adsorption sites ($T\theta$), which is proportional to the nanotube surface area, are the sum of A and θ sites.

The available total number of adsorption sites on nanotube surface ($T\theta$) can be divided into unoccupied sites (θ) and occupied sites ($A\theta$) by the analyte molecule (A). The analyte concentration, C_a , which is constant in our model, adsorb onto an unoccupied site according to surface event:



Here, the forward rate constant is k , and g and sur denote gas phase and surface bound species, respectively. From the conservation of total number of sites on a SWNT surface,



By definition, $T\theta$ is a constant property of the array, proportional to the accessible surface area on nanotube surface. The monitored sensor signal, S , is the change in array conductance (ΔG) normalized by the initial conductance (G_0). It is assumed that S is directly proportional to $A\theta$.

$$\frac{d^2 S}{d(A\theta)^2} = 0$$

This assumption is valid when the analyte dopes primarily the semiconducting nanotubes and causes a constant shift of the sub-threshold slope either higher or lower bias voltages. It is also true if metallic nanotubes dominate the baseline conductance and the carrier scattering introduced by analyte adsorption can be approximately linearized. The sign and magnitude of proportional constant is determined by the type of nanotube detector (n-type, p-type) and the overall electronegativity of analyte molecules. The rate of the sensor response is found from (1):

$$\frac{dA\theta}{dt} = k\theta C_a \quad (3)$$

In a variation of an Eley-Rideal mechanism, the gas analyte A adsorbs directly on the unoccupied sites in the simplest case⁸³. It is reasonable to assume there is no pre-adsorption isotherm for an uncoated array (i.e. no polymer over-layer). Equation (3) can be rewritten using the balance in (2):

$$\frac{dA\theta}{dt} = k[T\theta - A\theta]C_a \quad (4)$$

Solving it for initially clean array ($A\theta = 0$ at $t = 0$):

$$A\theta(t) = (T\theta)(1 - \text{Exp}[-kC_a t]), \quad S(t) = S_{\max}(1 - \text{Exp}[-kC_a t]) \quad (5)$$

S_{\max} is the maximum conductance change when the nanotube surface is saturated by the analyte.

It should be noted that it is not appropriate to report a detection limit for this type of sensor. Upon exposure to a continuous supply of analytes at any concentrations, the sensor will respond due to the integrated analytes and eventually saturate. Hence, the figure of merit is rather the response time, which scales as $\tau = 1/(kC_a)$, than the concentration detected. The appropriate benchmark to report is the surface reaction rate constant, k , since this parameter communicates the ability to transduce a given concentration, C_a , within a pre-defined time. SWNT arrays electrically transducer analyte binding far below the ppb level, where most sensor elements are equilibrium limited, due to the lack of a detection limit.⁸³

It is not necessary to examine the response at $t \rightarrow \infty$ since, at any concentrations, the array will always be saturated at a value proportional to $T\theta$. The initial slope of the sensor response near can be reported instead. The response rate from (5) is:

$$\frac{dA\theta(t)}{dt} = (T\theta)kC_a \text{Exp}[-kC_a t], \quad \frac{dS}{dt} = S_{\max} kC_a \text{Exp}[-kC_a t] \quad (6)$$

The appropriate way of reporting the response for this case is correlating the initial response rate with analyte concentration. The array can be exposed to the analyte long enough to generate this slope, and the system can be regenerated thereafter.

We can conclude from (6) that three principal ways of increasing the signal transduction rate exist. First way is to increase the number of nanotubes in the array, thereby increasing $T\theta$. Increasing the adsorption rate constant, k , is another one. This can be achieved by controlled doping of the array. The third is to coat the array using a matrix with high analyte solubility.^{51,57} The effective analyte concentration at the sensor boundary can be increased this way.

2.2. Case II: Reversible adsorption

When the analyte adsorption to the nanotube surface is reversible so that there is a constant exchange of analytes between gas phase and surface-bound phase, the dynamics is inherently different. The sensor can be regenerated, in this case, simply by changing the environment with a analyte-free gas. The binding of analyte, with concentration C_a , can similarly be modeled.



The adsorption rate constant remains as k , but the desorption rate constant is k/K with K a adsorption equilibrium constant. The site balance in (2) still applies, and the mass action law is:

$$\frac{dA\theta}{dt} = k[T\theta - A\theta]C_a - \frac{k}{K}[A\theta] \quad (8)$$

In case of a sensor partially occupied by analytes, with a surface concentration $A\theta(0)$, solving (8) yields:

$$A\theta(t) = \frac{\text{Exp}\left[-\frac{1+C_aK}{K}kt\right]}{1+C_aK} \left(A\theta(0) + C_aK A\theta(0) - C_aK(T\theta) \left(1 - \text{Exp}\left[\frac{1+C_aK}{K}kt\right] \right) \right)$$

For the case of an initially clean array at $t = 0$, the above is simplified to:

$$A\theta(t) = \frac{C_aK(T\theta)}{1+C_aK} \left(1 - \text{Exp}\left[-\frac{1+C_aK}{K}kt\right] \right)$$

$$S(t) = S_{\max} \frac{C_aK}{1+C_aK} \left(1 - \text{Exp}\left[-\frac{1+C_aK}{K}kt\right] \right) \quad (9)$$

In this case, the response rate is:

$$\frac{dA\theta(t)}{dt} = k(T\theta)C_a \text{Exp}\left(-\frac{1+KC_a}{K}kt\right), \quad \frac{dS(t)}{dt} = S_{\max}kC_a \text{Exp}\left(-\frac{1+KC_a}{K}kt\right)$$

Note that the properties of this type of sensor are very different. In the infinite dilution limit, the characteristic time of the response becomes concentration independent.

$$\lim_{C_a \rightarrow 0} \tau = \lim_{C_a \rightarrow 0} \frac{1}{k} \left(\frac{K}{1+C_a K} \right) = \frac{K}{k}$$

A straightforward way of determining which process dominates between irreversible and reversible is examining the scaling of the response time at infinite dilution limit. Note that at high concentrations, the binding can be approximated as irreversible. A detection limit, C_{limit} , can be defined for the reversible sensors as the minimum occupancy $(A\theta/T\theta)_{\text{min}}$ that can be resolved above the noise level.

$$C_{\text{limit}} = \frac{\left(\frac{A\theta}{T\theta}\right)_{\text{min}}}{K \left(1 - \left(\frac{A\theta}{T\theta}\right)_{\text{min}}\right)}$$

One result is that for any non-zero heat of adsorption ΔH ,

$$K = \exp\left(\frac{\Delta S}{R}\right) \exp\left(-\frac{\Delta H}{RT}\right) = \exp\left(-\frac{\Delta G}{RT}\right)$$

ΔS and ΔG are the entropy change and Gibbs free energy change, respectively, upon binding to the SWNT surface. The detection limit becomes poor at higher temperature where the equilibrium constant decreases. It is appropriate to report a measured detection limit for reversible case. The detection limit should be essentially independent of detector geometry. Unlike the case of irreversible binding, the steady state signal can be correlated as the familiar linear response as C_a is varied.

Additional sensitivity and selectivity to particular analytes can be imparted by attaching various functional groups to the array.^{51,57} The concentration, C_a , in both the irreversible and reversible cases can be replaced with $H_a C_a$, where H_a denotes a Henry's law factor. The $H_a C_a$ reflects a preferential enhancement or diminution of the analyte concentration in the coating layer. If the matrix particularly has a high partitioning coefficient so the dissolved analyte concentration is high, a non-linear solubility relation needs to be considered.

In addition, due to an apparent increase or decrease of the analyte sticking coefficient, $S(\theta)$, the adsorption rate constant k may also vary with functional group in the coating. The sticking coefficient, along with k , is related to the adsorption rate (r_a):

$$r_a = S(\theta) \hat{I}_z = k \theta C_a$$

where, \hat{I}_z is the total flux of analyte molecules.⁸³ For instance, k increase will be observed for the adsorption of electron withdrawing molecules if nanotubes are coated with electron rich polymers. Sticking coefficients for NO_2 adsorption, reported both for electron rich polyethyleneimine (PEI) coated nanotubes and for as-grown ones, is 2 orders of magnitude higher for the former.⁵¹

2.3. Application to literature data

Qi *et al.* grow a single semiconducting SWNT using CVD followed by PEI functionalization. The response to NO_2 was then examined. The signal recovery from conductance increase upon NO_2 exposure took 12 hours at room temperature.⁵⁹ A longer recovery time is expected for a multi-tube sensor coated with electron rich PEI due to the enhanced sticking coefficient and binding affinity for the electron-withdrawing NO_2 .⁵¹ The conductance change parametric in NO_2 concentration is shown below (Figure 9a).

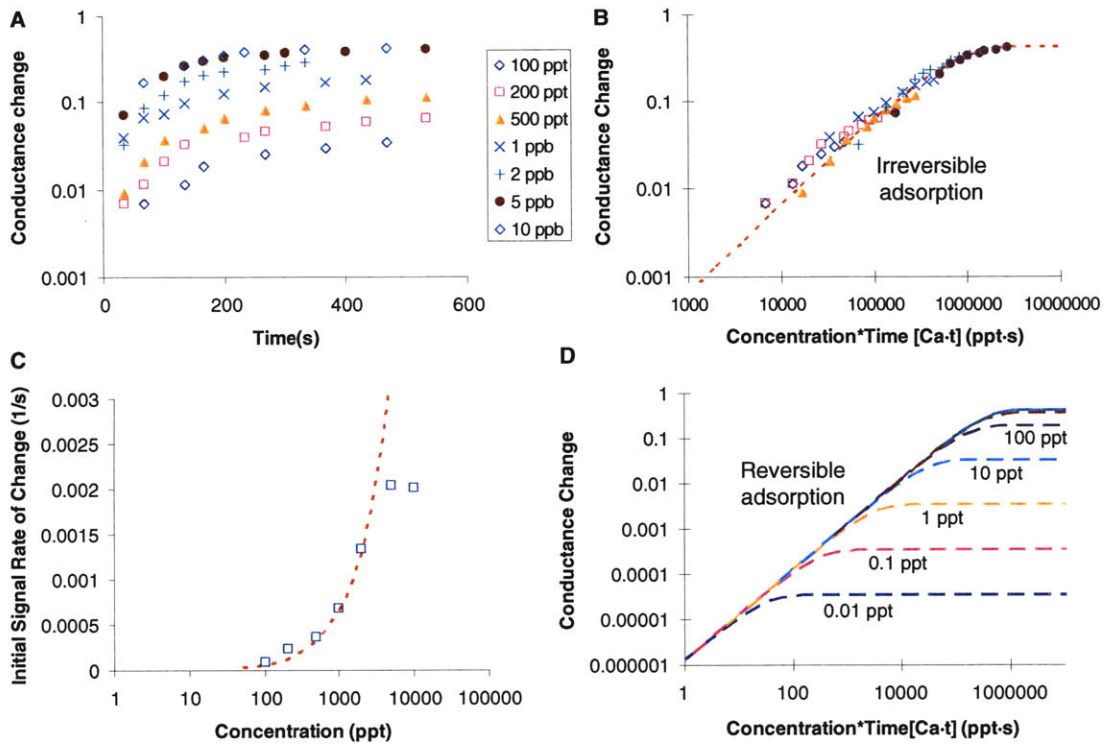


Figure 9. (a) Conductance change of PEI coated carbon nanotubes by an irreversible NO_2 adsorption at different concentrations (Data from Qi et al.⁵¹). (b) Conductance change plotted versus $C_a \cdot t$. All the points are fitted to a single model line (red dotted) described by equation (5). ($k = 1.64 \times 10^{-6} / \text{ppt} \cdot \text{s}$, $S_{\max} = 0.43$). (c) Initial signal transduction rate versus concentration. Experimental data (square) fit to a model line (equation (6), red dotted) at low concentrations. (d) A predicted reversible response¹⁷ using (9). The signal is parametric in concentration.

The signal does not reach a steady state, and the surface was regenerated using UV light at the end of exposure period.⁸² The maximum response, S_{\max} , is approximately 0.43 from the responses at high concentrations. Assuming a completely irreversible response, equation (5) can be used to obtain a useful scaling for this data. The conductance change plotted versus $C_a t$ should collapse the curves to one regardless of the concentration (Figure 9b). This behavior is a signature of irreversible adsorption, and it can be used to distinguish irreversible adsorption from reversible one. The adsorption rate constant of NO_2 on nanotube is regressed ($k = 1.64 \times 10^{-6} / (\text{ppt} \cdot \text{s})$). This rate constant should be independent of detector geometry and the number of nanotubes in the array. From equation (6), the initial slope from the sensor response can be correlated with concentration as shown in Figure 9c. Data points from the first 120 s were used to obtain

the initial rate. For all except the largest concentration⁸⁴, the initial slope increases with analyte concentration, and the model predicts the response curve accurately using the two previously regressed parameters. In contrast, when the same plot is generated for reversible responses (equation (9)), the response is predicted to be parametric in concentration as in Figure 9d.⁸⁵ Note that at high concentrations, where binding becomes irreversible, the data collapse to a single curve.

Qi *et al.*⁵¹ and Peng *et al.*⁵⁴ modeled the NO₂ vapor sensor response using a Langmuir adsorption model based upon the reversible adsorption limit. The conductance change, parametric in sticking coefficient, is plotted as a function of analyte pressure. An experimental sticking coefficient was then determined. For this system, however, NO₂ adsorption is partially irreversible because of a strong NO₃ co-adsorbate binding and stabilized NO₂ by electron rich polymer. For the case of irreversible adsorption, only at saturation when all sites are occupied does the sensor response reach equilibrium. Further understanding will be possible by examining the irreversible, surface rate constant, *k*, and how it varies for different analytes.

A similar analysis was performed for other systems in the literature. Novak *et al.*⁵⁷ use a modified sensor geometry. A monolayer of SWNT grown on the interior surface of a tube acts as a chemiresistor. Adsorbed DMMP, a nerve agent simulant, is desorbed by applying a positive gate bias. However, just flushing the saturated array with a DMMP-free stream only partially regenerates the sensor. Figure 10a plots the experimental response for their system. If adsorbed on a bare p-type SWNT device, the electron donating DMMP is less stable than electron withdrawing NO₂ on electron-rich PEI coating. This may explain why DMMP adsorption shows both reversible and irreversible site dependence. Irreversible adsorption is due to strong binding sites, while reversible adsorption is due to weaker sites. Hence, the properties of sensors *and* the analyte molecules determine the ratio of irreversible and reversible sites. We assume, for the simplest model, that these two sites independently contribute to the sensor signal. Therefore, one can extract reversible and irreversible component by simply taking a linear combination of the two models (labeled as additive in Figure 10). The best-fit surface reaction rate constant of irreversible component in this case is 1.98×10^{-6} /(ppt-s),

with approximately half (50%) of the total sensor response coming from the irreversible component.

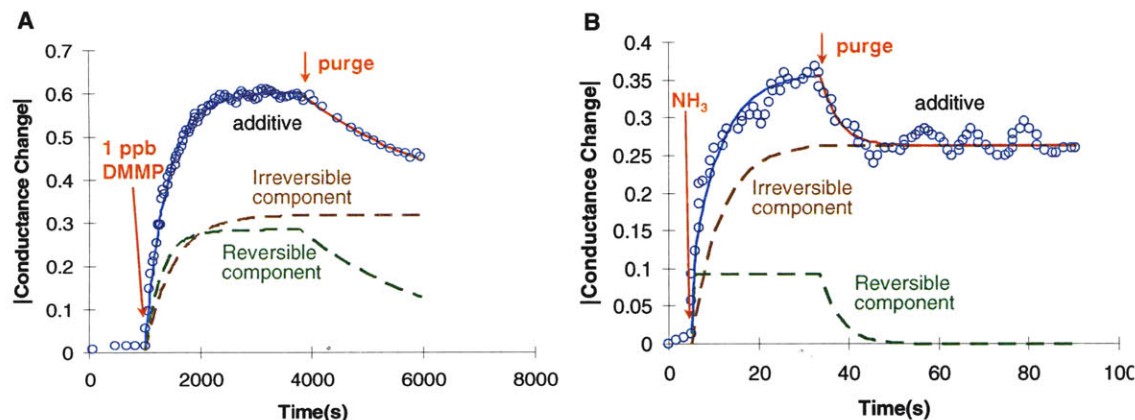


Figure 10. Response from a SWNT tubular chemiresistor (data from Novak et al.⁵⁷) showing both irreversible (brown) and reversible (green) components. Additive models are shown for detection (blue) and regeneration (red). (a) Response to 1 ppb DMMP. Contribution of irreversible component is 50%. $k(\text{irrev}) = 1.98 \times 10^{-6}/\text{ppt}\cdot\text{s}$, $k(\text{rev}) = 3.02 \times 10^{-6}/\text{ppt}\cdot\text{s}$, $K = 8.24 \times 10^{-3}/\text{ppt}$ are regressed. (b) Conductance response to NH_3 . A concentration of 100 ppb was assumed. 74% of the entire response is from irreversible component. Regressed rate constants are $k(\text{irrev}) = 1.56 \times 10^{-6}/\text{ppt}\cdot\text{s}$, $k(\text{rev}) = 6.32 \times 10^{-3}/\text{ppt}\cdot\text{s}$, $K = 2.59 \times 10^{-2}/\text{ppt}$.

Figure 10b shows the conductance change of the same sensor array for NH_3 .⁵⁷ The analyte concentration in this case is unknown.⁸⁶ The contribution of the irreversible component is found to be higher (74%). NH_3 as a weaker electron-donating molecule than DMMP is expected to be more stable on a hole rich p-type nanotube array. In the future adsorption rate constant k will be correlated with analyte binding energy. The binding energy for NO_2 is -0.42 eV, whereas -0.18 eV is reported for NH_3 .⁸⁷ The corresponding surface rate constants show a similar trend with a larger value for the former.

Chapter 3. Charge transfer from metallic SWNT sensor arrays

It has been unclear as to what quantity should be examined to optimize the sensor response in the aforementioned efforts to enhance sensor performance. The normalized conductance ($\Delta G/G_0$) has been typically examined. However, an effort to correlate the value with the nanotube chemical or physical properties has not been sufficient. Change in nanotube electronic density of states was suggested by density functional calculations^{53,88}, but its connection to actual sensor response has not been studied.

As discussed earlier, SWNT can be either metallic or semiconducting depending on its chirality.^{89,90} Especially utilizing the semiconducting SWNT has been a main focus because of several orders of magnitude conductance change upon chemical doping.^{59,61,77} Accordingly, the explicit function of metallic SWNT in sensor applications, and particularly in SWNT networks, has received little attention. The Schottky barrier FET⁹¹ model implies the semiconducting nanotube sensor response is in part from the Schottky barrier modulation at the metal electrodes/nanotube contact. It was Bradley et al.⁷⁷ who experimentally studied the role of this contact using a contact-passivated sensor.

In this chapter, we examine the SWNT response to molecular adsorption where the percolation of metallic nanotubes dominates the transport behavior. Both thionyl chloride (SOCl_2), a nerve agent precursor, and DMMP, a nerve agent simulant, are investigated. AC dielectrophoresis^{92,93} is used to form a SWNT network. The number of nanotubes is experimentally shown to be proportional to the array conductance. The previously developed model in Chapter 2 is used to analyze the response. Raman spectroscopy and electrical transport measurements are performed in order to verify the signal transduction mechanism. The charge transfer between SOCl_2 and carbon nanotubes will be shown to occur through a metallic pathway. Array-assist hydrolysis is used for the first time to regenerate the sensor.

3.1. Extracting the kinetic properties from the response

Figure 11a shows a typical response to 3 mL of 100 ppm SOCl_2 pulsed for 10 s at a source-drain bias voltage of 1 mV. The current rapidly increases upon analyte injection

for about 10 s while the analyte is being flown. The signal restores approximately 25% after 50 s, which presumably is due to analyte desorption. A similar type of response was observed in Novak et al.⁵⁷ Testing multiple devices confirms the signal does not restore for more than 4 hours. Analyte flow rate does not affect the response unless the analyte delivery is diffusion-limited. The response to dichloromethane solvent was negligible compared to SOCl_2 response.⁹⁴ A stepwise signal change was observed as expected for irreversibly binding analytes (Figure 12). Therefore, the thionyl chloride adsorption on untreated SWNT is at least partially irreversible as observed in several other systems.⁹⁵

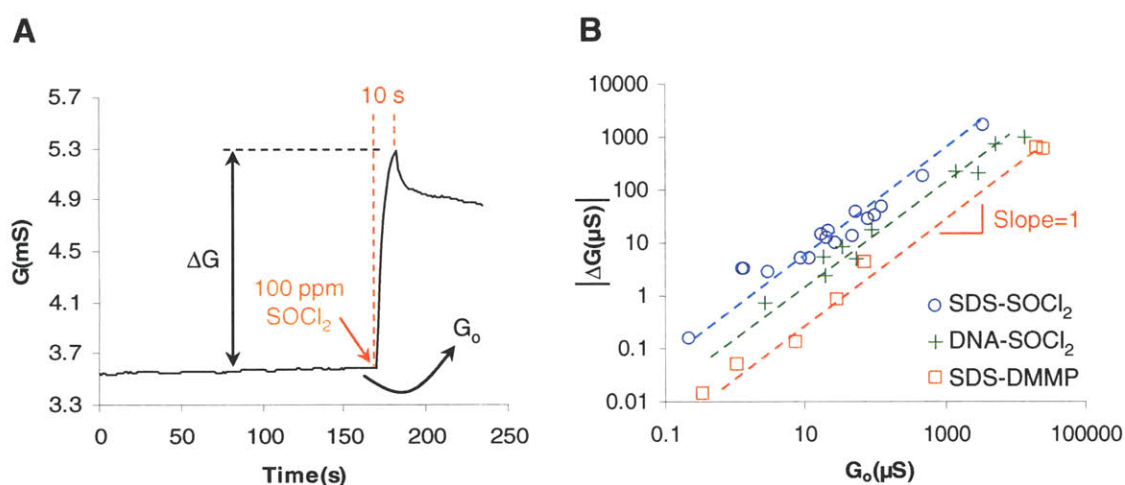


Figure 11. (a) A response to 10 s exposure to 3 mL of 100 ppm SOCl_2 showing partially irreversible analyte adsorption. G_0 and ΔG are related to the number of SWNT and analyte adsorbed, respectively. (b) ΔG from 34 sensors versus initial array conductance. SOCl_2 or DMMP responses from SDS-SWNT or DNA-SWNT fall on straight lines with slope 1 with different intercepts.

Testing each device at an identical condition (100 ppm SOCl_2 or DMMP pulse) enables to find a correlation between conductance change and analyte properties. The initial conductance before the analyte injection (G_0), and the conductance change on exposure to the analyte (ΔG) were measured. Figure 11b shows this relationship from three surfactant/analyte combinations for 34 devices. Three systems were examined: 1) SOCl_2 response from SDS-suspended nanotubes (3 μm , or 6 μm gap)⁹⁶, 2) SOCl_2 response from DNA-suspended nanotubes (6 μm gap), and 3) DMMP response from SDS-suspended nanotubes (6 μm gap). Negative responses were observed only in system 3). All responses are on straight lines with unity slope. The intercepts on a log-log plot

vary for different systems.⁹⁷ This unity slope corresponds to a constant $\Delta G/G_0$ at a fixed analyte concentration. The intercept values on the ΔG axis for 1), 2), and 3) are -0.2105, -0.8291, and -1.479, respectively.

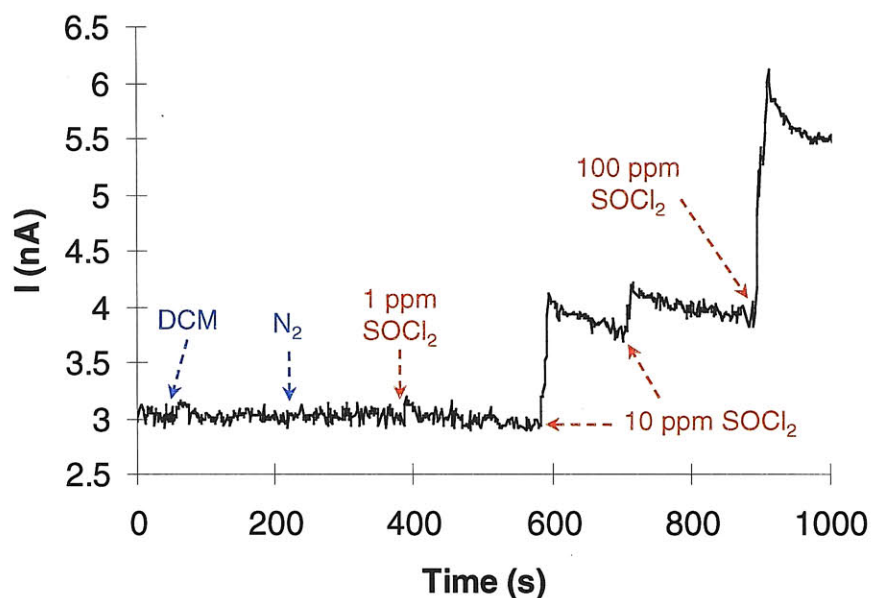


Figure 12. Response to dichloromethane (DCM) and thionyl chloride (SOCl_2). Response to DCM is negligible comparing to SOCl_2 response. Successive injection of SOCl_2 causes stepwise increase in the signal. This is caused by irreversible binding SOCl_2 molecules on nanotube surface.

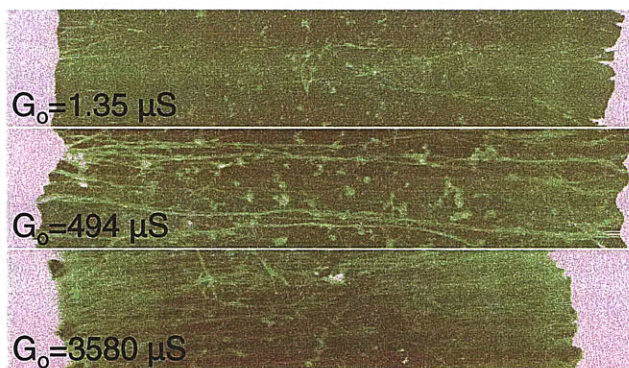


Figure 13. AFM images ($8 \mu\text{m} \times 1.5 \mu\text{m}$) from sensors with different initial conductance. Number of SWNT increases with G_0 .

We performed AFM on three devices with representative G_0 values as shown in Figure 13. Note that the number of SWNT increases with the array conductance. Hence, we can interpret the result in Figure 11b using the number of adsorption sites. For simple

analysis, the response in Figure 11a is assumed to be completely irreversible. We can then use the model for irreversible adsorption (Case I in Chapter 2). G_o is proportional to the number of SWNT across the gap, and thus, to the total number of adsorption sites ($T\theta$) available. ΔG is proportional to the number of analyte molecules adsorbed.

$$T\theta = \alpha G_o \text{ and } A\theta = \beta \Delta G \quad (10)$$

Proportional constants were denoted as α and β . If the sticking coefficients are the same for each nanotube array, a sensor with more nanotubes is expected to show higher conductance change at a fixed concentration. The ratio between two proportional constants (α/β) can be expressed using maximum normalized conductance change ($(\Delta G/G_o)_{\max}$) when all the sites are occupied by analyte molecules ($A\theta=T\theta$).

$$\frac{\alpha}{\beta} = \left(\frac{\Delta G}{G_o} \right)_{\max} \quad (11)$$

At a fixed concentration (e.g. $C_a = 100$ ppm) and time ($t = 10$ s), equation (5) can be rewritten as

$$\log \Delta G = \log \left\{ \left(\frac{\Delta G}{G_o} \right)_{\max} [1 - \exp(-kC_a t)] \right\} + \log G_o \quad (12)$$

The above equation predicts that ΔG and G_o should have a unity slope when plotted on a log-log scale. The experimental result in Figure 11b is explained well. The intercept values are related to the maximum available signal change, and therefore represent the sensitivity and selectivity of the sensor for a specific analyte. A simple sensor optimization procedure can be deduced: 1) prepare sensors with different configurations, 2) test one of each configuration at the same concentration, 3) use a configuration with the highest intercept in ΔG versus G_o plot.

Dialyzing DNA-suspended nanotubes against water does not flocculate the nanotubes. Thus, we hypothesize DNA wrapping around nanotubes, unlike SDS molecules⁹⁸, is relatively stable in a water rinse. We attribute the small intercept for DNA-SOCl₂ system to the reduced number of adsorption sites by wrapped DNA molecules. The low intercept value in the case of DMMP indicates the sensor is more optimized for SOCl₂ detection.

Two important parameters of a SWNT sensor, the analyte adsorption rate constant (k) and maximum signal $((\Delta G/G_o)_{\max})$ can be estimated from $\log(\Delta G)$ versus $\log(G_o)$ graph at two different analyte concentrations. The linear relationship between the two parameters was confirmed from 71 nanotube devices including the 34 plotted in Figure 11b. Values from lower concentrations, 10 ppm and 50 ppm, are plotted in Figure 14. Table 1 summarizes the result. The k values are of order 10^{-9} /ppt(parts per trillion)·s for all three types. This suggests similar analyte adsorption rate for all three system. The maximum signals vary for different systems. The rate and magnitude of the signal transduction can be related to k and $(\Delta G/G_o)_{\max}$, respectively. Compared to a previously analyzed system ($k \sim 10^{-6}$ /ppt·s, $(\Delta G/G_o)_{\max} \sim 0.43$)⁹⁵, k is smaller by three orders of magnitude, but with slightly higher $(\Delta G/G_o)_{\max}$ for our SDS-SOCl₂ system.

surfactant	analyte	C _a (ppm)	intercept	k (ppt ⁻¹ s ⁻¹)	$(\Delta G/G_o)_{\max}$
SDS	SOCl ₂	100	-0.2105	2.69×10^{-9}	0.533
		50	-0.5486		
		10	-0.8838		
DNA	SOCl ₂	100	-0.8291	9.41×10^{-10}	0.243
		50	-1.040		
SDS	DMMP	100	-1.479	3.29×10^{-9}	0.0345
		50	-1.556		

Table 1. From the intercept values in $\log(\Delta G)$ vs $\log(G_o)$ graph, both parameters (k and $(\Delta G/G_o)_{\max}$) can be extracted by testing the sensors at two different concentrations. The analyte adsorption rates are similar in all systems, but the sensitivities vary.

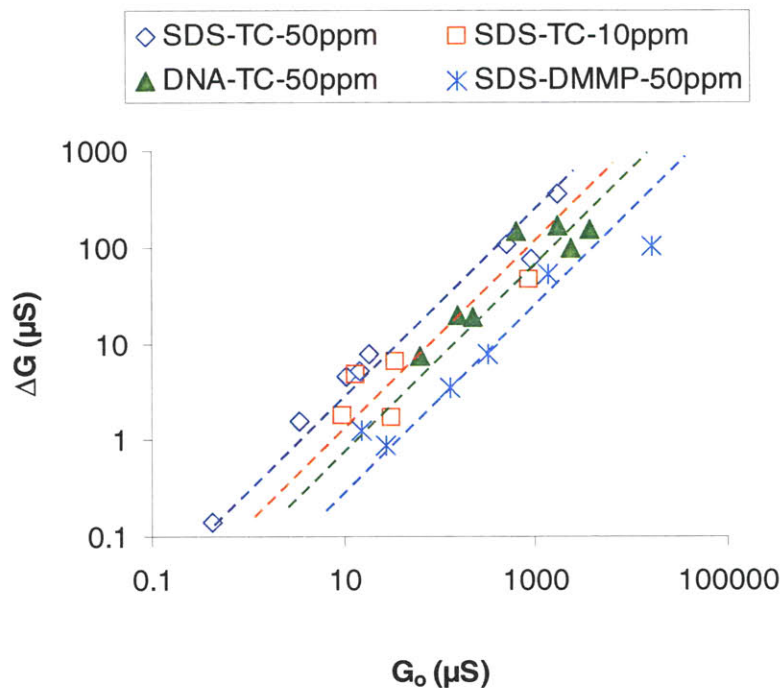


Figure 14. Responses at lower concentrations (10 ppm, 50 ppm) used to calculate k and $(\Delta G/G_0)_{\max}$ in Table 1. R^2 values are 0.976, 0.797, 0.842, and 0.941 for SDS-TC-50ppm, SDS-TC-10ppm, DNA-TC-50ppm, and SDS-DMMP-50ppm, respectively.

3.2. The role of electrode-nanotube contact in sensing

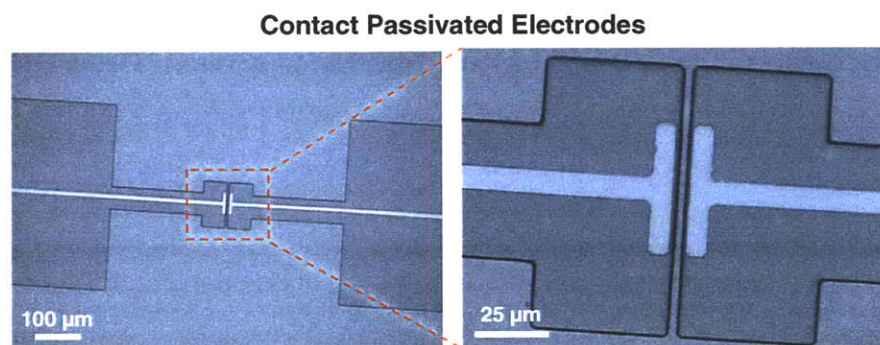


Figure 15. Contact passivated SWNT device. SU8-2 photoresist is used to passivate both electrodes and electrode-nanotube contact.

As previously discussed in oxygen sensors⁵⁵ by Heinze et al.⁹¹, one of the important issues in unveiling the mechanism of SWNT gas sensor is the work function modulation by the adsorbate, and thus the modulation of the Schottky barrier. We investigate the role

of nanotube-electrode contact in SOCl_2 detection. A photoresist (SU8-2, MicroChem) layer ($\sim 1.5 \mu\text{m}$ thick) was patterned to passivate the entire electrodes and nanotube-electrode contact (Figure 15).

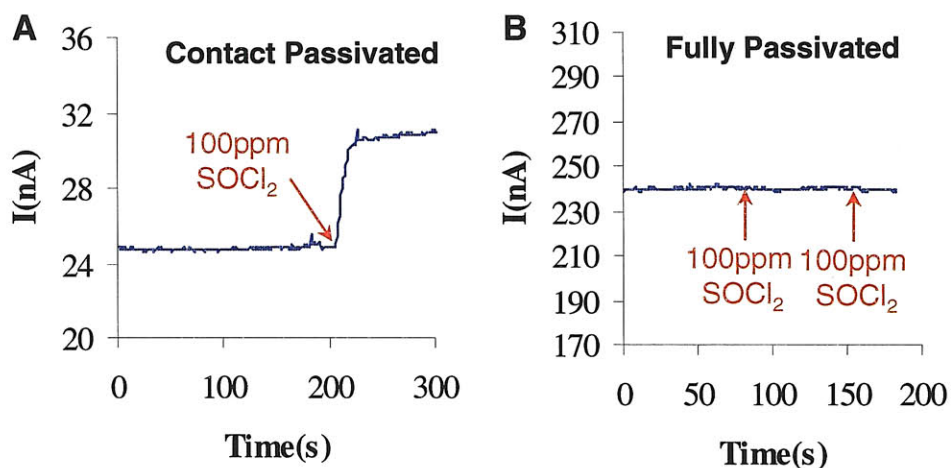


Figure 16. (a) The response from the contact passivated sensor. The conductance change matches the trend line in Figure 11b, suggesting the negligible role of metal-nanotube contact. (b) Completely passivated sensor exposed to SOCl_2 . No response confirms isolation is successful.

The conductance change from a contact-passivated electrodes, where only nanotubes were exposed, was 24% (Figure 16a). This is 72% of the expected signal from Figure 11b, considering that around 47% of the gap is covered. The small decrease in sensitivity ($\sim 28\%$) could be due to degradation of SWNT properties during lithographic process, or a diffusion barrier through the passivation layer. Figure 16b shows no response from a completely passivated sensor. This confirms the passivation scheme is effective. Thus, it was conclude that the contribution of metal-nanotube contact in thionyl chloride detection is minor.

3.3. Charge transfer from large diameter metallic SWNT

Raman spectroscopy at 633 nm and 785 nm laser excitation was performed to further understand the mechanism. The spectra were taken before and after 18,000 ppm

SOCl₂ injections⁹⁹ (Figure 17). All spectra are normalized with respect to the silicon peak.

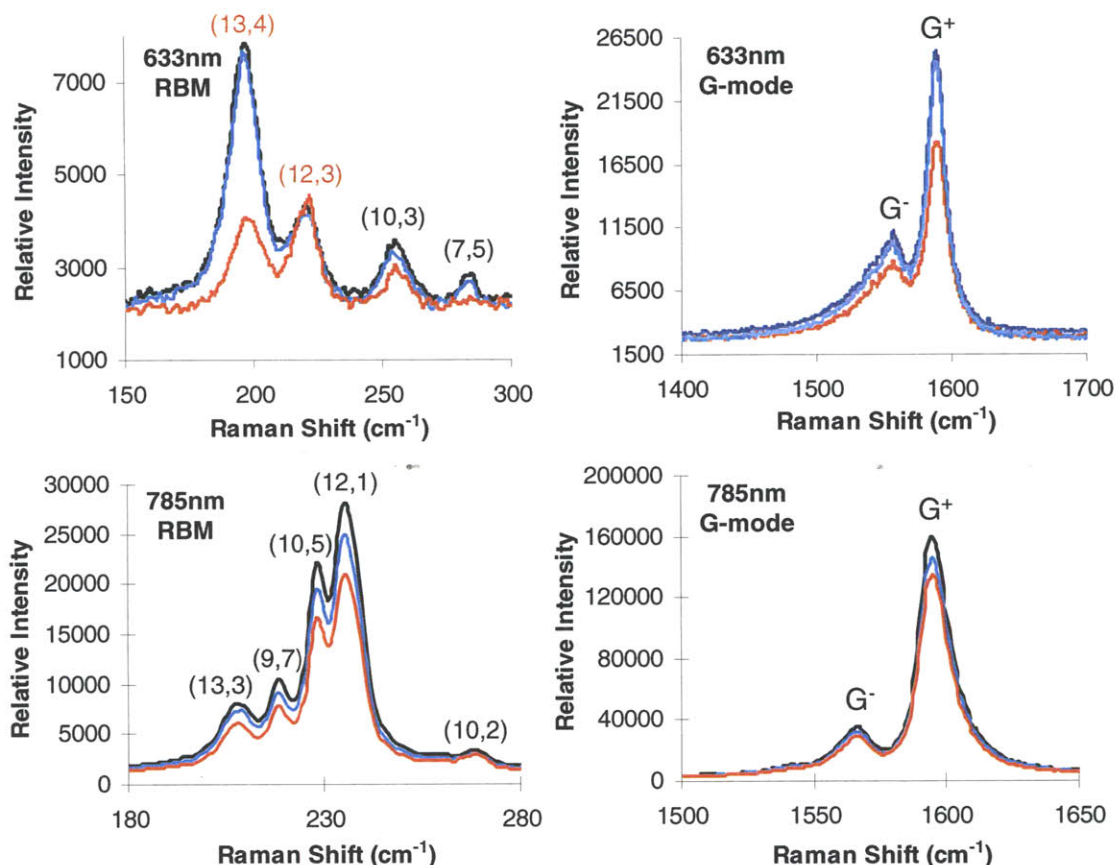


Figure 17. Raman spectra at 633 nm and 785 nm excitation wavelengths were taken in the following order: initial (black), dichloromethane (blue), and SOCl₂ (red). Both RBM and G-mode decreases. Red and black indices indicate the RBM from metallic nanotubes and semiconducting nanotubes, respectively. The most prominent decrease in (13,4) RBM suggest the preferential charge transfer from large diameter metallic SWNT to thionyl chloride. Larger decrease in G⁻ at 633 nm than at 785 nm further supports this mechanism.

A dichloromethane injection was made first, followed by a SOCl₂ injection. No noticeable change was observed at 633 nm from the former. Overall decrease in both RBM and G-mode was observed at 633 nm excitation. Conversely, SOCl₂ causes large decrease in both RBM and G-mode. Curiously, we notice the decrease is largely in (13,4) metallic SWNT feature¹⁰⁰

The RBM at this wavelength is couple to the c₂→v₂ transition of semiconducting SWNT (black indices) and c₁→v₁ transition of metallic SWNT (red

indices). What is typically observed in SWNT bundle formation is a unidirectional shift of resonance energy, which causes either an increase or decrease for RBM from different chiralities.¹⁰¹ The behavior is different from what we observe in our system. Large decrease in RBM suggests that there is an active electron flow from the SWNT network to the strongly electron-withdrawing SOCl_2 molecules. A similar selective RBM change was reported in the covalent functionalization of metallic SWNT.¹⁰² In our system, however, there is no evidence of covalent chemistry as supported by negligible D-band increase (data not shown). X-ray photoelectron spectroscopy (XPS) was not able to detect any residual Cl or S, so any remaining thionyl chloride remaining after exposure is below the detection limit of the technique ($\sim 0.01\%$).

The decrease in RBMs of semiconducting nanotubes at both wavelengths is not as prominent as the decrease in the (13,4) metallic peak. This selective signal decrease is observed in tangential G-mode as well. The G^- mode at 633 nm is a characteristic feature of metallic SWNT which can be fit using a Breit-Wigner-Fano (BWF) lineshape.¹⁰³ The preferential charge transfer from metallic SWNT is further supported by larger decay in G^- at 633 nm than in G^- at 785 nm.

3.4. Mechanism and modeling

We propose that the difference in M11 transition energy between (13,4) and (12,3) SWNT causes the preferential decay in the (13,4) RBM while the (12,3) peak remains constant as illustrated in Figure 18. We assume that the density of states does not change its shape by SOCl_2 , and that only a constant Fermi level decrease occurs.¹⁰⁴ As the SWNT Fermi level is lowered by SOCl_2 adsorption, the shift below the van Hove singularities (vHs) at the valence edge takes place at the (13,4) and larger diameter nanotubes first. The Fermi level is still above the vHs of (12,3) nanotube. The Fermi level after 18,000 ppm SOCl_2 exposure is estimated to be around it shifts below the van Hove singularity (vHs) at the valence edge for the (13,4) and larger diameter nanotubes first, whereas the value for the (12,3) tube is still above its vHs. The estimated Fermi level after 18,000 ppm SOCl_2 exposure is roughly 0.988 eV below the mid-gap. The current through nanotube is proportional to the transmission coefficient, thus to the density of

states, when a small voltage (1 mV) is applied at low temperature.¹⁰⁴⁻¹⁰⁶ Therefore, the main cause of the conductance increase is the increased density of states at the Fermi level by SOCl₂ adsorption for the large diameter metallic nanotubes.

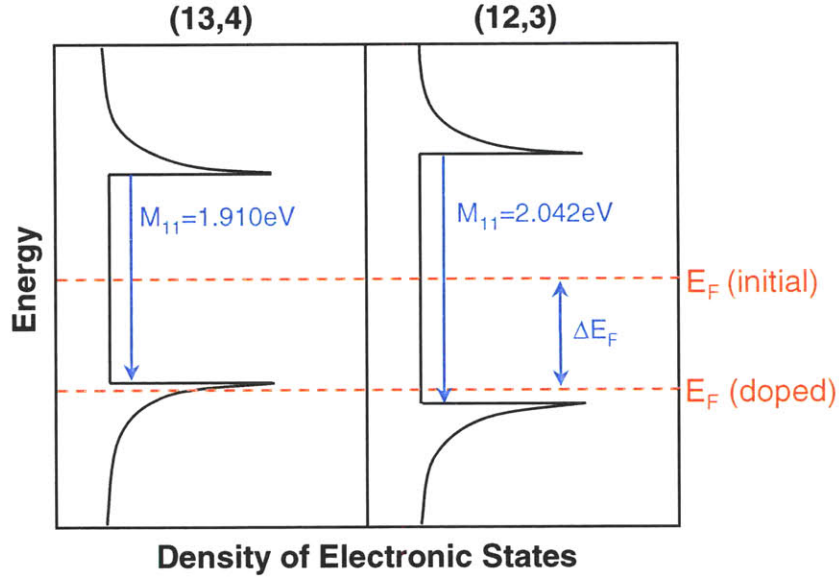


Figure 18. SOCl₂ adsorption causes a constant Fermi level shift (ΔE_F) below the first vHs for the (13,4). Fermi level of (12,3), conversely, remain above the first vHs. Depleted electron at Fermi level with high density of states at E_F explains both electrical and Raman data.

The Fermi level decrease helps electrons pass through the tunnel barriers as well, resulting in conductance increase. Both nanotube-gold contacts were models as tunnel barrier with height V_0 and thickness a as shown below in Figure 19a. The electron transmission coefficient in the asymmetric double barrier system¹⁰⁷ can be express as

$$T = \frac{T_L T_R}{\left\{1 - \sqrt{(1 - T_L)(1 - T_R)}\right\}^2 + 4\sqrt{(1 - T_L)(1 - T_R)}\cos^2 \Phi}$$

Φ denotes the sum of the various phase factors. T_L and T_R represent the transmission coefficients of the left and right barriers. T is a function of Φ and the Fermi level decrease (ΔE_F) in SWNT due to SOCl₂ adsorption. The increase in the electron transmission, and thus the conductance increase upon SOCl₂ injection as the E_F is lowered, could be

predicted using this model. ΔE_F versus T at two barrier heights (0.5 eV, 1 eV) is shown in Figure 19b.¹⁰⁸ When the sign of ΔE_F is reversed, negative responses to electron donating DMMP could be predicted as well.

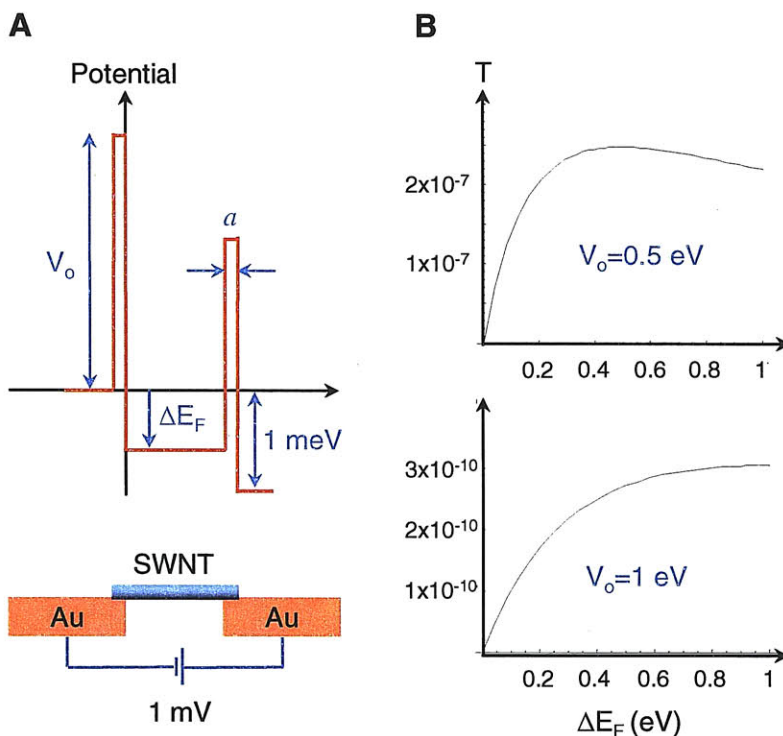


Figure 19. The system is modeled so that electron transfers through an asymmetric double barrier. (a) Nanotube-gold electrode contact is modeled as a tunnel barrier. The barrier height is V_0 with thickness a . SOCl_2 adsorption shifts the Fermi level downward (ΔE_F). (b) Calculated transmission coefficient for two different barrier heights (0.5 eV, and 1 eV). Decrease in the Fermi level results in an increased electron transmission, and thus the conductance increase.

3.5. Electrical transport measurement

Using the Raman spectroscopy for mechanism study of gas sensors has a limitation in that it collects spectra from nanotubes that do not cross the electrodes gap. A back-gate potential can be used to study semiconducting nanotubes actually contribute to the sensor response. Figure 20 shows a typical drain current change by gate bias with drain voltage 1 V at 100 ppm and 18,000 ppm SOCl_2 .

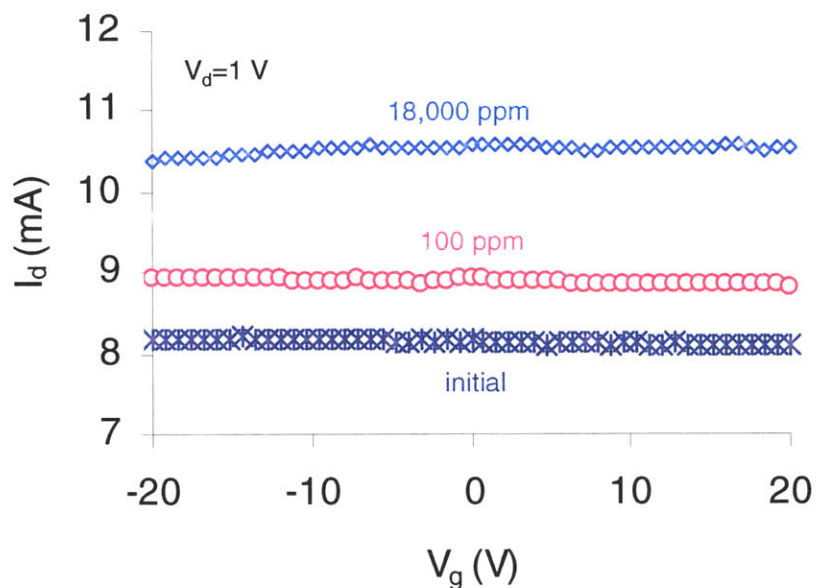


Figure 20. Drain current measure versus gate bias at two different SOCl_2 concentrations. A vertical shift with small on/off ratio near 1 suggests charge transfer to thionyl chloride through predominantly metallic SWNT.

The channel current is not modulated by gate voltage at all as can be seen in low on/off ratio (~ 1). This means the semiconducting SWNT are not contributing to the sensor response as described by percolation theory^{109,110} in a high density SWNT network. Only a vertical shift in drain current is observed upon SOCl_2 injections. This is in marked difference from the horizontal shift of a FET transfer characteristic for other gas sensors.⁵⁹⁻⁶¹ We concluded, from the vertical shift in electrical transport and the small on/off ratio, that signal transduction primarily occurs via charge transfer through metallic pathway. The negligible role of nanotube-electrode contact shown in Figure 16, further supports this mechanism. Currently the nature of metallic SWNT limits the sensing performance as a SOCl_2 vapor sensor. SOCl_2 detection limit estimated over three times the noise level (10 s pulse, 3 mL SOCl_2) is 3.9 ppm in average and 0.7 ppm at the lowest.¹¹¹

3.6. Regeneration via analyte hydrolysis

The irreversible binding of analyte molecules is a primary hurdle for most SWNT gas sensors that have appeared in the literature to date.^{51,57,68,69,112} We note that, for the

system explored here, there is a facile method of regeneration by hydrolyzing reactive molecules adsorbed on the nanotube surface (Figure 21). In the case of SOCl_2 , the decomposition by reaction with water is as follows (blue reaction):

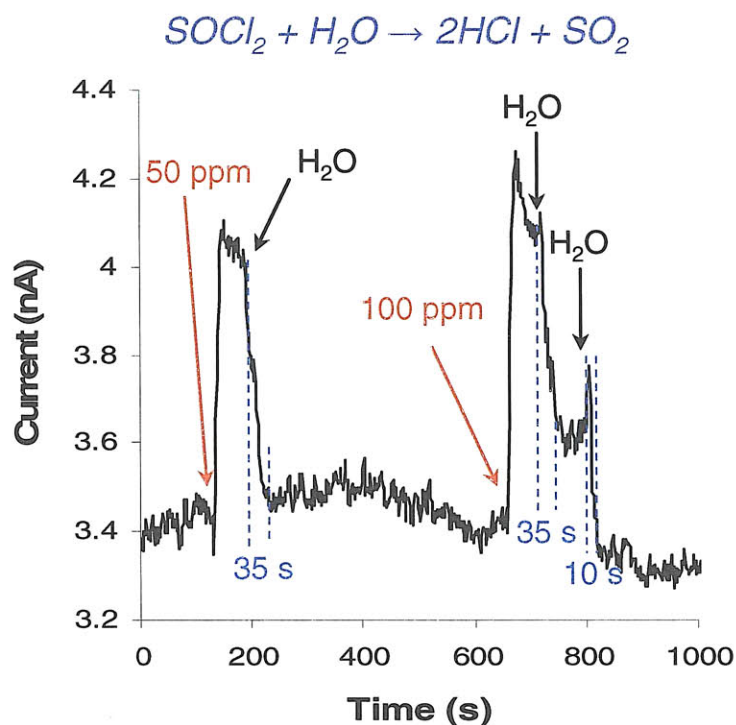


Figure 21. Active sensor regeneration. Rapid regeneration of nanotube surface from irreversibly-binding SOCl_2 molecules. Water reactive SOCl_2 can be hydrolyzed and desorbed from the nanotube surface by injecting water vapor on the array. Regeneration times are shown in red.

The signal increase after 50 ppm SOCl_2 exposure is restored rapidly when a pulse of saturated water vapor at room temperature was passed over the SWNT array. A higher current increase at 100 ppm SOCl_2 requires two successive water injections to get complete restoration. For most devices, 3 mL of saturated water vapor was enough to regenerate the surface. Once the signal recovers its original value, additional water injection causes no additional signal decrease. Hence, the response is not simply a negative response to water. We note that this method is the fastest way of regenerating a SWNT surface reported to date. Moreover, it applies to molecules capable of rapid hydrolysis which includes organophosphate chemical weapons. Low-temperature destruction of chemical agents including hydrolysis of mustard agent and nerve agent,

which has been already demonstrated, supports our argument.¹¹³ The focus on simulants of these species, such as DMMP, has obscured this chemical fact in the literature. Future studies will verify the efficacy of this method of regeneration.

3.7. Experimental

Silicon substrates (Montco Silicon Technologies) with 150 nm thermal oxide were metallized with 5 nm Ti and 300 nm Au, where electrodes with 3 μm or 6 μm gaps (Figure 22a) were patterned by photolithography. AC dielectrophoresis was performed to form a nanotube array between gaps (Figure 13b) as follows: 3 μL of HiPco carbon nanotube (Rice University) suspension (16.4 mg/L in 1% sodium dodecyl sulfate (SDS)- H_2O) prepared as described previously¹⁵ was dropped on the gap. AC voltage of 12 V_{pp} (3 μm gap) or 15 V_{pp} (6 μm gap) at 10 MHz was applied. The droplet was blown off, and the power was turned off. Although the control on SWNT coverage was attempted by varying deposition time (3 min~10 min), the array impedances ranged from 1.3 μS to 494 μS even at the same deposition time (3 min). The substrate was rinsed with deionized water to remove residual SDS. DNA (d(GT)₁₅)²⁴- suspended HiPco (6.64 mg/L) nanotubes were prepared and deposited in a similar way. The configuration allowed testing of the array field effect.^{51,60-62} Variation in electric field and deposition time results in different numbers of nanotubes in the channel. All nanotube suspensions were dialyzed prior to dielectrophoresis to minimize excess ions and surfactants in the solution.

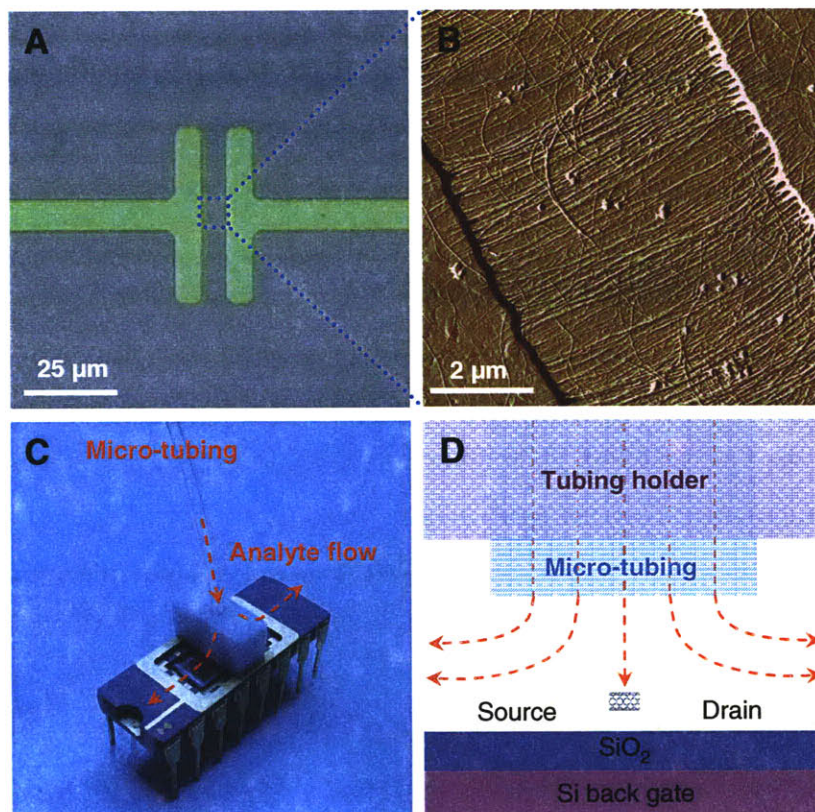


Figure 22. Sensor fabrication and testing. a) Optical image of 6 μm gap Au electrodes. b) AFM image of HiPco nanotubes deposited on the gap by AC dielectrophoresis. c) Setup for analyte delivery: Diced substrate is mounted and wirebonded to dual in-line package (DIP). Analyte is delivered perpendicularly to the substrate via the micro tubing and is free to leave the setup. d) Schematic of analyte delivery onto SWNT array. Area ratio of the tubing to the gap determines the efficiency of analyte delivery.

PFA (perfluoroalkoxy) micro medical tubing (ID=0.457 mm, Scientific Commodities, Inc.) was aligned and glued such that it was suspended above the gap for analyte delivery (Figure 22c). Delivered analyte molecules are free to leave the setup to the open air. This simple and disposable set up prevents contamination from highly corrosive thionyl chloride molecules. The analyte flow is perpendicular to the nanotube surface (Figure 22d). Only 0.2% of the total analyte is estimated to flow directly onto the gap from hydrodynamic analysis; it is noted that smaller diameter tubing or large gap electrodes could improve the efficiency of analyte delivery.

Desired SOCl_2 concentrations were obtained by vaporizing 2.0 M SOCl_2 (solution in dichloromethane, Sigma Aldrich) diluted in dichloromethane (Sigma Aldrich) in dry

flasks filled with ultra-high-purity nitrogen. DMMP analyte was prepared by diluting saturated vapor in the air.

Current-voltage measurements were performed using a semiconductor parameter analyzer (HP4155 and E5272A, Agilent). While monitoring the current at a source-drain bias voltage of 1 mV, a pulse of 3 mL of analyte vapor was injected for 10 s (0.3 mL/s) through the micro tubing. Raman spectra at the excitation laser wavelengths of 632.8 nm (1 mW) and 785 nm (37.5 mW) were also obtained before and after exposure to SOCl_2 , with a Kaiser RamanRXN1 analyzer.

Chapter 4. Chemically tuning the molecular adsorption

The transition between irreversible and reversible binding to a nanotube surface is a direct probe of the energetics of the adsorption process. The equilibrium constant of adsorption, obtainable directly from the transient sensor response, includes both entropic and enthalpic factors. A great number of mechanisms influence the thermodynamics of binding to these systems, including electron donor/acceptor interactions, dipole-induced dipole interactions, and steric influences of nanoscale curvature. Nanotube bundles, with spaces formed between neighboring nanotubes, form high energy pores of various potential. Lastly, junctions between metal and semiconducting SWNT possess uniqueness in both geometric and electronic properties.

In this chapter, we demonstrate, for the first time, the controlled tuning of adsorption energies on single walled carbon nanotube arrays, separating the influences of steric and electronic factors controlling the free energy of adsorption. Dielectrophoresis is utilized to generate SWNT electronic networks both above and below the percolation transition. Using thionyl chloride as a model adsorbate, the adsorption response is tuned by chemically treating the array with n-doping amines of $pK_a < 8.5$. The free energy of adsorption, extracted from reversible responses, is comparable to simple molecular potential (MP) calculation results. In-situ conductance and simultaneous Raman measurements were performed to find conditions for effective amine functionalization. A mechanism for tuning reversibility is proposed based on in-situ Raman, X-ray photoelectron spectroscopy (XPS), and MP calculations. Understanding the science of molecular adsorption enables us to reversibly detect the analyte with significantly enhanced sensitivity via polymer-functionalization. We demonstrate the detection of as few as 10^9 molecules of DMMP at the end of a μ GC column, suggesting that such arrays may form the basis of a new class of rapidly transducing molecular sensors with micron-size footprints.

4.1. Amine-functionalization tunes the reversibility

CY Lee et al., Amine basicity (pK_b) controls the analyte binding energy on single walled carbon nanotube electronic sensor arrays, *Journal of the American Chemical Society* 130, 5, 1766-1773 (2008)

CY Lee et al., On-chip micro gas chromatograph enabled by a noncovalently functionalized single-walled carbon nanotube sensor array, *Angewandte Chemie-International Edition* 47, 27, 5018-5021 (2008)

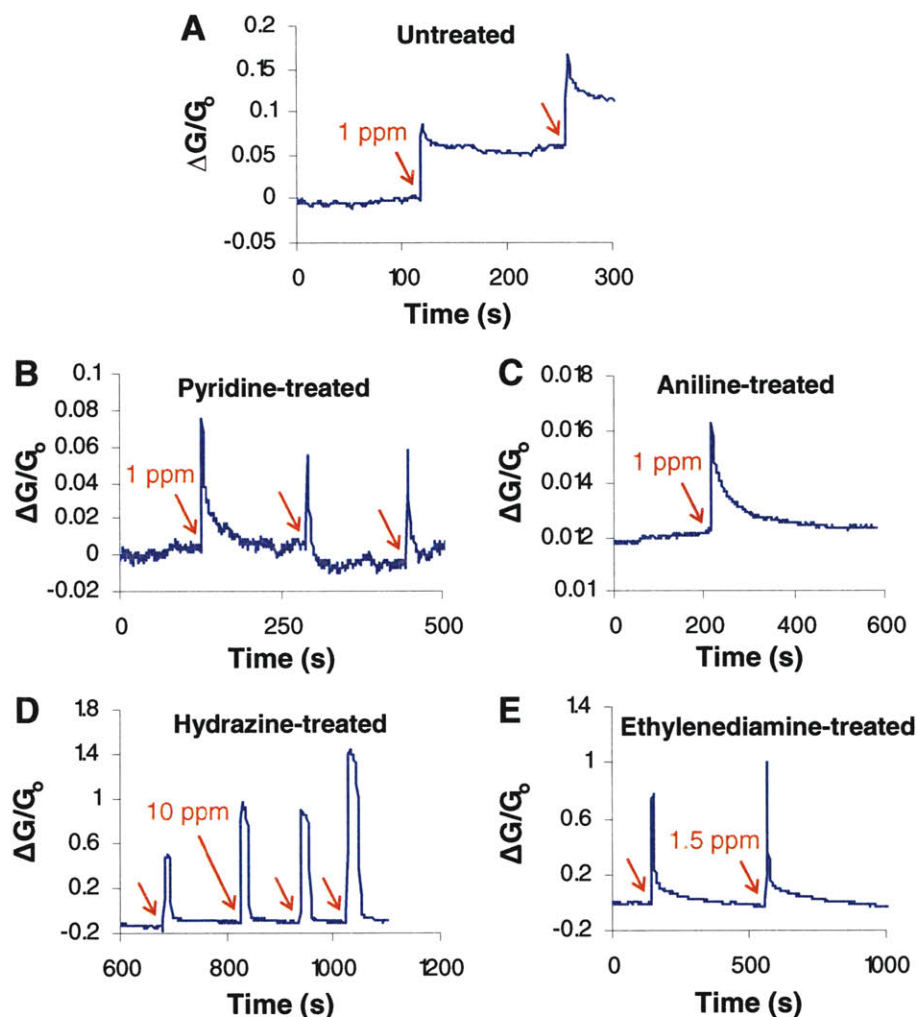


Figure 23. Tuning the sensor reversibility by surface chemistry. Normalized conductance change ($\Delta G/G_0$) was monitored upon exposure to thionyl chloride. (a) Irreversible stepwise signal increase from untreated sensor. Reversible responses from sensors treated with pyridine (b), aniline (c), hydrazine (d), and ethylenediamine (e).

Dielectrophoresis of an aqueous solution of SWNT and surfactant between $5 \mu\text{m}$ Au electrodes produces networks of varying connectivity and bundle size nearly a monolayer thin. As-produced SWNT networks show a stepwise conductance increase upon a pulsed 10 mL injection of 1 ppm thionyl chloride (Figure 23a). The signal does not restore to the baseline value for several days. This type of response is typical and well documented for these systems by our laboratory and others.^{68,69,76} In the case of thionyl chloride, it was conclusively demonstrated using subsequent hydrolysis that irreversible adsorption is responsible for the persistence of the response⁷⁶. Thionyl chloride is a

strong electron acceptor. The conductance increase is due to the enrichment of hole carriers by p-doping or enhanced electron transmission through nanotube-nanotube or nanotube-electrode contacts.

This behavior, however, is altered when the array is non-covalently functionalized by dropping and evaporating either small or large molecular weight amine-bearing molecules such as pyridine, aniline, hydrazine, and ethylenediamine. The current decreases immediately upon amine functionalization, consistent with n-doping by lone pair electrons.⁵¹ The sensor responses after amine-functionalization become reversible as in Figures 23b-e. Negligible drift in the baseline is observed after subsequent exposures. Adsorption (k) and desorption (k_{-1}) rate constants, and thus the equilibrium constant (K) for thionyl chloride adsorption can be extracted using our previously developed model.⁹⁵

$$S(t) = S_o \exp[-k_{-1}t] \quad (13)$$

$$S(t) = S_{\max} \frac{C_a K}{1 + C_a K} \left(1 - \exp\left[-\frac{1 + C_a K}{K} kt\right] \right) \quad (14)$$

S and C_a denote the sensor signal ($\Delta G/G_o$) and analyte concentration, respectively. Extracting kinetic/thermodynamic parameters by fitting the reversible response is shown using the aniline-treated sensor as an example (Figure 24a). The desorption part, an exponential decay from the signal when analyte is removed (S_o), is fitted to equation (13) to determine $k_{-1}=0.509 \text{ s}^{-1}$. Maximum signal (S_{\max}) was estimated to be around 2.71 by exposing the sensor to excess amount of saturated thionyl chloride vapor. Values for $k=1.74 \times 10^5 \text{ s}^{-1}$ and $K=3.41 \times 10^5$ are then extracted using (14) from the adsorption segment. Finally, the Gibbs free energy of adsorption ($\Delta G_{ad}=-0.330 \text{ eV}$), a thermodynamic potential related to the reversibility, is estimated from (15). Considerable variation was observed from sensor to sensor, even for the same functionalization chemistry. The origins of this variation are discussed below.

$$\Delta G_{ad} = -RT \ln K \quad (15)$$

The average free energy values of -0.252, -0.297, -0.157 eV are obtained in a similar way for ethylenediamine, pyridine, and hydrazine, respectively (Figure 24b, dark blue). These results suggest that the reversibility of SWNT sensor response can be tuned by systematically changing the surface chemistry. We also find that the values show a similar trend with the enthalpy of adsorption (ΔH_{ad}) between an amine and a thionyl chloride molecule calculated using a generic molecular potential (MP) (Figure 24b, red). The results suggest the thionyl chloride binds directly to the amine-functionalization.

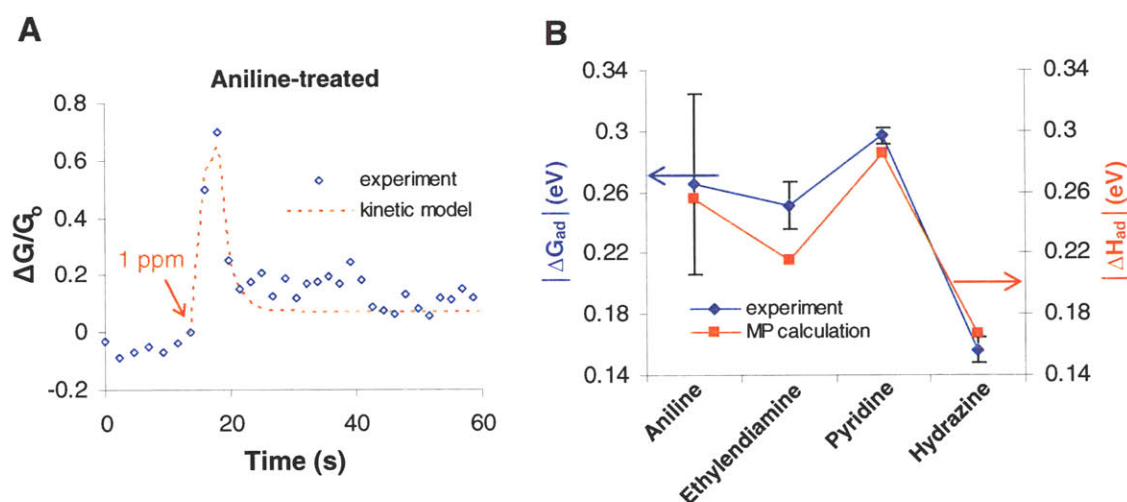


Figure 24. (a) A reversible response (diamond) fitted using our kinetic model (dotted line). (b) Comparison between the extracted free energy from experiment (diamond) and adsorption enthalpy from MP calculation (square).

Hydrazine-treated sensor showed unique responses. Only after ~8 s upon analyte removal did the signal start to recover. The recovery rate maximized at 10~20 s after the analyte removal (Figure 25). The mechanism is likely a surface reaction between hydrazine and thionyl chloride, or formation of a temporary charge transfer complex. Further study will answer this question.

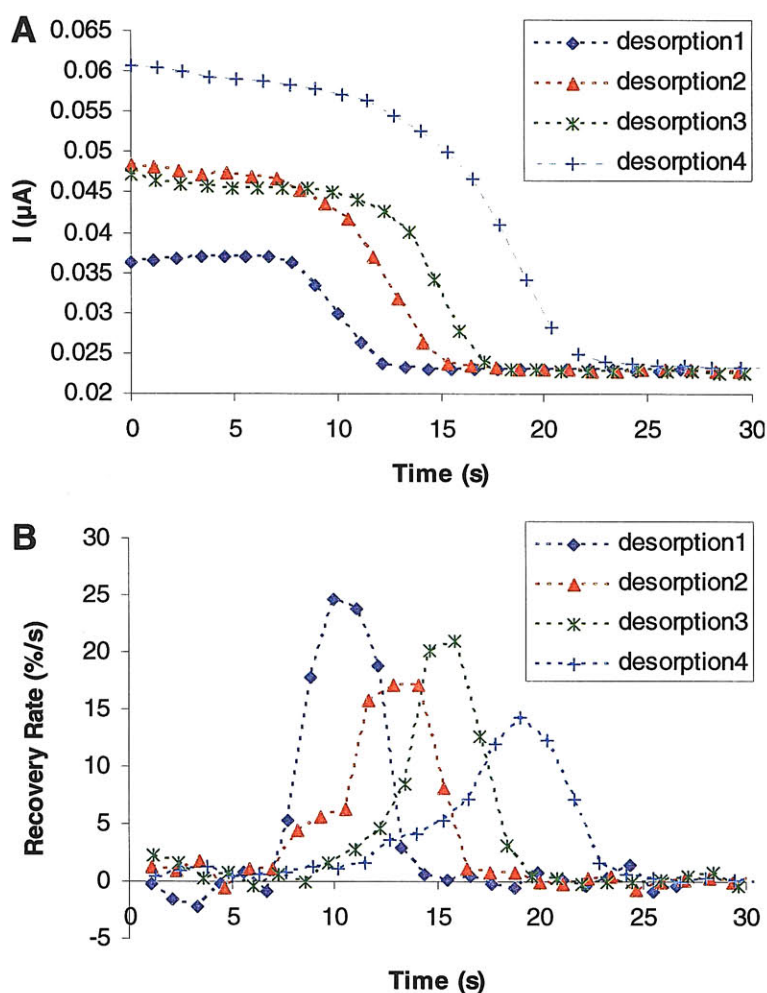


Figure 25. Unique desorption kinetics of thionyl chloride from hydrazine-treated sensors. (a) The signal recovery part from hydrazine-treated sensor in Figure 23d. The analyte is removed at $t = 0$ s, and ~ 8 s delay was observed for the signal recovery to start. (b) % recovery rate per second is plotted versus time. The rate maximizes 10–20 s after the analyte removal. Conversely, most sorption-based reversible sensors would show maximum at $t=0$. One explanation could be the reduction of thionyl chloride by aniline treatment ($2\text{SOCl}_2 + 4e^- \rightarrow \text{SO}_2 + \text{S} + 4\text{Cl}^-$). In this case a partial charge transfer from amine to thionyl chloride would occur, which might correspond to the 8 s delay. Thionyl chloride would then be reduced and desorbed from the SWNT.

Several conditions appear to influence the conversion from irreversible to reversible binding. Some amines failed to produce reversible binding at all. Benzylamine, diethylenetriamine, dimethylamine, and triethylamine are among those that are not effective, meaning that the sensor response remained irreversible even after application of the chemistry. A response from a butylamine-functionalized sensor is shown as an

example (Figure 26a). We also observe considerable sensor to sensor variation, even for the same surface chemistry, for this irreversible to reversible conversion (Figure 26b, aniline-functionalization failed). This variability motivates an investigation of the exact conditions necessary for the change in adsorption mechanism.

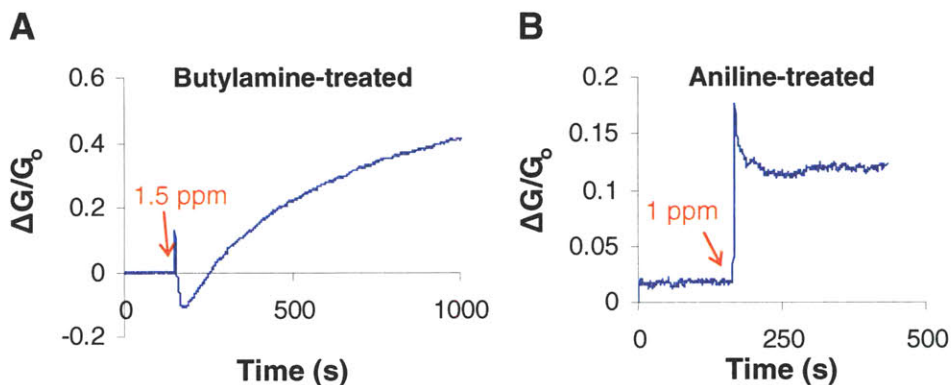


Figure 26. (a) Aniline-treated (partially) irreversible sensor. (b) An example of ineffective amine functionalization (n-butylamine-treated).

4.2. Conditions for reversible sensors

There is a strong correlation between the irreversible/reversible conversion, and a sub-percolated SWNT electronic network. We studied the conversion of 27 aniline-functionalized SWNT sensors to eliminate the chemistry as a variable. The functionalization is defined as effective if the response to a dilute thionyl chloride injection becomes (partially) reversible after treatment, and ineffective if it remains irreversible (Figure 27). The initial sensor conductance versus sensor number, assigned in ascending conductance order, is plotted as Figure 28a. We note that 67% of low conductance (< 1 mS) sensors were reversible, while only 13% of high conductance (> 1 mS) sensors were reversible. The trend displayed in Figure 28a is comparable with 2D percolation behavior in nanotube networks where a sharp conductance increase is observed well above percolation threshold.¹¹⁰ We conclude that the SWNT network should be near or slightly above the percolation threshold for effective conversion.

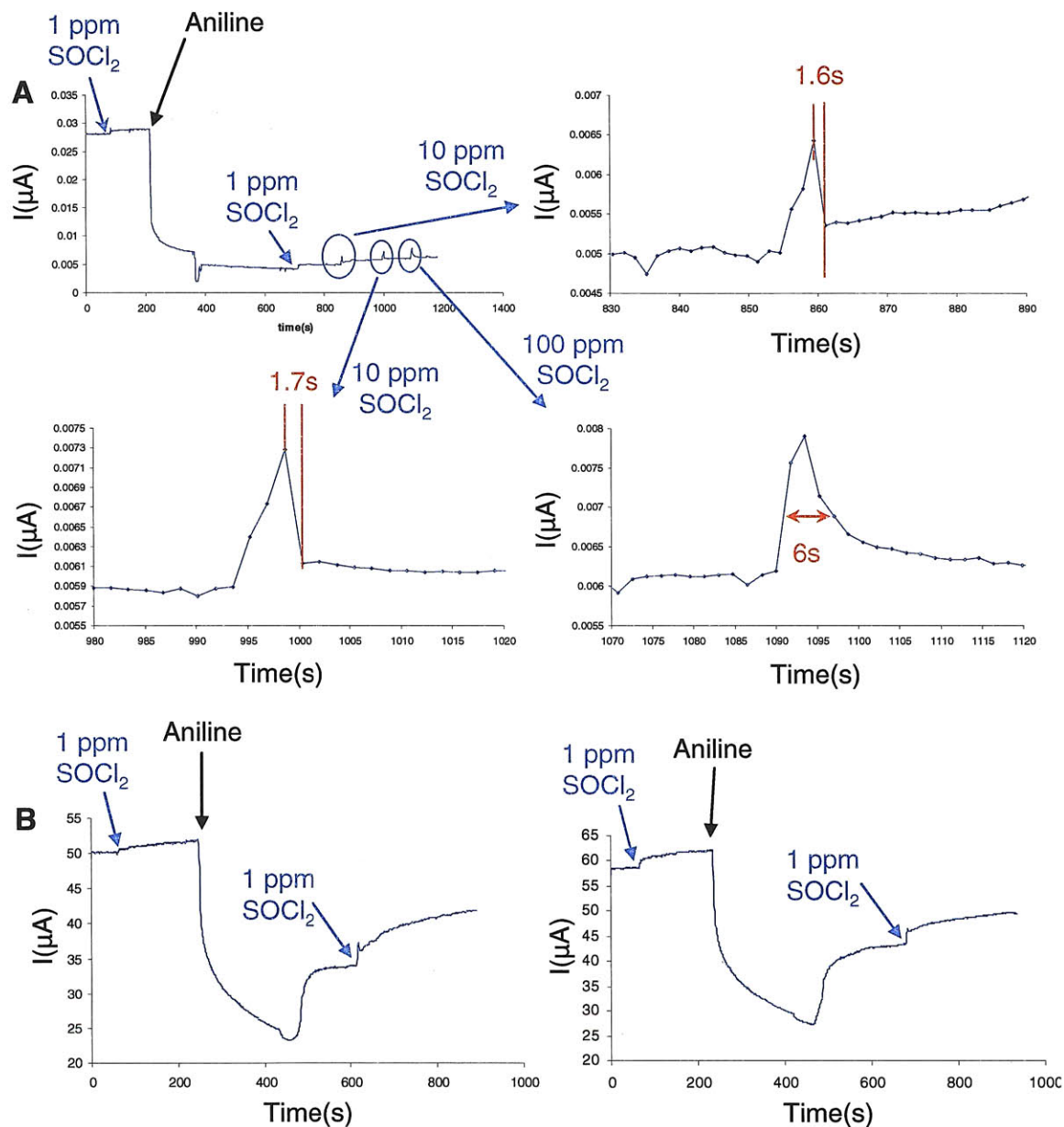


Figure 27. Response to thionyl chloride (SOCl_2) from aniline-treated sensors (effective versus ineffective). (a) An example of effective aniline functionalization. The response to thionyl chloride from untreated sensor was irreversible. Aniline drop caused a sharp decrease in the signal. After the aniline droplet evaporated and the signal stabilized, SOCl_2 response became reversible. (b) Examples of ineffective aniline coating. The response to SOCl_2 remains irreversible even after amine-treatment.

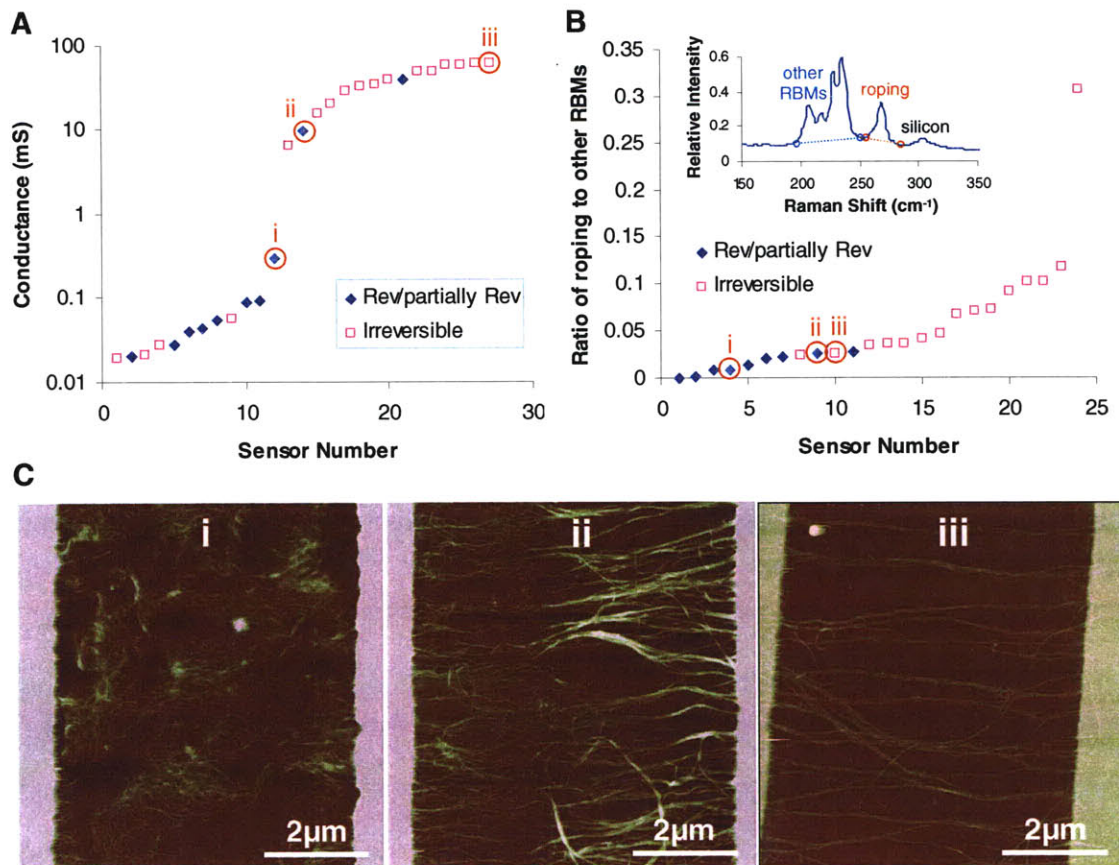


Figure 28. Required properties of SWNT network for effective functionalization. Array conductance and Raman features from 27 aniline-functionalized sensors are correlated with the reversibility. Dark blue and pink shapes denote (partially) reversible and irreversible sensors, respectively. (a) Conductance versus reversibility, showing that a SWNT network near percolation threshold is desired. (b) Raman roping peak to other RBMs ratio versus reversibility. Minimal SWNT aggregation is necessary for the chemistry to effectively shift the reversibility. (c) AFM images from three representative sensor arrays i, ii, and iii from (a) and (b).

The effect of nanotube aggregation on the effectiveness of chemical treatment was studied using Raman spectroscopy at 785 nm laser excitation. SWNT exhibit strong Raman scattering when the inter-band transition energy is in resonance with excitation laser, due to the unique van Hove singularities (vHs) in the density of states.²¹ Each peak in the radial breathing mode (RBM) region of the spectrum is a vibrational mode in the radial direction that probes SWNT with a certain chirality vector (n,m) and electronic structure. A Raman peak at 267 cm⁻¹, i.e. the RBM of the (10,2) SWNT, becomes more prominent as nanotubes form electronically-coupled aggregates and the interband transitions are subsequently broadened and shifted.¹⁰¹ The ratio of this peak to other

RBM, shown as an inset, is a relative measure of inter-tube coupling or bundle size, and is also plotted versus sensor number in ascending order (Figure 28b). We find that nanotube aggregation state, probed spectroscopically in this manner, is a much more effective predictor of chemical effectiveness except for sensors 8 to 11 in the apparent transition region. AFM images support this correlation. Figure 28c shows the AFM images of three representative sensors. The first is a reversible sensor just near the onset of percolation (i), while (ii) is a reversible sensor just above percolation. Lastly, (iii) is an irreversible sensor far above percolation. It is apparent that (i) is composed mostly of individual or small bundles of nanotubes. Also, (ii) and (iii) have similar overall aggregation states but (ii) has more current paths through individual nanotubes compared to (iii).

Bundling can inhibit reversible binding by creating sites of much lower potential for adsorption than the SWNT sidewall. A SWNT bundle has four possible adsorption sites: the external surface, external groove, internal surface, and interstitial channel.¹¹⁴ The external groove and interstitial channel are additional sites created upon bundling. Several studies^{115,116} predict significantly higher binding energy for these adsorption sites. Our molecular potential (MP) calculations and XPS results (discussed in the next section) support the idea that the aniline could reduce the binding energy of thionyl chloride by irreversibly covering the entire SWNT surface. Aniline molecules will presumably functionalize a SWNT bundle along the equi-potential surface, which still has groove sites.¹¹⁷ This could explain the chemistry failure for SWNT arrays with high aggregation states. This relationship between adsorption strength and array morphology explains the strong correlations of reversible behavior with sub-percolated networks, and low extent of bundling.

In previous work⁷⁶, we demonstrated that for a sparse SWNT network free from significant aggregation, the conductance change upon analyte adsorption increases linearly with the sensor conductance. A mass-action model of dynamic adsorption predicts this trend, which is due to the increase in surface area and binding sites for analyte adsorption. This assumes that each nanotube is an independent, isolated series of sites. However, when the array is dominated by large bundles, the behavior is different. Sensors with the highest current, corresponding to this regime, do not even respond to

analyte. In this regime, the surface area to current ratio is the dominant factor. For sensors with large bundles, current pathways exist with no connection to surface sites. We observe this trend during aniline treatment as well. The percent conductance change after functionalization with aniline was inversely proportional to the array conductance, suggesting that aniline adsorbs primarily to external sites of SWNT bundles (Figure 29).

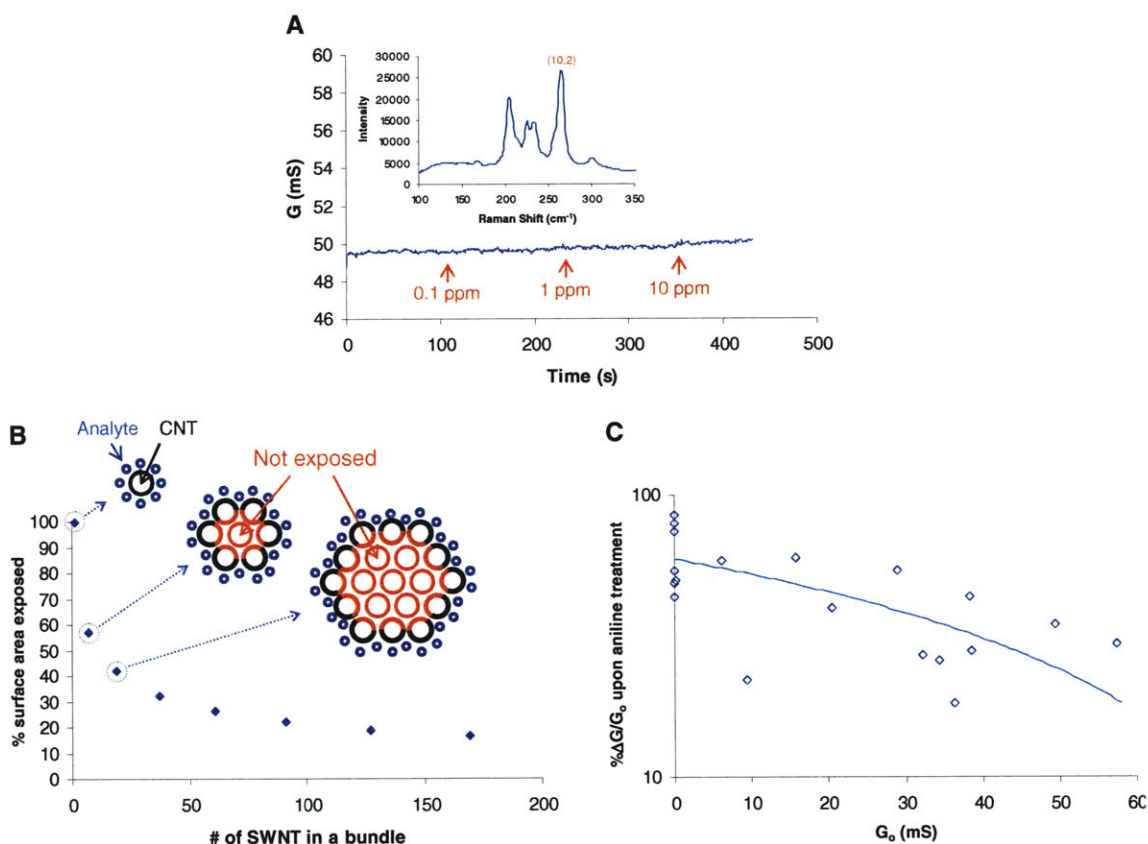


Figure 29. Reduced sensitivity for large bundles. (a) SWNT sensors with high current did not respond to thionyl chloride. High (10,2) RBM in Raman at 785 nm excitation (inset) confirms this high current is due to the large SWNT bundles. (b) % exposed surface area versus number of SWNT in a bundle is plotted, assuming uniform SWNT diameter and analyte adsorption only on external sites. Larger bundles have fewer adsorption sites per nanotube. No response in a) can be explained as such. (c) A similar trend is observed during aniline functionalization. % conductance change upon aniline functionalization is larger for the sensors with low initial conductance.

4.3. Sensing mechanism

Thionyl chloride, a strong electron acceptor, is expected to adsorb more strongly on metallic SWNT than on semiconducting SWNT due to high electron-charge density at the Fermi level.¹¹⁸ We performed *in-situ* Raman spectroscopy to test this (Figure 30a). The conductance (black line) drops upon aniline addition and stabilizes (~1250 s) after aniline evaporation (Figure 30b). Subsequent thionyl chloride injections, 1,000 ppm followed by 10,000 ppm, were made. Baseline-integrated RBM at 785 nm excitation, resonant only with semiconducting SWNT, was monitored in situ (blue line). Partial recovery was observed for both conductance and Raman signal, which changed in opposite direction to each other. This can be explained by increased hole carriers, and a decreased number of ground state electrons for photo-absorption upon electron-withdrawal by thionyl chloride. Raman spectroscopy at 632.8 nm excitation enables us to probe the effect of adsorption on metallic and semiconducting SWNT separately. Figure 30c shows baseline-integration of RBM, normalized by Si background peak, from aniline-functionalized metallic (green) and semiconducting (blue) nanotubes. Both types show partially irreversible decreases (conductance increase), seen in Figure 30b. The peak ratio of semiconducting to metallic SWNT is 0.71 initially, and 0.80 after thionyl chloride injection. We assigned this phenomena to the preferential charge transfer from metallic SWNT to thionyl chloride as discussed in our previous work.⁷⁶ However, the percent signal recovery after 10 min is 33% and 32% for semiconducting and metallic SWNT, respectively. We have therefore concluded that the desorption kinetics of thionyl chloride are indistinguishable with respect to SWNT electronic structure treated with aniline. Detailed change in the Raman spectra can be found in Figure 31.

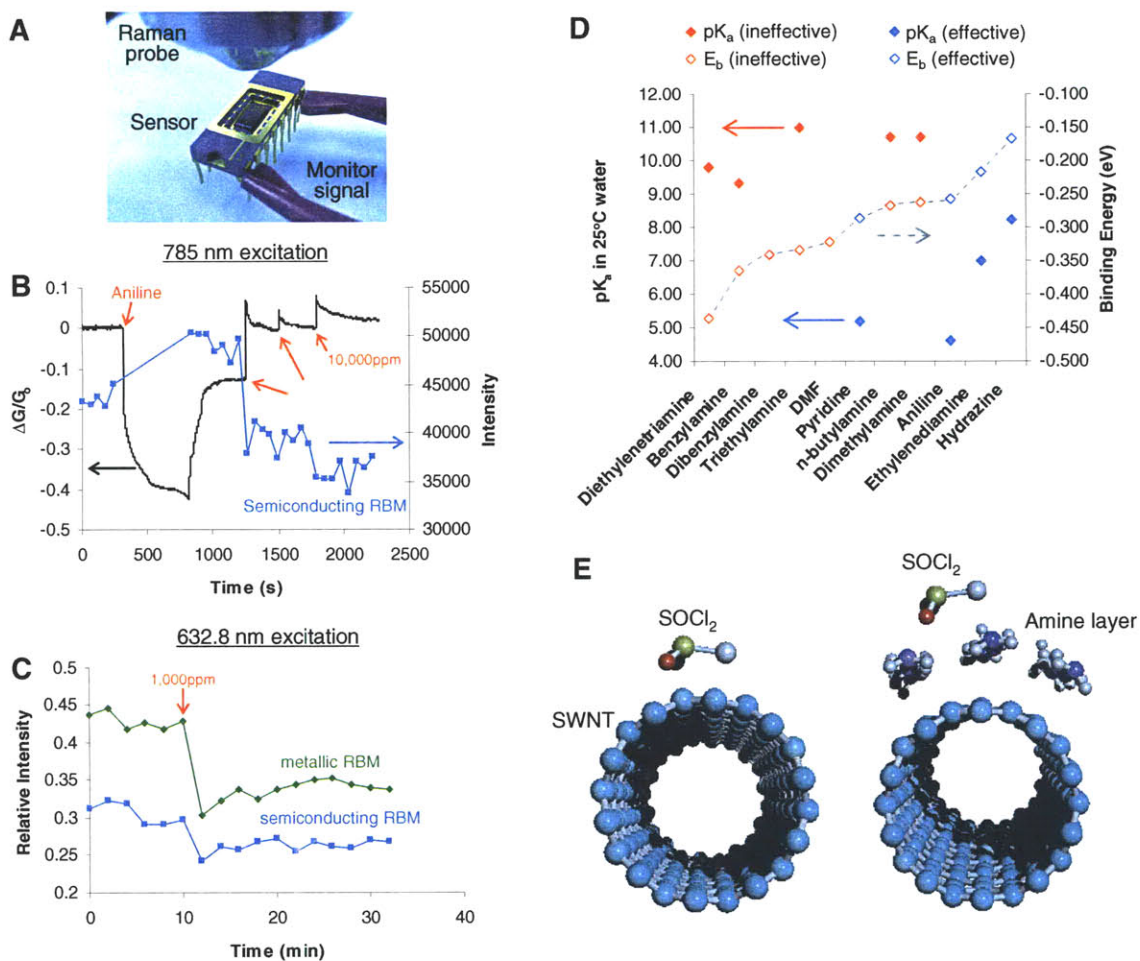


Figure 30. Proposed mechanism for tuned reversibility. (a) Picture showing in situ Raman on aniline-treated sensor exposed to thionyl chloride. (b) Baseline-integrated RBM (blue) from semiconducting nanotubes at 785 nm laser excitation, monitored in situ with conductance (black). (c) Real-time Raman at 632.8 nm laser excitation. Desorption kinetics of thionyl chloride does not differ between metallic (green) and semiconducting (blue) nanotubes. (d) pK_a of amine molecules tested, and the binding energy (E_b) between a thionyl chloride and a amine molecule calculated by molecular potential. Red and blue shapes represent ineffective and effective functionalization, respectively. Filled and open shapes correspond to pK_a on the primary axis and E_b on the secondary axis, respectively. Effective surface chemistry reduces the thionyl chloride binding energy, causing reversible responses. (e) Thionyl chloride adsorbed on a bare SWNT (left), and on a functionalized SWNT (right).

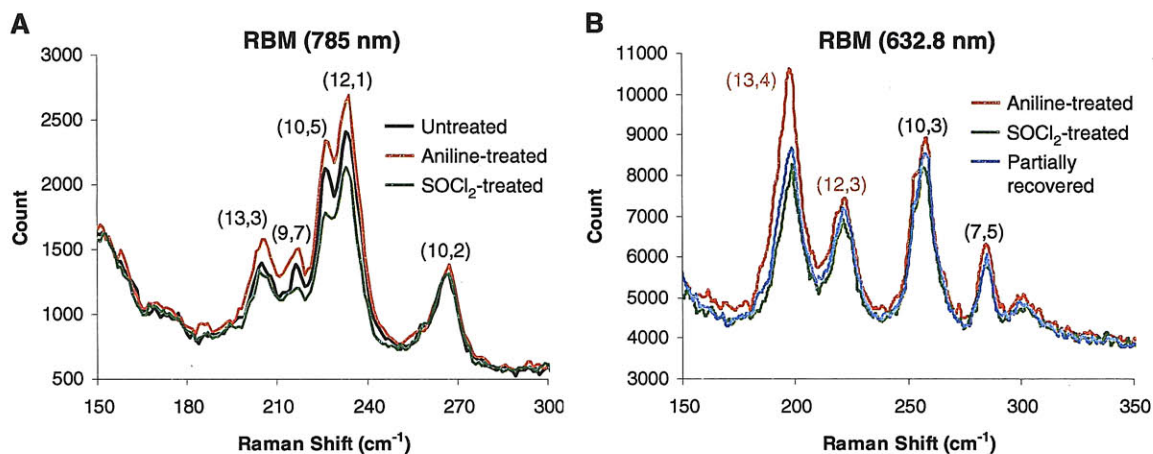


Figure 31. Changes in RBM upon chemical treatment. (a) RBM of a sensor tested in Figure 30b at 785 nm laser excitation. Only semiconducting SWNT are in resonance at this wavelength. Black, red, and green spectra are for untreated, aniline-treated, and thionyl chloride-treated sensor, respectively. Lone pair electrons in aniline n-dope the nanotube and increase the number of ground state electrons for photo-absorption. Conversely, RBM decays upon exposure to electron-withdrawing thionyl chloride. The change is more prominent in large diameter nanotubes due to the small band-gap and high density of electronic states (DOS) near Fermi level. (b) RBM of a sensor tested in Figure 30c at 632.8 nm excitation. RBM for both metallic (red indices) and semiconducting nanotubes (black indices) can be observed. The sensor treated with aniline (red) was exposed to thionyl chloride (green spectrum). As previously reported, most charge transfer occurs from large diameter metallic SWNT to thionyl chloride due to the high DOS at the Fermi level. Although there was a slight recovery after 20 min (blue), no difference in desorption kinetics was found between both electronic types.

Both small molecular weight and larger polymeric amines induce this conversion. The former can still have an n-doping effect on SWNT as documented for PEI functionalization.^{51,77} The primary y-axis in Figure 30d shows pK_a values for ineffective (filled red) and effective (filled blue) amine functionalities. Only amines below pK_a of 9 are apparently effective, suggesting a correlation with basicity. We first hypothesized that the change in reversibility was due to doping by the amine. In this scenario, amine molecules fill groove sites on SWNT bundles, leaving the external surface available for analyte adsorption. The increase in SWNT Fermi level by amines, however, would increase the SWNT-SOCl₂ binding energy. Hence, we abandon this hypothesis.

Molecular potential (MP) calculations were carried out on a (10,0) SWNT to understand the aniline interaction. Irreversible binding of thionyl chloride on a (10,0) SWNT does so with an energy (E_b) of -0.367 eV. The higher binding energy for an

aniline molecule ($E_b = -0.564$ eV) predicts that aniline irreversibly adsorbs on SWNT surfaces. The array conductance decreased permanently upon aniline addition, and the presence of strongly-bound aniline after evaporation was confirmed in X-ray photoelectron spectroscopy (XPS). Average atomic N/C ratio was 1.76 ± 1.61 % and 6.74 ± 3.23 % for 3 untreated and 11 aniline-functionalized sensors, respectively. Price and Tour¹¹⁹ recently reported SWNT functionalization with substituted anilines at 80 °C for 12 h in the presence of oxidizing agents, but we do not expect this reaction to occur in the milder conditions of our system. No noticeable increase in D-peak, a Raman signature of covalent functionalization of SWNT, was observed after aniline treatment. Monolayer aniline coverage predicted by MP corresponds to 27 aniline molecules for a 6.5 unit cell (10,0) SWNT. The estimated N/C ratio is 6.11 %, which is lower than 6.74 % in XPS. These results support that aniline irreversibly adsorbs upon the entire SWNT surface so that no bare SWNT surface is exposed for analyte adsorption.

Hence, thionyl chloride is expected to adsorb on the amine layer rather than on SWNT surface as illustrated in Figure 30e. The binding energy of thionyl chloride-amine complex was estimated using MP calculations for 10 different amines (Figure 30d, secondary y-axis, open shapes). No SWNT was involved in this calculation. The calculated E_b values were smaller for effective amines (blue) than for ineffective ones (red). Therefore we propose that amine functionalization reduces the thionyl chloride binding energy, resulting in reversible sensor responses. The amine layer in this system acts as a mediator for charge transfer from SWNT to thionyl chloride.

The possibility of a reaction between thionyl chloride and amine molecules was considered. It is well known that thionyl chloride readily reacts with amines under some conditions.^{120,121} The expected reaction products with aniline are N-sulfinyl-benzenamine and HCl.¹²² Reduction of thionyl chloride could also occur to form SO₂, S, and Cl⁻.^{123,124} Either case would affect the sensor signal by producing strongly bound reaction products or removing the amine layer. The MP calculations predict the E_b of N-sulfinyl-benzenamine, HCl, and SO₂ on (10,0) SWNT would be -0.669, -0.139, and -0.300 eV, respectively. The strongly-binding N-sulfinyl-benzenamine would especially cause an irreversible sensor response. Therefore, the stable baseline in Figure 23b suggests that these possibilities can be rejected. There was also no residual sulfur evident via XPS

from aniline-treated sensors exposed to thionyl chloride. This further supports the absence of the reaction (Figure 32). We speculate that this is due to the reduced basicity and reactivity of amines that have partial electron donation to the SWNT.¹²⁵ Conversely, ineffective amine treatments in Figure 30d, which are categorically stronger bases than those of the effective group, potentially react with thionyl chloride and form irreversibly binding species. Thionyl chloride in our system appears to functionally behave similarly to SO₂ molecules for probing the surface basicity.^{126,127}

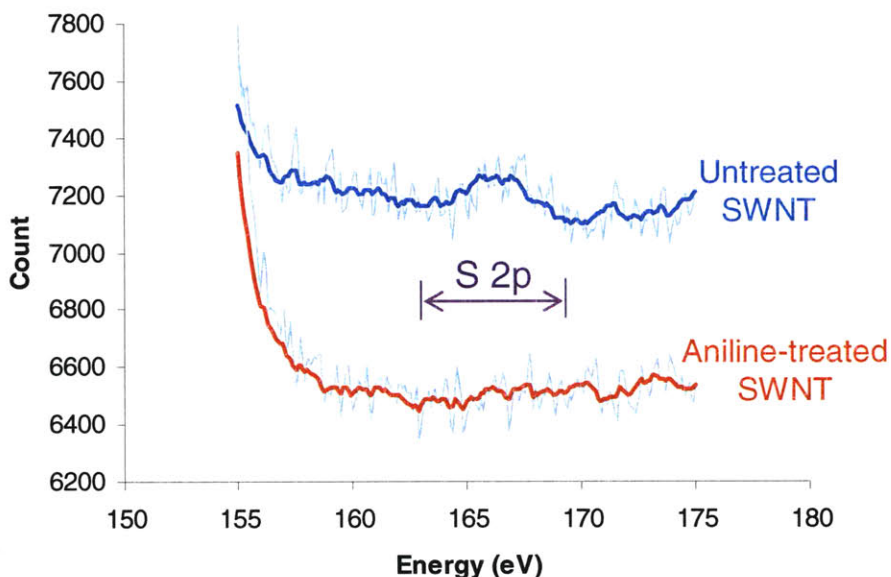


Figure 32. XPS from untreated and aniline-coated sensors after exposure to thionyl chloride. S 2p peak in XPS from untreated (blue) and aniline-coated (red) sensors, after exposure to thionyl chloride. Thionyl chloride responses from untreated sensors are irreversible. The presence of S 2p signal in XPS suggests it is due to the irreversible adsorption of thionyl chloride on SWNT. However, no signature of sulfur was found from aniline-coated sensors exposed to thionyl chloride. This supports the reversible responses from aniline-coated sensors. No sulfur residues along with little baseline drift in the sensor responses suggest the absence of reaction between thionyl chloride and aniline.

4.4. Polymer coating for enhanced sensitivity

If the amine moiety represents the new, reversible binding site, intermediate to the SWNT array, then a polymeric form should increase the detection limit of the system by increasing the number of sites per area. We find that the sensitivity to thionyl chloride

was dramatically improved by polyethyleneimine (PEI) functionalization (Figure 33a). Red and blue arrows denote thionyl chloride and air injections, respectively. A sharp signal increase was observed even at the ppb level, and the response was reversible with stable baseline. Regular air injections (as shown) were made to monitor any potential contamination in the injection system or background. Negative responses were observed from another sensor with a slight drift in the baseline (Figure 33b). We were able to detect a 5 s pulse of 10 mL thionyl chloride at 725 ppt (parts per trillion), which is the lowest concentration detected by a reversible SWNT sensor to date. We believe the sign of the signal is related to the extent of n-doping by PEI. Electron withdrawal by thionyl chloride from an n-type (p-type) array will cause a decrease (increase) in conductance by removing (introducing) the majority carriers. Figure 33c is a response curve from 5 representative PEI-treated sensors. The lowest detection limit, extrapolated to three times the noise level, is 25 ppt. This enhancement in sensitivity of over 3 orders of magnitude is also due in part by the Fermi level increase due to PEI doping, up to the most probable first vHs in conduction band (~ 0.516 eV from mid-gap for HiPco¹²⁸).

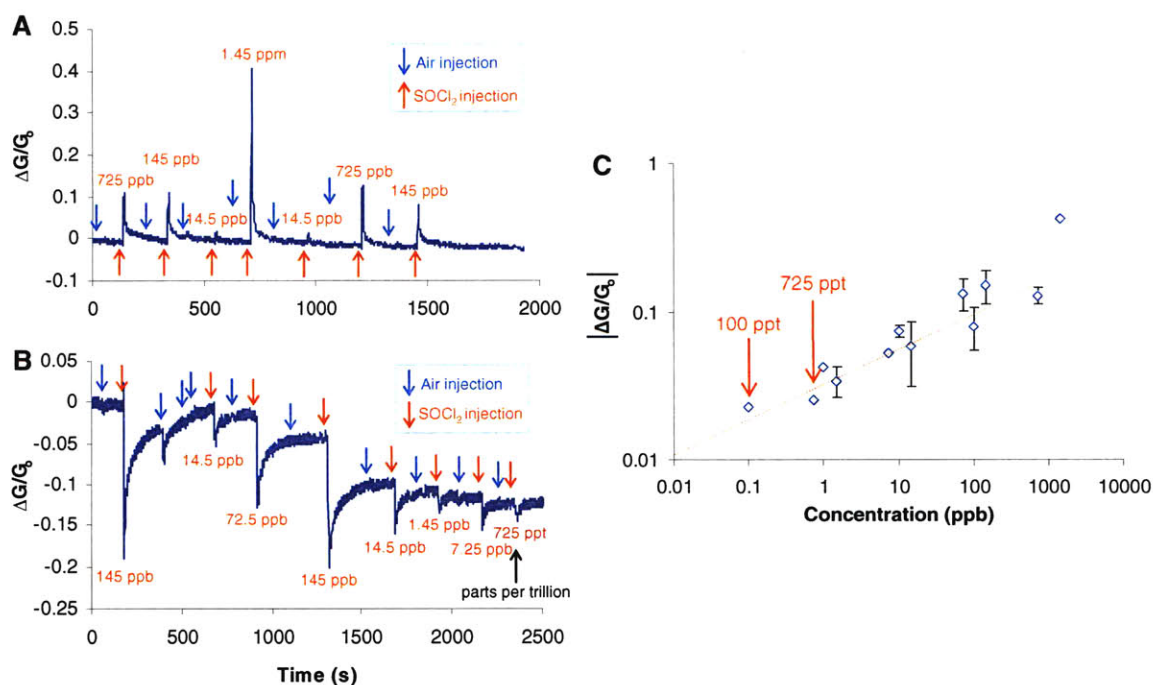


Figure 33. Enhanced sensitivity via polymer functionalization. Sensor response to thionyl chloride can be dramatically improved by PEI functionalization without losing the reversibility. (a) Positive responses to thionyl chloride. (b) Negative responses to

thionyl chloride showing ppt level detection. (c) Response curve from 5 PEI-treated sensors. The estimated detection limit, at 3 times the noise level, is 25 ppt.

4.5. Application of reversible sensors: integration with μ GC column

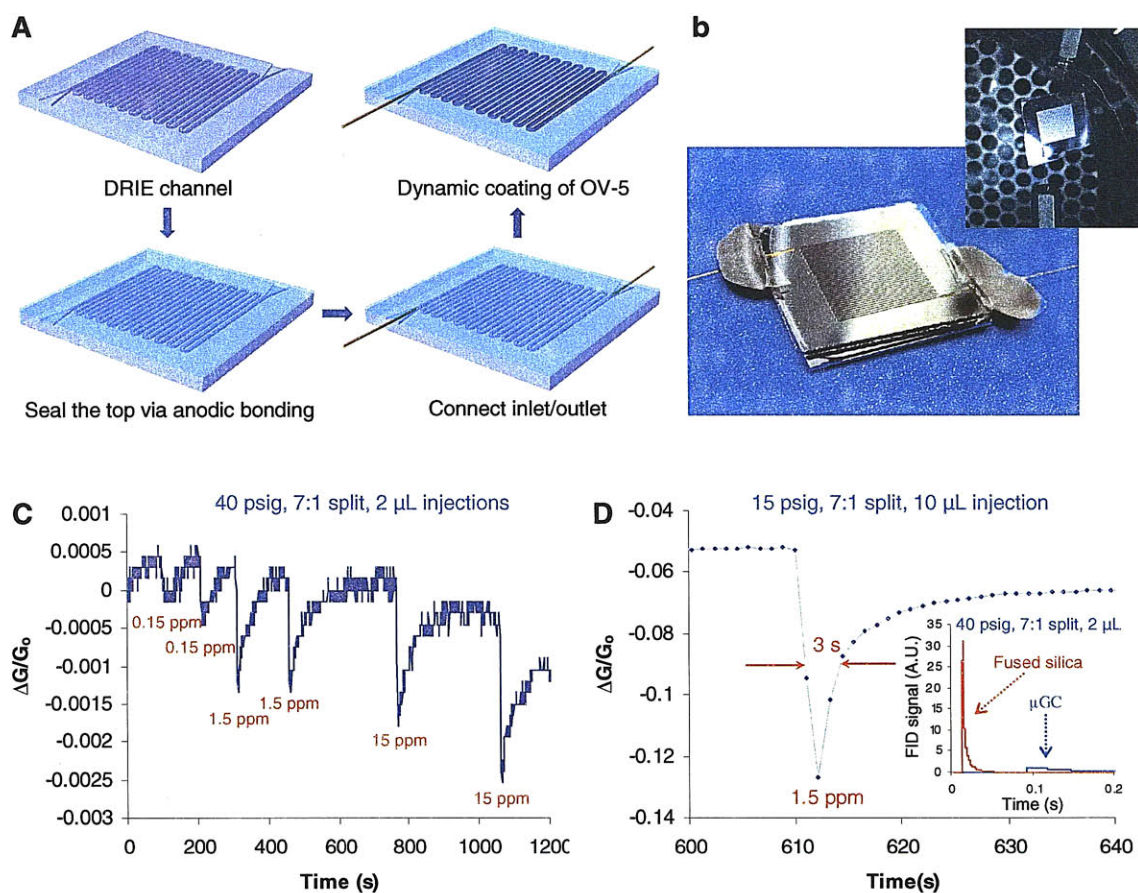


Figure 34. Application of reversible sensors with μ GC column. (a) μ GC column fabrication process. (b) Pictures of fabricated μ GC column connected to the injection port. (c) DMPP pulses through μ GC column detected by a polypyrrole-functionalized sensor. A 0.15 ppm pulse corresponds to 10^9 DMPP molecules. (d) Polypyrrole-functionalized sensor response to a DMPP pulse through conventional fused-silica column. The peak is much sharper (FWHM \sim 3 s) than the one from μ GC column (FWHM \sim 26 s). This is due to the peak broadening in μ GC column as confirmed in FID signal (inset)

Tuning the array to exact a rapid, reversible response with high sensitivity enables new applications for real time, dynamic detection using these systems. One example is a reversible SWNT array coupled to the outlet of a micro-fabricated gas chromatographic column (μ GC). Chromatographic separation and detection remains the analytical

standard for the detection of diverse classes of organic molecules. The advantage of such a micro-fabricated arrangement lies in the exceedingly small foot-print for molecular discrimination via column chromatography and detection with a rapidly transducing electronic array. We demonstrate that the SWNT network, when chemically treated as described above, has a response that is rapid enough to reversibly detect DMPP in real time from the end of a 30 cm, 100 x 100 μm μGC column.¹²⁹ In this case, polypyrrole was selected as a functionalization material for DMPP binding.¹³⁰ A slight conductance decrease was observed upon functionalization as expected. Control experiments with only polypyrrole on the electrode gap showed no response to DMPP.

Figure 34a-b outlines the μGC column fabrication and assembly. The outlet was carefully aligned above a polypyrrole-treated SWNT sensor. With H_2 carrier gas flowing at 40 psig, 2 μL of DMPP headspace was manually injected (<0.3 s) at 7:1 split, and the current was monitored at 0.1 V. GC oven fan was kept off for stable analyte flow. The injector and column temperature were 250 $^\circ\text{C}$ and 30 $^\circ\text{C}$, respectively. The sensor response (Figure 34c) is negative, and reversible with FWHM ~ 26 s. The 0.15 ppm pulse corresponds to $\sim 10^9$ DMPP molecules, and this number was confirmed with a flame ionization detector (FID). The ability of our experimental approach and detection limits to be independently verified by GC-FID – an analytical standard for determining gas concentrations – is unique, and provides high level of confidence in the reported absolute and relative detection limits. We note that the direct electrical transduction of 10^9 molecules in this manner has not been demonstrated before with any analytical platform. It is also noteworthy that this absolute detection limit was achieved with no physical coupling between the SWNT device and the micro-column, and hence, the value is an overly conservative estimate.

Figure 34d is a response to 10 μL of 1.5 ppm DMPP at 7:1 split at 15 psig using a 3 m long commercial fused silica column. The FWHM is as short as 3 s. This suggests the broad peaks in Figure 34d are due to the peak broadening in the μGC column. It is confirmed by a much broader FID signal from a μGC column than from a conventional fused silica column (40 psig, 7:1 split, 2 μL injection) (Figure 34d, inset). Future efforts will determine the applicability of the analytical approach to complex gas mixtures.

The response to DMPP from a bare SWNT array was reversible. The E_b of DMPP on (10,0) SWNT in MP calculations is larger than the E_b for thionyl chloride. The MP calculation gives the enthalpy of adsorption rather than the Gibbs free energy. Direct calculation of entropy was not available in MP. The entropy decrease upon adsorption is expected to be larger for DMPP than for thionyl chloride due to the size effect, as observed in alkane adsorption on SWNT.¹³¹ Thus, we attribute the reversible DMPP adsorption to the ΔG_{ad} increase by large entropy loss upon adsorption.

We have demonstrated the reversibility of SWNT gas sensor can be tuned by variation of the surface chemistry. Kinetic and thermodynamic parameters extracted from the reversible responses match calculated binding energy between analyte and surface functional group. It is proposed that irreversibly bound amine layers reduce the analyte binding energy. The absence of strong adsorption sites, such as grooves in a SWNT bundle, is a prerequisite for the amine functionalization to effectively reduce the analyte binding energy. Providing more adsorption sites by PEI functionalization enables both reversibility and ppt-level sensitivity to thionyl chloride. We show that such reversible sensors can be a part of an integrated, micro-fabricated and portable detector system. We have reversibly detected a pulse as small as 10^9 DMMP molecules at the end of a μ GC column. Future work will examine dynamic peak resolution of gas mixtures using this platform.

4.6. Experimental

- Sensor fabrication

Interdigitated gold electrodes with 5 μ m gap were patterned on a thermally oxidized Si wafer (600 nm SiO_2 , Montco Silicon Technologies) by photolithography. The electrodes mounted on a chip carrier were wire-bonded for electrical connection. HiPco SWNT (batch HPR 107.1) was suspended in 1 wt% sodium dodecyl sulfate (SDS) by 10 min sonication, followed by 4 h centrifugation at 30,000 RPM. AC-dielectrophoresis was performed to form a SWNT network. AC voltage (10 V_{pp} , 5 MHz) was applied across the electrodes, and ~ 1 μ L of SWNT solution was dropped onto the electrodes. SWNT

coverage was roughly controlled by deposition time. After shutting off the power the substrate was rinsed with 1 wt% SDS solution and DI water to remove residual SDS.

- Sensor functionalization and testing

Aniline and other amine functionalization: 1 μL aniline (Acros) was applied onto the sensor, followed by removal of excess liquid aniline after 3 min. The remaining aniline was evaporated, and the signal was stabilized before testing. All other non-polymeric amines were functionalized in a similar way.

PEI functionalization: PEI (Aldrich, Mn~423) was dropped onto the sensor and blown with ~ 15 psig N_2 stream. This forms a ~ 10 μm wet PEI film.

Polypyrrole functionalization: 5% aqueous solution of polypyrrole, doped with organic acids (Aldrich) was dropped onto the array and rinsed with DI water after 2 min.

Testing: A pulse of 10 mL thionyl chloride vapor at desired concentration was flown onto the sensors with non-polymeric amines or PEI layers (~ 1.5 mL/s). Polypyrrole-functionalized sensors were tested with DMPP in a GC. Saturated analyte vapor was diluted in series for desired concentration. Injections were made using a glass syringe to prevent corrosion and contamination. The array conductance was monitored at 1 mV unless specified. All functionalization and testings were done at room temperature air.

- MP calculations

Molecular potential calculations were performed using universal force field (UFF)¹³² and Gasteiger charge calculation¹³³ in a Cerius2 program.¹³⁴ We assumed the molecular geometry of deposited SWNT and amine molecules did not change in response to the analyte adsorption. For the bindings on SWNT, a 6.5 unit cell (10,0) SWNT was first optimized, and the energy of analyte or amine molecules was minimized with the SWNT fixed. For the amine-analyte interaction (Figure 30d), an amine molecule was optimized, followed by energy minimization of thionyl chloride with the amine molecule immobilized. Different initial orientations were considered to find the global minima. The binding energy (E_b) of molecule A on molecule B was defined as the amount of energy reduced by adsorption (i.e. $E_{b,A} = E_A(\text{adsorbed on B}) - E_A(\text{free})$).

- μ GC column fabrication

A 30 cm long channel with 100 μm x 100 μm cross-sections was fabricated using deep reactive ion etching (DRIE) of a silicon wafer. A Pyrex coverslip was anodically bonded to seal the channel. A fused silica column (ID = 100 μm) was used to connect the μ GC column from injector port to SWNT sensor. The column was then coated with ~100 nm OV-5 via dynamic coating.¹³⁵ This process is schematically outlined in Figure 34a.

Part II. Interior of single walled carbon nanotubes for single molecule transport

Chapter 1. Background

SWNT is a nanopore with aspect ratio higher than other types of nanopores by several orders of magnitude. This high aspect ratio cannot be achieved by any means of micro/nano-machining or fabrication techniques, and therefore allows studying interior transport of molecules whose characteristic time is too short to measure in pores with small aspect ratio. In order to understand the transport phenomenon inside the SWNT, it is important to understand how conventional nanopores have been used to understand molecular transport. SWNT nanochannels show unusual behaviors that are so complex and therefore not observed in synthetic systems. This chapter starts with basic operational principles of existing nanopore sensors, followed by basic concept of stochastic resonance, and review of previous carbon nanotube research on molecular transport.

1.1. Nanopore resistive sensing

Protein ion channels in cellular membranes are nm or sub-nm in diameter and can pass desired ions with high flux (e.g. $\sim 10^8$ ions/s for KcsA K^+ channel¹³⁶) and high selectivity. These ion channels play critical role in cell viability and metabolism by maintaining membrane potential and exchanging ions with cell environment. Ions must shed hydration shells in order to enter the pore, and normally ions cannot enter nanopores due to the high energy required for dehydration. In protein ion channels, however, oxygen atoms in carbonyl groups mimic the structure of hydration shells and hence minimize the dehydration energy so the ions can easily translocate.¹³⁷ Selectivity is obtained by pore charges as well as by the pore size. Pore opening/closing is regulated by structural change of protein activated by concentration gradient of ions.¹³⁷

Synthetic solid state nanopores with a few nm in diameter can be drilled through a membrane of thin silicon nitride using ion beams.¹³⁸ Although these pores cannot mimic complex structure of the selectivity filter in protein ion channels, their robustness may be useful in understanding biological systems in a controlled environment. Because of 1) the pore-size large enough for small ions such as K^+ and Cl^- to migrate with little barrier, and

2) small aspect ratio (~ 10 at most), characteristic transport time of the small ions is in ps-ns range, which is far shorter than the equipment time resolution ($\sim 4\mu\text{s}$). For this reason, applications of the solid state nanopores have been focused on detecting and sizing larger molecules (e.g. DNA¹³⁹⁻¹⁴², polyethylene glycol¹⁴³) which have longer transport time. The Holy Grail in the nanopore sensing area is fast/accurate sizing and sequencing of DNA¹⁴⁴, and the technique is being developed by several companies for commercialization.

The nanopore sensor operates by change of ion current, or resistance, as the pore is blocked by a blocker. The concept is shown in Figure 35. Electrolyte solution (usually KCl aqueous solution) is placed on either side of the nanopore. Upon application of electric field across the pore, small ions such as K^+ and Cl^- electrophoretically migrate to cathode (-) and anode (+), respectively, contributing to the baseline ion current. The small ions therefore are charge carriers when the pore is open (step 1 in Figure 35a-b). When a large ion or molecule (red ball, Figure 35a) enters the pore, the ion current drops sharply by ΔI (step 2) where ΔI corresponds to flux of charge carriers through the pore at ON state. While the blocker is being translocated, the current remains at OFF state. Duration of the blocked state is the dwell time (t_{dwell}) of the blocker, from which the velocity and thus the mobility of the blocker can be estimated. As soon as the blocker leaves the pore, there is a sharp current recovery to the baseline (step 3) because the pore is back to the ON state allowing flow of the charge carriers (step 4). An all-point histogram can be generated from the nanopore current response (right, Figure 35b). Each peak in the histogram represents a pore state, and average current decrease (ΔI) due to pore-blocking can be obtained from the distance between peaks. A single nanopore switches between two states, ON and OFF. Hence, presence of n peaks in the histograms suggests there are at least $n-1$ nanopores in the system.

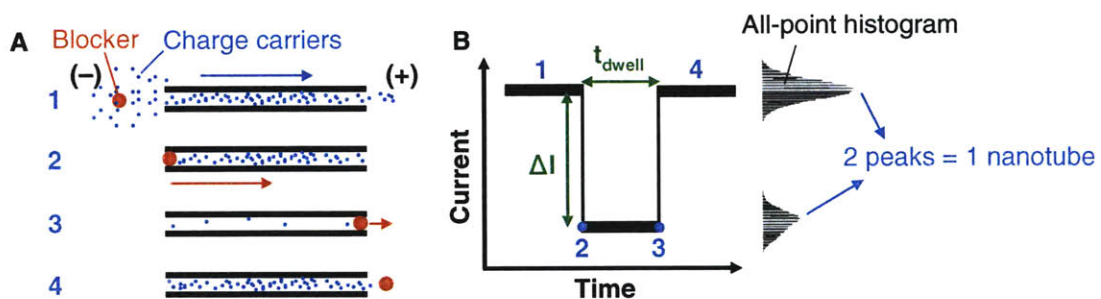


Figure 35. Basic operation of a nanopore sensor. a) Current is carried by small charge carriers (blue) while large molecules (blockers, red) block the pore. b) Current response. Baseline current is carried by charge carriers (state 1, 4). When the pore is blocked, the current decreases by ΔI (state 2, 3). All-point-histogram shown on right shows two distinct peaks which correspond to either open or closed state. n peaks suggest there are at least $n-1$ nanotubes in the system.

The nanopore blocking events can be simulated using rate constants for the blocker-in (k_{in}) and blocker-out (k_{out}). We assume that pore-blockings and openings from a pore are not affected by the presence of other pores. Simulated events for blockers with mobility of $10^{-6} \text{ m}^2/\text{Vs}$ translocating through a single $500 \text{ }\mu\text{m}$ -long pore are shown in Figure 36a. Rate constants of $k_{in} = 0.5 \text{ s}^{-1}$ and $k_{out} = 1 \text{ s}^{-1}$ are used, and ΔI is assumed to be 0.1 (arbitrary unit). As expected, the current transition takes place between only two states for the case of a single pore. When there are 3 pores in the system, $3+1=4$ current states in total are observed (Figure 36b). Hence, by comparing the simulation with experimental values of dwell time and open-channel lifetime, one can estimate the in/out rate constants for a specific blocker. It may be possible to use this information to identify various blockers such as DNA with different lengths and sequences.

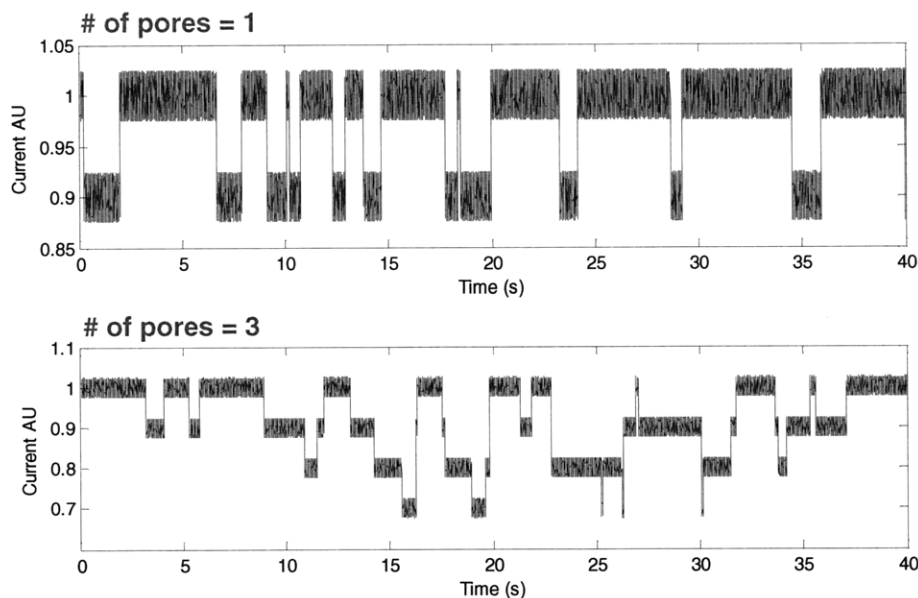


Figure 36. Simulated pore-blocking events for 1 pore (top) and 3 pore (bottom) systems. (pore length = $500 \text{ }\mu\text{m}$, blocker mobility = $10^{-6} \text{ m}^2/\text{Vs}$, electric field = 10^3 V/m , $k_{in} = 0.5 \text{ s}^{-1}$, $k_{out} = 1 \text{ s}^{-1}$)

A dwell time histogram can be generated by counting enough pore-blocking events. The t_{dwell} is determined by the pore length and the mobility of the blocker, which has to do with the blocker size with respect to the pore diameter as well as chemical interaction between the two. The t_{dwell} histogram shows a maximum at average t_{dwell} and with only few or zero counts near time zero. What determines the peak width and the tail is the kinetics of the blocker escape (k_{out}).

Distribution of the open-channel lifetime (open period between blocking events) can be quite different from that of the t_{dwell} because no minimum time might be required for blocker entrance. We limit our discussion in this paragraph only to single-pore devices. The ion current response will fluctuate only between two states. By looking at distribution of the open-channel lifetime, we can gain some mechanistic insight. The distribution is largely affected by how many open states are present. Let's first consider the case of single open state. The pore at closed state (C) changes to open state (O) with rate constant, k_{out} , and O becomes C with rate constant, k_1 (Figure 37a). Probability density function (PDF) for this case is $f_1(t) = k_1 e^{-k_1 t}$.¹⁴⁵ As shown in Figure 37b (blue), the distribution is maximal at time zero and decreases exponentially. There are cases when the blocker is going through different open states, whereas apparent ion current we measure remains stable at constant ON current. For example, a blocker can be either in bulk solution or interacting with functional groups at the pore-mouth. The ion current can still be ON as long as the blocker stays outside the pore, but obviously the blocker is in two different states (two open states, O_1 and O_2). If rate constants are k_1 and k_2 for $O_1 \rightarrow O_2$ and $O_2 \rightarrow C$, respectively, the PDF is a convolution of the two steps because they must occur in series. The PDF for the two open states is $f_2(t) = k_1 k_2 / (k_1 - k_2) e^{-k_2 t} - e^{-k_1 t}$.¹⁴⁵ The distribution is now skewed and shows a maximum (Figure 37b, green). Note the PDF is zero at $t = 0$. This means non-zero time is required for a pore to go through two open states in series. The PDF for three open states (O_1 , O_2 , and O_3) are further shifted to the right for the same reason (Figure 37b, red). In the literature, presence of two open states is observed in glutamate-gated channels in locust muscle membrane.¹⁴⁶ It should be noted that the distribution becomes broader and more symmetric as more open states are added. In case the distribution obtained by experiment is highly symmetric and narrow, however,

this approach cannot be applied because physical meaning of each state will be lacking as more open states are added.

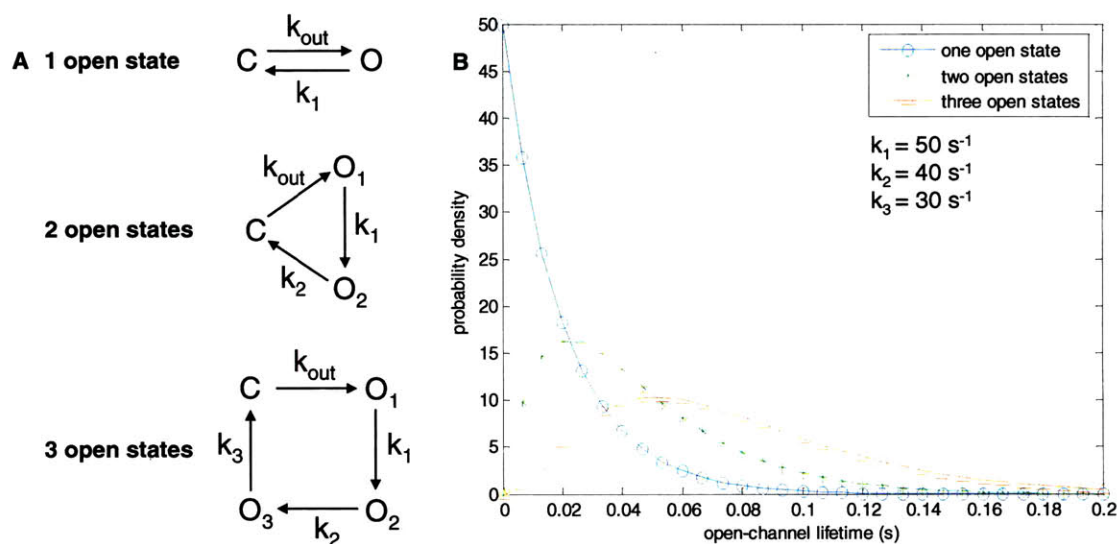


Figure 37. Probability density functions for open-channel lifetime. Open-channel lifetime at maximum probability density increases with number of open states.

1.2. Stochastic resonance

In most dynamic systems noise can bury signals and therefore is something to be removed or minimized especially when detecting small signals. However, there are cases where having noise can actually be beneficial in enhancing the signal-to-noise ratio. Stochastic resonance¹⁴⁷ is a phenomenon in which otherwise hard-to-detect weak signal is amplified by the noise either inherent to the system or externally added. There are three essential elements of the stochastic resonance: 1) presence of a threshold or energy barrier, 2) weak signal input (periodic or aperiodic), 3) noise in the system (added or inherent).¹⁴⁸ Since the stochastic resonance was first described by Benzi et al.¹⁴⁷ in 1981, the phenomenon has been not only found in many biological and non-biological systems but utilized to amplify weak signal in noisy synthetic systems.

Figure 38 illustrates the concept of the stochastic resonance. Let's consider a ball (shown red) sitting in one of the two potential wells at $x=-1$ in a bi-stable system (Figure 38a). The ball must overcome an energy barrier in order to move to the other potential well at $x=1$. When both of the potential wells are periodically driven up and down, the

barrier height will move up and down accordingly. If amplitude of the periodic forcing is not strong enough, the ball won't be moved to $x=1$ (Figure 38b). However, when some noise (shown as double-sided arrows in Figure 38c) is added to the same system, the ball can cross the barrier and move between $x=-1$ and 1 . Note that by adding noise we are able to amplify a weak input signal (weak periodic potential fluctuation) to a large output signal (transition between potential wells).

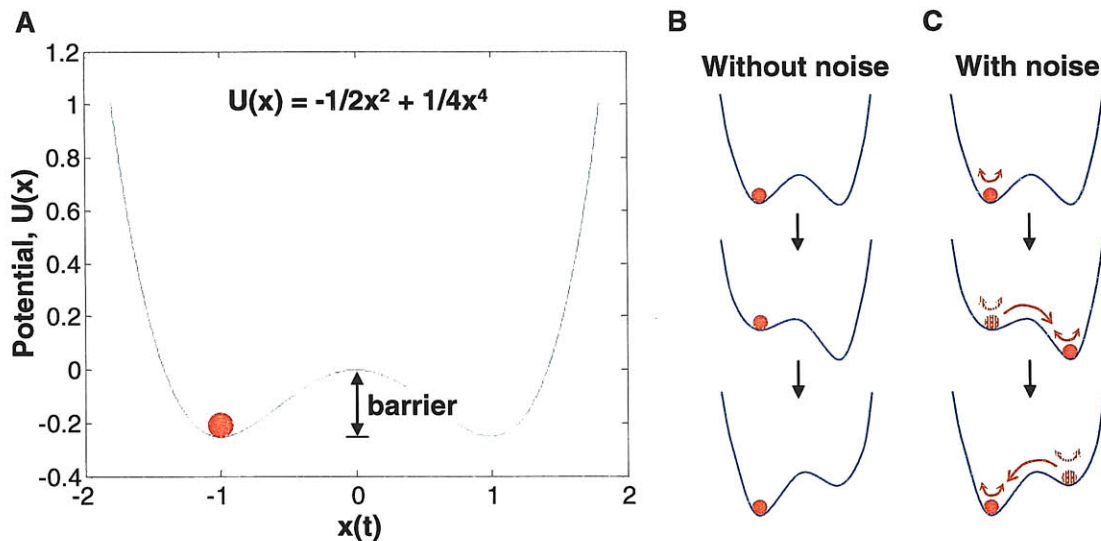


Figure 38. Basic concept of stochastic resonance. a) A bi-stable system with potential $U(x)$. A particle (red) placed at $x=-1$ must overcome the energy barrier in order to move to potential well at $x=1$. b) Periodically driven potential. The particle cannot overcome the barrier without any noise (left). With added noise, the particle can move back and forth (right)

Mathematically the stochastic resonance can be best described by Langevin equation for a periodically driven bi-stable system. Langevin equation for this system is shown below¹⁴⁷.

$$dx = [x(a-x^2) + A\cos\Omega t]dt + \varepsilon dW$$

The term $x(a-x^2)$ is a derivative of a bi-stable potential $1/2ax^2 - 1/4x^4$, and $A\cos\Omega t$ is a periodic forcing, where a and A are constants. W represents a Wiener process with ε determining the noise level. The periodic forcing $A\cos\Omega t$ is plotted in Figure 39a, along with solutions of the Langevin equation, $x(t)$, plotted in Figure 39b at 4 different noise

levels ($\varepsilon = 0.15, 0.21, 0.27,$ and 0.39 from top to bottom). When the noise level is low ($\varepsilon = 0.15$) the system stays in one potential well ($x=1$). The case is the same as in Figure 38b. A few transitions between $x=1$ and -1 occur at higher noise ($\varepsilon = 0.21$) although not as frequent as the periodic forcing. At higher noise, $\varepsilon = 0.27$, the transition frequency almost matches with the driving frequency, and the signal-to-noise ratio is maximized. Adding more noise to the system ($\varepsilon = 0.39$) causes too-frequent transitions and poor signal-to-noise ratio.

When the $x(t)$ is highly synchronized with the periodic forcing (as in $\varepsilon = 0.27$), dwell time histogram will show a single peak at $T/2$, where T is a period of the forcing. As the system deviates from perfect synchrony, multiple peaks will appear in the dwell time histogram at odd multiples of $T/2$.¹⁴⁹ This is because if a transition is once missed, the system must wait for the next forcing period.

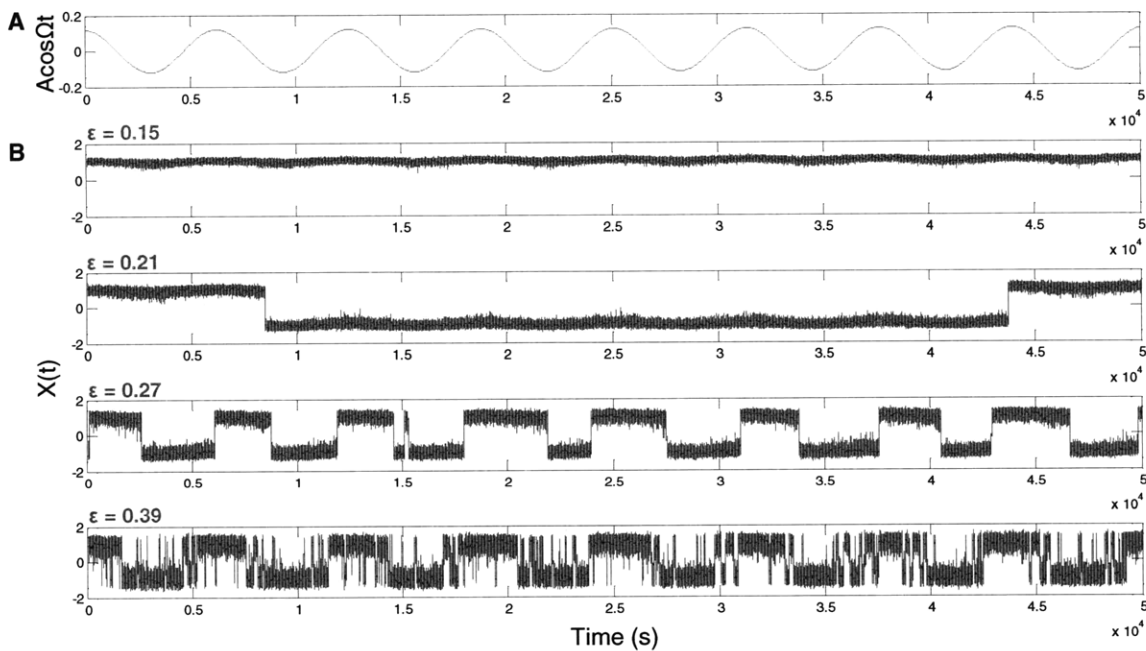


Figure 39. Solution of Langevin equation, $dx(t)=(x(a-x^2)+A\cos(\Omega t))dt+\varepsilon dW(t)$ as the noise level increases ($\varepsilon = 0.15, 0.21, 0.27, 0.39$ from top to bottom). $A=0.12, a=1, \Omega=0.001$. Signal-to-noise ratio (S/N) is a function of noise showing maximum at $\varepsilon = 0.26$ in this example. “S/N tuned in to noise” is a signature of stochastic resonance.

The concept, when first introduced by Benzi¹⁴⁷, was used to explain periodic recurrence of ice age every 100,000 years. The glaciation was explained to occur when

weak periodic wobbling of earth orbit around the sun is amplified by synergistic interaction with inherent noise such as daily/monthly weather change.

Stochastic resonance is found in many biological systems as well. Sensory neurons fire above a threshold and can detect environmental changes even in noisy environment.¹⁵⁰ Douglass et al.¹⁵¹ used a mechanoresonator to apply periodic water vibrations to crayfish tailfin, where vibration of hairs can be transferred to sensory neurons to detect the water vibration. They found that the water vibration alone was not enough to cause neuron firing. When the noise was added, however, the neurons fire periodically at optimal noise level. The experiment explains how the crayfish detects water vibrations created by its predators. Mechano-sensory systems in crickets use the stochastic resonance to protect from wasps.¹⁵² Rather than for protection, paddle fish use the stochastic resonance to detect electric signals from its preys, planktons.¹⁵³ The phenomenon was observed in ion channels as well. Bezrukov et al. demonstrated noise-induced large increase of signal-to-noise ratio using voltage-dependent ion channels formed by peptide alamethicin.¹⁵⁴ Hidaka and co-workers¹⁵⁵ found evidence of functional benefits of noise in the brain. They showed that homeostatic function in the human blood regulating system could be enhanced by adding noise. The result suggests it may be useful for biomedical applications such that externally added noise aid patients suffering from brain dysfunction. Another example of stochastic resonance can be found in human visual perception. Simonotto et al.¹⁵⁶ reconstructed a picture drawn in gray into a picture with black and white pixels. When noise, ξ , is added to the original gray color, I , if the $\xi + I$ is smaller than a threshold, the pixel was colored white. If the value is above threshold, the pixel was colored black. They found that there is an optimal noise level at which the best contrast for perception is achieved.

1.3. SWNT as a molecular transporter

Carbon nanotubes have atomically smooth surface and are predicted to be frictionless pipes due to graphitic surface where molecular corrugation is minimized by high density of atoms.¹⁵⁷ The result is a velocity slip at nanotube-molecule interface which will significantly enhance the molecular motion especially for channels with

confined geometry. Both experimental and theoretical results have shown much faster molecular transport than what is expected by continuum hydrodynamics.⁴⁵ Molecular motion along the carbon nanotubes exterior has been experimentally observed in several systems.¹⁵⁸⁻¹⁶⁰ Numerous theoretical¹⁶¹⁻¹⁶³ and experimental^{45,164-168} work demonstrate fast filling and transport of molecules through the interior of carbon nanotubes. However, all of these reports are based either on multi-walled carbon nanotubes where the Poiseuille flows maintain a parabolic velocity profiles¹⁵⁷ or on thin membranes of double/single-walled carbon nanotubes where the flow rate is limited by a large pressure drop. SWNT are unique because both the exterior and the interior are available for molecular transport. Diameter of the SWNT interior is only 1-2 nm, and thus provides unique opportunity for studying transport phenomenon at single molecule resolution, although constructing a reliable experimental platform has been challenging. In real applications as molecular transporter, a bundle or membrane of SWNT might need to be used to get enough molecular flux. However, it is important to understand the science at the level of individual nanotubes.

Carbon nanotubes are considered to be hydrophobic, and surfactants or polymer wrapping is required for suspension in water. However, the hydrophobicity is a macroscopic concept and may not be applicable at nanoscale.¹⁶² As a good example the contact angle of water on graphite, which is 80-90°, tends to decrease as the droplet size decreases. This explains the fast filling and transport of water in multi/double-walled carbon nanotubes. Molecular dynamics simulation predicts the filling of a first water molecule is not favorable thermodynamically, but filling the whole nanotube is favorable.¹⁶⁹ Without any applied electric field the motion of water molecules inside the SWNT is diffusive. The mode of diffusion can be Fickian, single-file, or ballistic. The Fickian diffusion where molecules pass each other chaotically may not be a main diffusion mechanism in SWNT interior due to the confinement. It is difficult for the water molecules to pass each other in the SWNT interior, and the diffusion can be single-file. If the movement of the confined water molecules is highly coordinated, the diffusion can be ballistic.¹⁶² The three diffusion mechanisms can be mathematically described as below.¹⁶²

$dr^2 \sim dt$	Fickian
$dr^2 \sim dt^{1/2}$	Single-file
$dr^2 \sim dt$	Ballistic

dr^2 is mean square displacement, and dt is time. Experimentally showing which mechanism is dominant will be difficult.

Experimentally studying molecular transport through the interior has been difficult due to equipment limitations and difficulty in fabricating reliable platform. For this reason, most studies of the interior transport have been done theoretically or using molecular dynamics (MD) simulations. Many researchers predict fast water transport through SWNT. Aluru group explains the orientation of $-OH$ in water molecules pointing toward the nanotube wall as well as the reduced hydrogen bonding near depletion region are the main reasons of velocity jump at the wall.¹⁷⁰ Water molecules confined in a nanochannel such as SWNT can form a 1D water wires. It has been known that proton conduction along the 1D wire occurs by “hop-and-turn” Grotthuss mechanism¹⁷¹ and can be highly efficient. Fast proton transport through SWNT was predicted by several researchers including Dellago et al.¹⁷² Theory also predicts that water inside the nanotube can form an ice-like phase.¹⁷³ This further supports the fast proton transport through SWNT because it is well known that the proton conduction is faster in ice than in water.¹⁷⁴

Nanotube exterior can be used for molecular transport. Zettl group demonstrated that pellets of indium metal on the exterior of multi-walled carbon nanotube (MWNT) can move along the surface by electromigration.¹⁵⁸ Temperature increased by high current ($\sim 50 \mu A$) can easily reach the melting temperature of the indium and facilitate the migration. They were also able to reverse the migration by changing the current direction. The electromigration was observed in SWNT network as well. Kuo et al. placed a droplet of water or glycol, and demonstrated the droplet moving toward anode (i.e. in the direction of electron flow). Thermophoresis is another mechanism of the external transport. Barreiro et al.¹⁵⁹ removed an outer shell of MWNT by electrical breakdown, except the region where a metal cargo was attached. The cargo moved as the current flowed. However, the cargo direction was independent of the current direction,

suggesting that the transport is driven by temperature gradient rather than flow of electrons.

The interior of carbon nanotubes can be filled as shown in SWNT peapods¹⁷⁵⁻¹⁷⁷. Several groups experimentally demonstrated interior molecular motion. However, most of the measurements were performed using either individual MWNT or membranes of DWNT/MWNT. A single MWNT (diameter 60-160 nm) embedded in a 1 μm -thick epoxy film can be used as a Coulter counter for polystyrene nanoparticles.^{178,179} Basic principle of operation is the same as the nanopore resistive sensors. Ion current through the MWNT drops as nanoparticles block the pore. Since the current decrease (ΔI) is proportional to the nanoparticle-to-nanotube diameter ratio, the device can be used to count and size the nanoparticles. Yan et al.¹⁸⁰ observed translocation of individual DNA using silica nanotubes. They observed both positive and negative ΔI as the DNA goes through. They attributed this ionic current crossover to the introduced counterions to the nanotube due to surface charges on DNA.

Vertically grown MWNT or DWNT can be sliced into a membrane for studying the interior transport. Hinds group measured flow rate of water and several hydrocarbons through a MWNT membrane upon application of pressure, and demonstrated enhanced flow with slip length of 3-70 μm .¹⁶⁶ Holt et al.⁴⁵ took a similar approach to demonstrate fast water and gas transport through a DWNT membrane. The slip length in their system was 140-1400 nm. Fornasiero et al.¹⁶⁷ demonstrated that these membranes can effectively reject ions from entering the pore. The % rejection values were reported for several ions dissolved in water. The results indicate that membranes of vertical carbon nanotubes can find applications in water desalination and purification.

So far only TEM studies allowed real time imaging of molecular motion inside the nanotube. A short nanotube capsule inside a longer host nanotube was shown to move back and forth along the tube axis, which the authors called linear molecular motor.¹⁸¹ MD simulation suggests the motion is driven by thermal energy provided by high power electron beam during TEM imaging. As shown in the exterior transport, the electromigration can be used for interior transport as well. Zettl group was able to move iron nanoparticles back and forth inside a MWNT at $\sim 25 \mu\text{m/s}$, and proposed an application in archival memory devices.¹⁸²

All of the experimental work on molecular transport in the nanotubes either used multi-walled carbon nanotubes with dimension much larger than the molecular size or performed ensemble measurements using membranes. None to date have experimentally confirmed interesting transport properties of SWNT predicted by theory such as fast proton transport, fast ion transport, rejection of ions, etc. Understanding the transport at the level of single molecule and single SWNT is important for future SWNT applications as molecular transporter.

Chapter 2. Preventing exterior transport of ions

Since molecular transport along SWNT can occur both externally and internally, in order to study the interior transport it is important to verify whether there is any exterior transport in our system. If the exterior transport does exist, it must be prevented to unambiguously study the interior transport. In this chapter, we show that aqueous solution of ions can transport along the exterior of SWNT. The exterior transport can be suppressed by covering the exterior with thin films of electrochemically inert materials.

2.1. Evidence of molecular transport on SWNT

It is crucial to carefully design an experimental platform to quantify transport of small amount of molecules. We have decided to use CVD-grown nanotubes rather than solution-processed ones. CVD-SWNT have advantages in easy alignment, ultra-long growth, free of surfactants on their surface. Nanotubes directly grown on a silicon substrate are also more suitable for micro fabrication process. We were able to grow cm-long and aligned nanotubes using laminar flow of CH_4 and H_2 as shown earlier.

Figure 40 shows our experimental platform to verify whether there is any external transport. Aligned nanotubes are grown by CVD on a silicon substrate. Center portion of the substrate is then protected by photoresist, followed by oxygen plasma etching to etch out nanotubes in unprotected region. Removing the photoresist in acetone leaves open-ended nanotubes about 2 mm-long (Figure 40a). An SEM image after the plasma etching clearly shows etched nanotubes (Figure 40b).

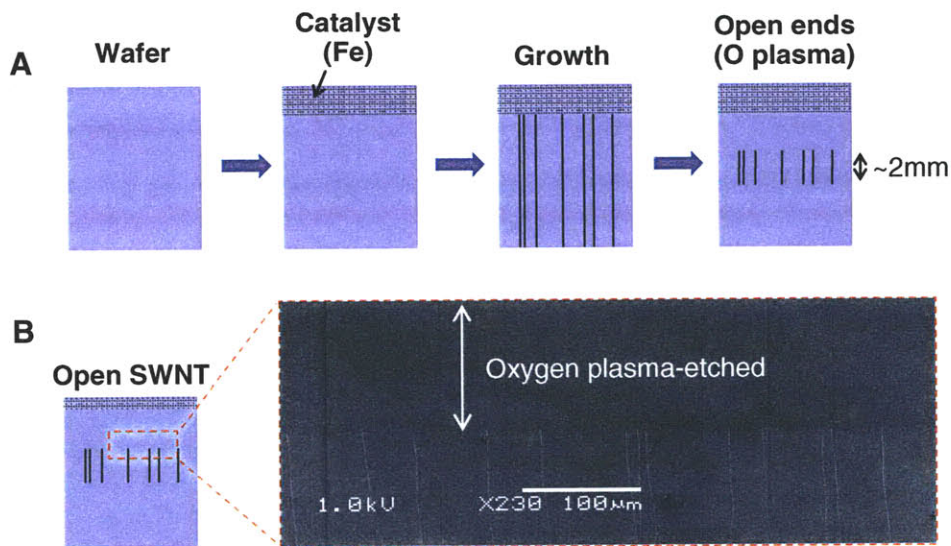


Figure 40. Device fabrication to verify external molecular transport. a) A film of Fe catalysts is deposited at one end. Aligned array of SWNT is grown by CVD, followed by plasma etching to open the ends. Tube length for this study is about 2 mm. b) SEM image of etched nanotubes.

We have performed a proof of concept experiment where NaCl aqueous solution is used for transport. Several aligned nanotubes are grown on a silicon substrate, and both ends are opened by oxygen plasma etching as shown above. With a NaCl droplet at one end and a water droplet at the other end, electrical bias is applied across the droplets (Figure 41a). Initially the current rapidly decreases (data not shown). This initial decay is associated with ion consumption at the Pt electrodes (H_3O^+ at cathode, Cl^- at anode). As charges are built up in each droplet, further ion current is suppressed unless there is an ionic transport between the droplets. Therefore, the current increase in Figure 41b is an indication of ion transport along the nanotubes. We have applied the bias until both droplets become dry and found salt crystals in water side (SEM image, Figure 41c). Elemental analysis by energy dispersive X-ray spectroscopy (EDX) proves the presence of Na (33 atomic %) and Cl (37 atomic %) transported along the nanotube surface (Figure 41d). The transport of ions can be either internal or external, or a combination of both.

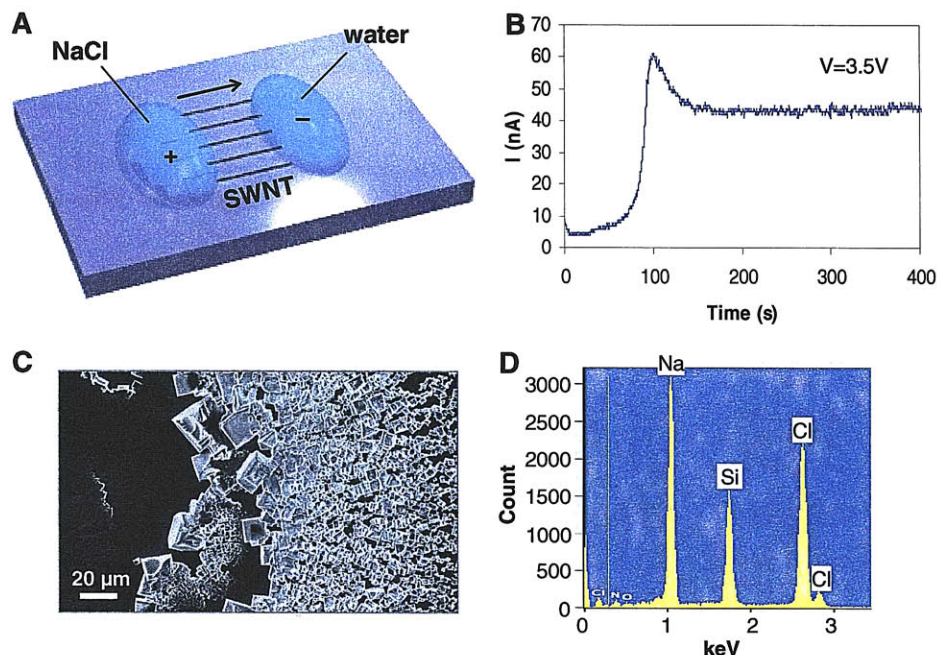


Figure 41. Evidence of ionic transport through SWNT. a) Initial experimental platform for the study of electroosmosis, b) Typical ion current from the system in a), c) SEM image of NaCl crystals found in the dried water droplet, d) EDX confirms the NaCl transport

Electroosmosis is the motion of polar molecules along a narrow channel in the presence of electric field. It has been widely studied for capillary electrophoresis for separation purposes.^{183,184} In our system water or NaCl aqueous is placed at both ends of aligned and open-ended SWNT, and an electrical bias is applied across the liquid droplets (or reservoirs). Studies of electroosmosis in SWNT has been limited to molecular dynamics (MD) simulations^{185,186}, and experiments are again performed using a membrane of multi-walled carbon nanotubes^{187,188}. In the experiments shown in Figure 42, the interior transport, if there is any, should occur mainly by the electroosmosis. Unlike electrophoresis where ions migrate to the electrode with opposite charge to themselves, the electroosmotic flow causes both cations and anions move in the same direction due to confined geometry. Exterior transport of ions on a surface occurs by surface diffusion, molecular layering¹⁸⁹ of liquids, and electrophoretic force. With an electric field applied, cations and anions on a large surface move in the opposite direction. However, the situation can be quite different for the case of nanoscale objects.

The EDX result suggests that migration of both anion and cations is unidirectional on nanotube exterior.

2.2. Evidence of exterior molecular transport on SWNT

We have verified that there is a significant contribution of external molecular transport to the ion current when carbon nanotubes bridge the droplets. SWNT array is etched so the length is 1 mm. 3M of NaCl aqueous solution is dropped on both ends of nanotubes, and 40 V is applied across the droplets until both become dry. Figure 42a is an SEM image of the sample after the experiment. Bright lines are observed along the nanotubes, and zoom-in of the anode (-) side shows NaCl crystals formed on nanotube surface (inset). Crystals do not form on nanotubes on cathode (+) side at this experimental condition. Bright lines could indicate the path of ion transport, which is along the nanotubes, and the crystal on nanotube is a direct proof of exterior transport. We find that the exterior transport can be prevented by covering the nanotube surface with another material. Similar experiment was performed with a 60 nm-thick layer of gold or SiO₂ on top of the 2 mm-long nanotubes. SEM image in Fig 42b clearly shows that only the uncovered region has bright lines along the tubes. If the bright lines are caused by molecules/ions carried along the SWNT exterior, the result confirms that the exterior transport can be suppressed by covering the exterior. Low ion current when the surface is covered further supports our claim. It should be noted we have demonstrated only the exterior transport, and the presence of interior transport is still unknown.

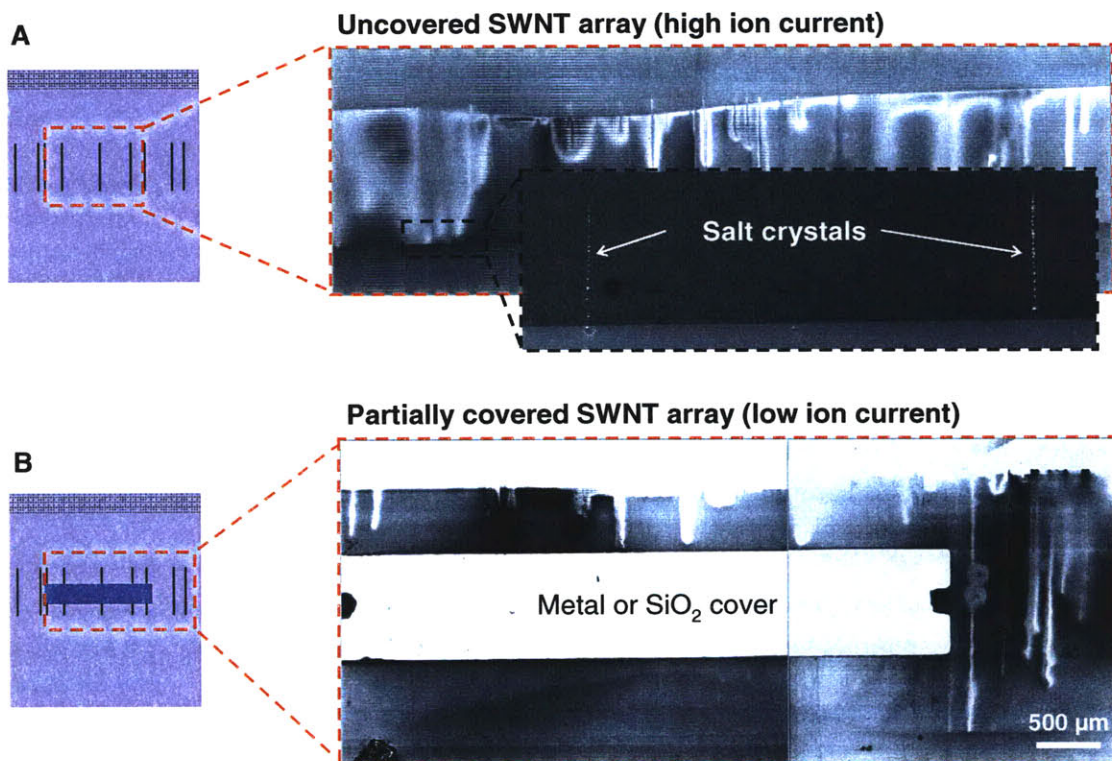


Figure 42. Evidence of external ion transport. a) 40V was applied across 3M NaCl droplets at each ends of 1 mm-long SWNT array. SEM image after the experiment is shown. Crystals form along the nanotubes (inset). b) Bright lines do not connect all the way when the nanotubes are covered.

2.3. Problems caused by exterior transport of ions

Although this experimental platform gave us useful information about the exterior transport of ions on nanotubes, it also has several problems which prevent us from exploring the interior molecular transport and the electron wind force idea. One of the problems is the nanotube damage during the experiment as shown in Figure 43a-b. We find that many nanotubes are cut during the experiment. Careful examination in SEM tells that the damage occurs at substrate-air-nanotube interface. Repeating the experiment under nitrogen blanket does not prevent the damage.

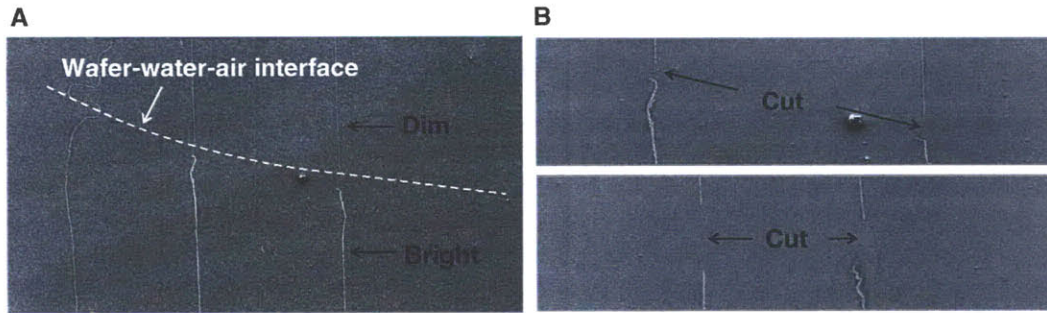


Figure 43. SEM images of nanotubes after the transport experiment. a) nanotubes are cut at wafer-water-air interface. b) Zoomed in images of damaged nanotubes.

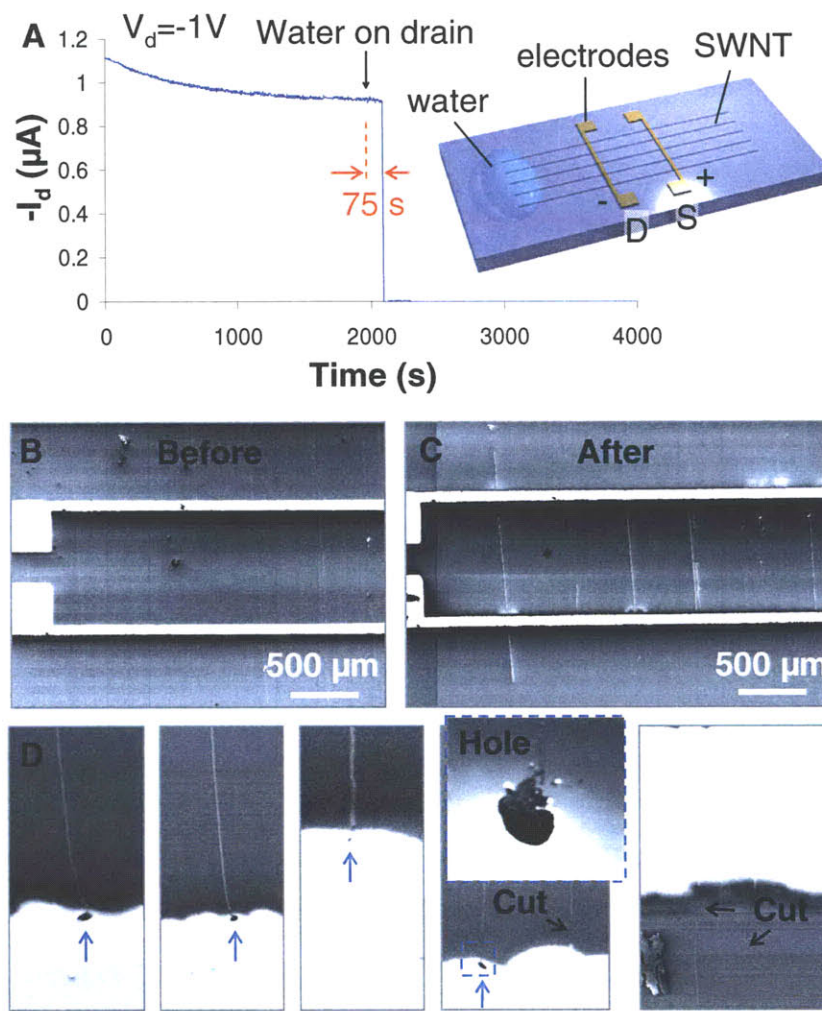


Figure 44. Exterior transport damages electrodes as well. a) Water droplet is placed at one end of SWNT while electrical bias is applied at the electrodes. Current became zero ~75 s after dropping water. b) SWNT across electrodes before the experiment, c) SWNT after experiment, d) Holes at nanotube-electrode junctions, and damaged nanotubes

The exterior transport damages the electrode-nanotube contact as well. The experimental platform is drawn in Figure 44a. Source (S) and drain (D) electrodes are deposited on the unopened nanotube array. With a bias ($V_d = -1V$) across the electrodes a drop of water is placed at one end of unopened nanotubes. Surprisingly, the current dropped to zero after ~ 75 s. SEM images before (Fig 44b) and after (Fig 44c) the experiment again show the bright regions along the nanotubes, an indication of the exterior transport. Curiously, the bright lines can be observed from nanotubes between the two electrodes, and large bright spots are found at nanotube-electrode junctions. The results suggest that the current drop could be due to penetration of water through the electrodes. By carefully examining the nanotube-electrode junctions we have found several holes at the junctions, an indication of electrode damage perhaps by electrochemical reaction with water and ions. For some SWNT-electrode contacts that remain undamaged, nanotubes are found to be damaged. This type of device failure has not been reported in any of the nanotube publications. In order for the electrode damage to occur water molecules need to spontaneously reach the SWNT-electrode junction by molecular layering on SWNT surface. Brochard¹⁹⁰ modeled the spreading of liquid drops on thin cylinders. The governing parameters are the “spreading coefficient”, S , and the critical value of it, S_c .

$$S = \gamma_{SO} - \gamma_{SL} - \gamma$$

$$S_c = 3/2\gamma(a/b)^{2/3}$$

where γ_{SO} and γ_{SL} denote the interfacial energies between solid/air and solid/liquid, respectively. γ is the liquid/air interfacial tension. a and b are respectively the molecular size and the cylinder radius. When $S > S_c$, the molecular layering proceeds to the entire cylinder length. For SWNT $S_c/\gamma \sim 1$ since $b/a \sim 2.5$. The theory does not explain our results since $S < S_c$ if we use γ values from the existing literature which was obtained from large amount of nanotubes (bundles or films). As discussed earlier, there may be significant difference in the surface tension between bulk and individual nanotubes. More study is needed to understand the molecular layering on the SWNT surface, but it is beyond the scope of our study.

Chapter 3. Interior transport of ions: stochastic resonance in SWNT ion channels

Rhythmic behavior and synchronization with internal/external stimuli are observed in both biological and non-biological systems in nature: heartbeat¹⁹¹, light-dark cycle¹⁹², brain waves¹⁹³, recurrence of ice age¹⁴⁷, dynamics of animal population¹⁹⁴, etc. In human body disruption of the rhythm is associated with diseases and symptoms such as insomnia, sinus node dysfunction, and Parkinson's disease¹⁹⁵. Medical devices including pacemaker and ventilator electrically/mechanically drive an arrhythmic body part at a desired frequency and help it re-synchronize. Understanding and devising the rhythmic process in a synthetic system, especially at small scale, is therefore not only of great scientific interest but important for potential applications in portable, implantable, and energy efficient biomimetic oscillators. However, it has been difficult to artificially mimic this spontaneous and complex rhythmic behavior.

Single walled carbon nanotube (SWNT) is a nanoscale tubular carbon material with both exterior and interior surfaces. Since the discovery of the SWNT in 1993¹⁹⁶, vast majority of studies have focused on the exterior due to easy access for modification and characterization. Properties of the interior, however, still remain largely unknown. TEM studies verified that the SWNT interior can be filled as shown in SWNT peapods¹⁷⁵ and SWNT with a single organic molecule¹⁹⁷. *Ensemble* measurements from membranes of double and multi-walled carbon nanotubes demonstrated rejection of ions¹⁶⁷ as well as fast transport of gas and water^{45,198}, which agree well with theoretical predictions^{162,199}. As for the motion of *individual* ions along *individual* nanotubes, however, there have been only speculations based on molecular dynamics simulations¹⁸⁶. Theory also predicts fast proton conduction along the SWNT interior¹⁷², but no experimental evidence has yet been provided.

3.1. Reliable experimental platform for the study of interior transport

We have designed an experimental platform by which the interior transport can be unambiguously characterized. The process is shown in Figure 45. First step is to grow an array of ultra-long aligned nanotubes using CVD as described earlier (SEM image). We

follow the procedure in Lin et al.²⁰⁰ to fabricate an epoxy structure with two compartments using photolithography. SU-8 2050 was poured and spread onto a silicon wafer with 300 nm thermal oxide at 80 °C so the epoxy thickness was about 1.5 μm. Temperature was raised slowly up to 120 °C. After 8-10 hr of annealing the substrate was removed from the hotplate and cooled down to room temperature. A structure with two compartments was patterned by UV exposure at 4.5 mW/cm² for 30 min. Developed structure was then released in HF solution. The released structure was placed onto the SWNT sample, and UV glue was dropped at the structure-wafer interface. The glue fills in the gap between the epoxy and the substrate by capillary action. The sample was then exposed in UV to cure the glue. Next step is to open both ends of nanotubes in oxygen plasma. The epoxy structure in this step serves both as a mask during the plasma etching and as an efficient blocker of the exterior transport. The compartments were then filled with aqueous ionic solution (NaCl, LiCl, KCl). Ion current was monitored with electric field across the reservoirs (Axopatch 200B, 2 kHz Bessel low-pass filter, 250 kHz acquisition frequency).

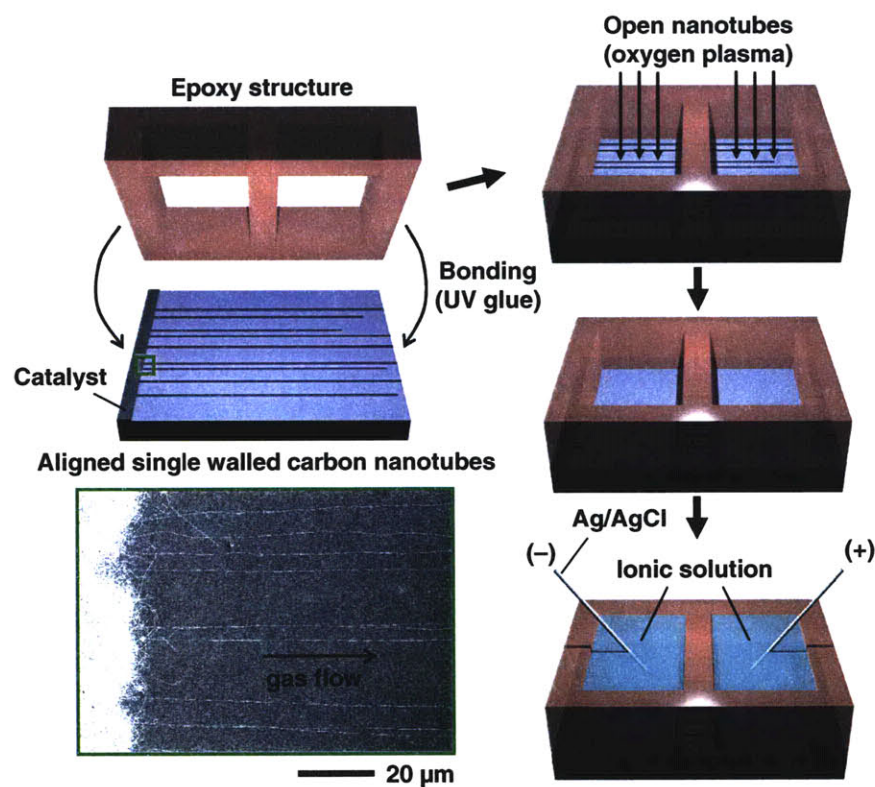
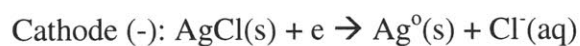


Figure 45. Experimental platform for studying interior transport. Ultra-long aligned nanotubes are grown on a substrate by CVD. Patterned epoxy well is glued onto the substrate. Tubes are then open in plasma etching. After filling both compartments with ionic solution, electric field is applied with ion current monitored in real time.

It is important to understand migration of which ions is causing the current that we measure. Figure 46 is a side view of our experimental platform. Ionic solutions of NaCl, KCl, or LiCl are connected via array of open-ended SWNT. Ag/AgCl electrodes are used to apply electric field across the reservoirs. Using Ag/AgCl electrodes minimizes the electrode polarization and therefore allows stable ion current measurement. Electrode chemical reactions at cathode and anode are shown below.



Chloride ions are consumed at anode (+) and released from AgCl at cathode (-). For channels much larger than the size of ions, there will be counter-migration of cations (Na^+ , K^+ , or Li^+) and anions (Cl^-) to the electrodes with opposite polarity. However, for single walled carbon nanotubes with the diameter comparable to the size of individual hydrated ions, the ion migration may experience some resistance. We need to consider charges at the pore-mouth as well as the dehydration energy barrier to verify which ions will be translocated. Details will be discussed in the following chapter.

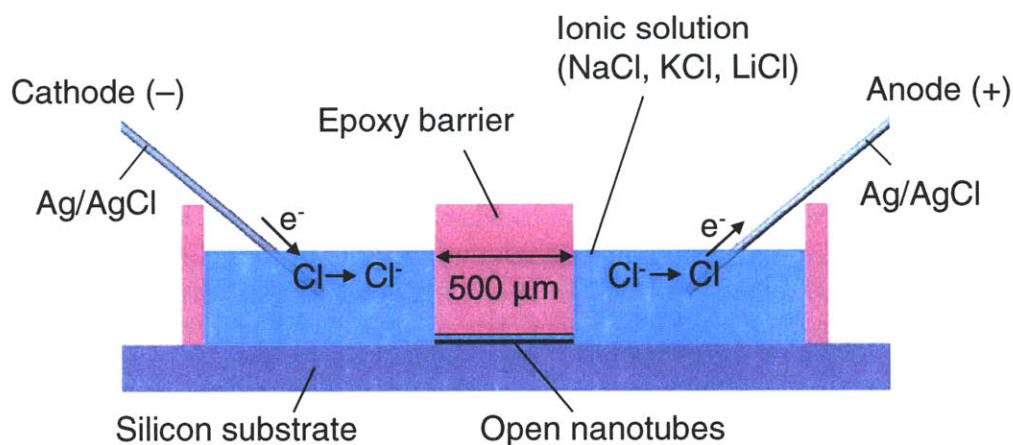


Figure 46. Side view of our experimental platform. Two reservoirs of ionic solutions are connected via open nanotubes. Cl^- is released at cathode (-) and consumed at anode (+).

3.2. Interior transport of individual ions

Figure 47a is a current trace at 0.3 V (600 V/m) across reservoirs of 1M NaCl connected via arrays of 500 μm -long nanotubes. As well documented in the studies of biological ion channels and solid-state nanopores^{144,201}, sharp decrease (recovery) of the ion current is a signature of stochastic pore-blocking (opening). The step height, or the conductance decrease (ΔG), is the amount of reduced flux of charge-carrying species upon pore-blocking. Velocity and thus the mobility of the blocker, in case the blocker translocates through the nanotube, can be estimated from the width of the downward peaks. Each peak in all-point histogram (Figure 47a, right) corresponds to a pore-state. Presence of 3 major states suggests the events are from at least 2 nanotubes. We noticed that there is a threshold voltage above which the pore blocking events are first observed. For each sample there is an optimal voltage to observe the events, and we tune to this region each experiment. By carefully adjusting the bias we are able to see current fluctuations between two states only of conserved ΔG (Figure 47b), which is indicative of single-tube phenomenon¹⁴⁵.

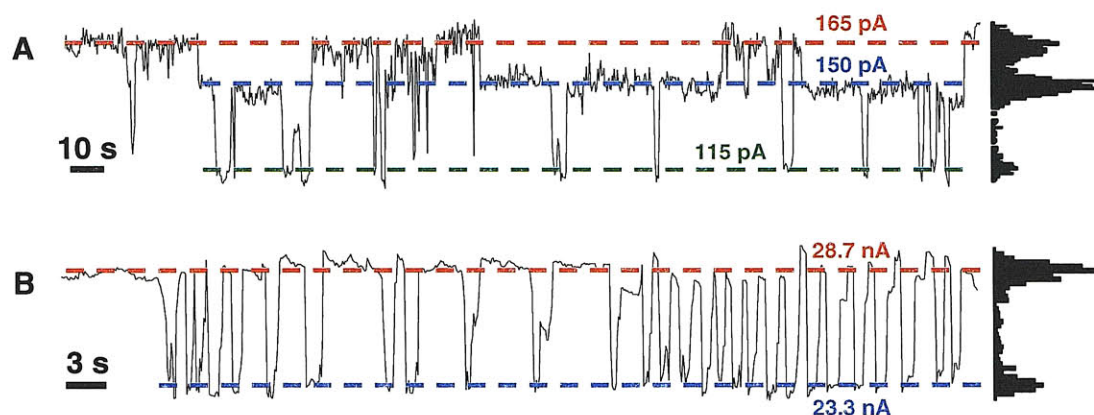


Figure 47. Ion current from the device. a) Measurement with 1M NaCl on both sides at 0.3V. 3 peaks in all-point-histogram suggest that the pore blocking is caused by at least 2 nanotubes. b) Measurement with 1M LiCl on both sides at 3V. Current transition occurs between only 2 states indicating the phenomenon is from a single tube.

Two critical questions need to be answered: 1) what carries the current, and 2) what blocks the current. Current level with and without any added salts is comparable to each other. This means only H^+ and/or OH^- are candidates for major charge carriers.

Estimated velocity of the charge carriers from the ΔG , if the carriers have to physically move through the tube, turns out to be unrealistic. In ion channels where the majority charge carriers are ions, the conductance increases with the ion concentration as observed in all the solid state nanopores^{138,202} and nanofluidic channels²⁰³. In our system, however, the trend is opposite as shown in Figure 48. The result suggests that neither Na^+ nor Cl^- is the majority charge carrier through the SWNT interior, and agrees with theoretical prediction^{199,204,205} and experimental demonstration^{167,206} of ion rejection at nanopore-mouth. Therefore, H^+ and/or OH^- are the major charge carriers. Several researchers predict much faster proton conduction along the 1D chain of water molecules inside the SWNT than in the bulk¹⁷². As previously discussed, the proton conduction can occur via “hop-and-turn” Grotthuss mechanism along the water chain¹⁷¹, and does not require physical translocation of protons. Since this mechanism does not occur for the transport of OH^- , OH^- must to be translocated through the nanotube. Velocity of a hopping proton for a SWNT with 1.5 nm diameter, estimated using water density of 0.87 g/mL¹⁶², is $\sim 2 \times 10^{-2}$ m/s. Assuming single occupancy of the OH^- in a SWNT, a current decrease of 100 pA upon pore-blocking corresponds to velocity of 3×10^5 m/s, which is unrealistic. This high charge carrying rate can only be explained when the carrier displaces one already in the tube (concerted mechanism). The ends of nanotubes, when etched in oxygen plasma, are known to have carboxylic acid groups with pK_a of about 4.5²⁰⁷. Hence, at pH ~ 5 in our experiment the entrance barrier will be higher for the OH^- . From the estimations above we have concluded that the protons are the major charge carriers in our system.

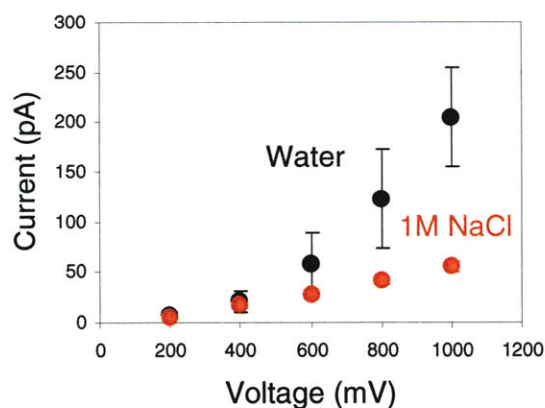


Figure 48. IV curves from one of the devices measured with and without NaCl. Conductance decreases when NaCl is added to the system suggesting little contribution of Na^+ and Cl^- to the ion current.

We find that both the nanotubes and salts are required in order to observe any blocking events. The results suggest that blockers are the ions from the added salts (cations and/or anions), and the conduction path blocked by the ions is the interior of carbon nanotubes. We repeated the experiments using a solution with large cations, 1M tetramethylammonium (TMA) chloride. Because the large TMA⁺ (crystallographic diameter 0.7 nm) will not be able to enter the nanotube, the experiment will verify contribution of Cl⁻, Ag⁺ (dissolved from Ag/AgCl electrodes) and other impurities in the solution to the pore-blocking. As shown in Figure 49, no blocking-events suggest that none above are the blockers. The result can be attributed to repulsion of anions from negatively charged pore-mouth as well as low concentration of Ag⁺ ($\sim 10^{-5}$ M based on K_{sp} of AgCl = 1.8×10^{-10}) and impurities.

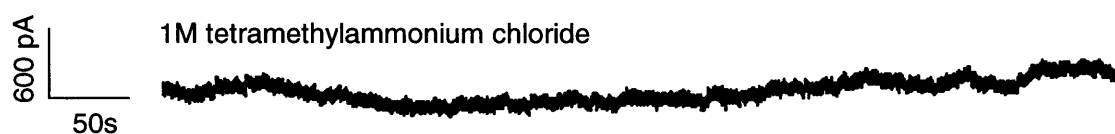


Figure 49. Ion current through SWNTs using 1M tetramethylammonium chloride on both sides of the SWNTs. No pore-blocking events are observed.

We have considered other possible scenarios of the pore-blocking. We first reject the possibility of ion clusters blocking the pores since the diameter of clusters measured by dynamic light scattering is about 500 nm, which is too large to block the tubes. Precipitation of ions²⁰⁸, which might block the pore, does not occur because of high solubility product (K_{sp}) of NaCl, KCl, and LiCl. Next, impurities in the solution are considered. As discussed earlier, impurities in water do not cause any pore-blocking. No blocking from the TMA-Cl suggests impurities in salts have little effect. No event from the water and TMA-Cl removes the possibility of nanobubbles²⁰⁹ as well. Ag⁺ and Cl⁻ dissolve out from Ag/AgCl electrodes with K_{sp} of 1.8×10^{-10} . [Ag⁺] is about 5 orders of magnitude smaller than [Na⁺] and therefore is negligible. Once an ion blocks the pore, the ion must translocate to the other side because the driving force of diffusing back to the solution is relatively weak compared to high electric field across the blocker.

The presence of threshold voltage for ion entrance matches with theoretical predictions in the literature. Ions need to shed hydration shells when entering a

nanochannel¹⁹⁹. In protein ion channels carbonyl oxygens minimize the dehydration energy barrier¹³⁷, whereas in hydrophobic nanopores such as carbon nanotubes enough energy above threshold must be supplied to overcome the barrier. For the nanotubes in our study, required free energy of permeation is 80-150 meV¹⁹⁹. The observed minimum threshold voltage of 100 mV is within this range. Fornasiero et al.¹⁶⁷ have experimentally measured % ion rejection by a nanotube membrane as a function of ion concentration and valence. Rejection of anions on average was more efficient due to negatively charged pore-mouth. Our system has ability of detecting a single ion and therefore allows accurate estimation of separation factor. Complete rejection of ions can be achieved below the threshold, and even the minimum separation factor (proton/alkali cation) is as high as $\sim 6 \times 10^7$! Our device when scaled up can find applications in desalination of sea water and water purification.

We are the first to experimentally detect transport of individual ions through a solid-state nanopore. Two key elements in our nanochannel allow this measurement: 1) diameter comparable to the size of individual ions, and 2) nanopore with the highest aspect ratio ever tested. Single walled carbon nanotube is the only material with this property. Characteristic transport time of an ion in our study is in the range of 100 ms. The time for other nanopores with aspect ratio of at most 10, when linearly scaled back, is only 2 μ s, which is shorter than the time resolution of most equipments. For this reason counting individual ions has been achieved neither in biological nor non-biological ion channels. The current trace in our system resembles that of protein ion channels, but the origin of the phenomenon differs intrinsically. KcsA K⁺ channel for instance can flow about 10⁸ ions/s in open state, and the current drops when the channel physically closes via structural change of the protein¹³⁶. Conversely, in our SWNT channels charge carriers in open state are protons whose flow is reduced upon blocking by a single ion.

Our ability to detect individual ions is assisted by extremely efficient proton conduction through SWNT. The proton conduction is reduced upon ion entrance to the nanotubes possibly due to 1) disrupted water chains, 2) reduced cross-section for proton conduction, 3) water molecules dedicated to hydrating the ion than to proton conduction. Since ions might partially block the proton conduction, we use the maximum ΔG (= 420 pS) to estimate the single-tube proton conductivity of 1.2×10^3 S/cm, about 4 orders of

magnitude higher than for the commercial Nafion membrane, and also the highest ever achieved. To our knowledge this is the first experimental report of the fast proton transport through the SWNT interior. With its chemical and thermal stability SWNT may potentially replace current proton conducting polymers such as Nafion and find applications in proton exchange membranes for direct methanol fuel cell.

3.3. Ion current oscillation due to rhythmic transport of ions

Occasionally we see highly synchronized and rhythmic transport of ions with locked frequency. Figure 50 shows rhythmic pore-blocking events and resulting current oscillations from 1M NaCl, LiCl, and KCl translocating through nanotubes. Multiple nanotubes are in the device, but oscillation between only two states ensures the single-tube events although not clear whether identical nanotubes are involved across experiments¹⁴⁵. Except for the NaCl with a baseline drift, two states are distinguished in the all-point histograms.

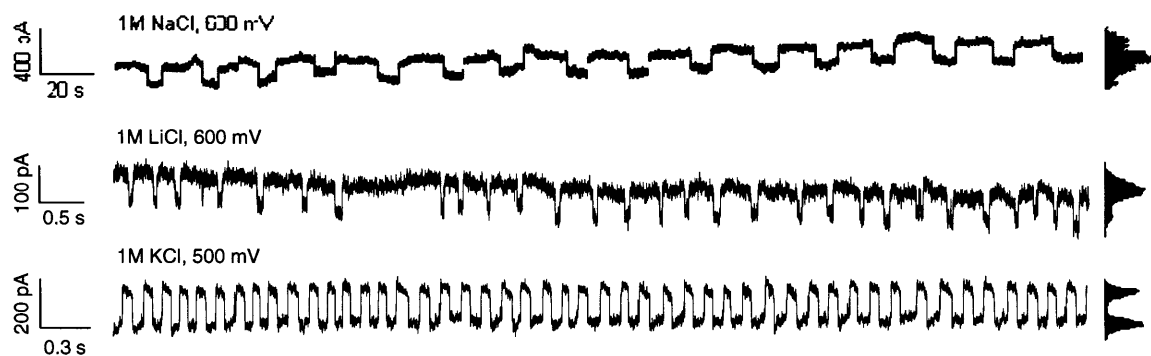


Figure 50. Ion current oscillation showing rhythmic transport of ions. Dwell time, open-channel lifetime, and thus the frequency of the pore-blocking vary between ions.

Average frequency of the oscillation can be obtained from fast Fourier transform (FFT) in Figure 55a: 0.046 Hz for NaCl, 2.7 Hz for LiCl, and 8.1 Hz for NaCl. The oscillation is fragile, but can be also stable for as long as several minutes counting thousands of individual cations as shown in the following figures.



Figure 51. Current oscillation when 1M NaCl placed at both ends of open nanotubes. Extended from the oscillation shown in Figure 50.

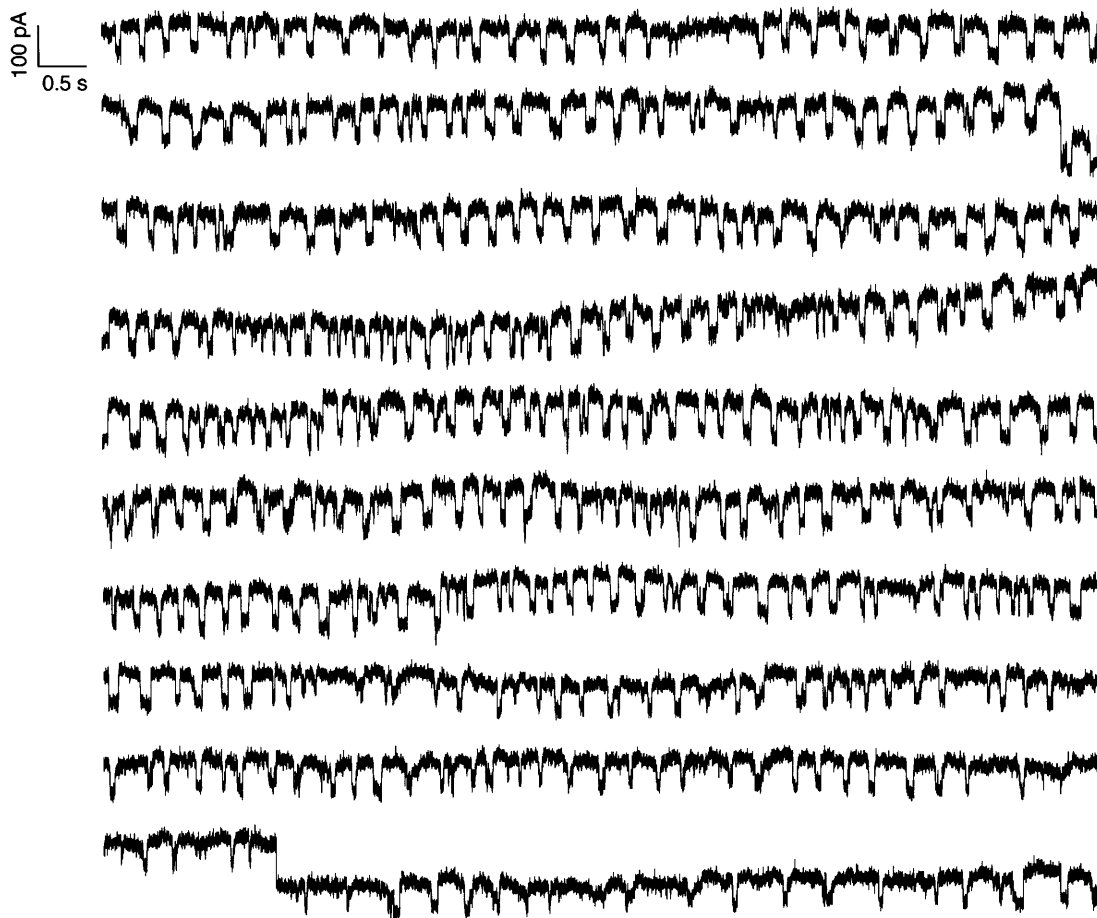


Figure 52. Current oscillation when 1M LiCl placed at both ends of open nanotubes. Extended from the oscillation shown in Figure 50.



Figure 53. Current oscillation when 1M KCl placed at both ends of open nanotubes. Extended from the oscillation shown in Figure 50.

We used a custom Matlab code to extract the current change (ΔI), dwell time of blockers (τ_{dwell}), and open-channel lifetime from each blocking event. Considering the characteristic time of each event (~ 100 ms) and the data collection frequency (250 kHz), we trimmed the data by taking every 100-500 data point from raw data. Example trimmed data from 1M NaCl at 600 mV are shown in Figure 54a. Moving window average of the slope was calculated with varied window size (Figure 54b). The slope can be transformed into three states: 0 (stable ion current), -1 (current decrease due to pore-blocking), and +1 (current restoration due to pore-opening) as in Figure 54c. For each pore-blocking event, which can be described as a sequence of (-1)-(0)-(+1), dwell time of i^{th} event, $\tau_{\text{dwell}}(i)$, corresponds to $t_{+1}(i) - t_{-1}(i)$. t_{+1} and t_{-1} represent time for pore-opening

and closing, respectively. The open-channel lifetime for i^{th} event is $t_1(i+1) - t_1(i) - \tau_{\text{dwell}}(i)$.

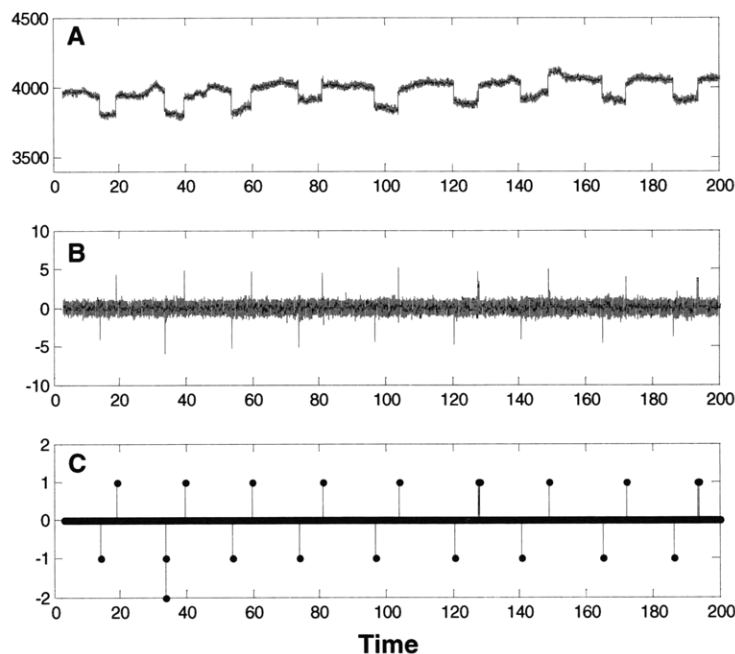


Figure 54. Data processing in Matlab. a) Trimmed ion current data from 1M NaCl 600 mV. Every 500 point is collected from the raw data to reduce the data size. b) Slopes taken from the current trace above with window size of 10 data points. c) Trace in b) is transformed into 3 states: 0 (constant current), -1 (pore-blocking), +1 (pore-opening).

Using the program described above, we have generated histograms of ΔG and ion mobility from 42, 666, and 2469 pore-blocking events from NaCl, LiCl, and KCl, respectively (Figure 55b). Distributions of the ΔG are Gaussian, but distribution of the ion mobility (velocity per electric field) is skewed. Na^+ has the smallest mobility values ($\sim 5 \times 10^{-8} \text{ m}^2/\text{Vs}$) of all tested. Li^+ and K^+ have mobility of $\sim 5 \times 10^{-6} \text{ m}^2/\text{Vs}$ on average and of as high as $\sim 2 \times 10^{-5} \text{ m}^2/\text{Vs}$. We are the first to experimentally measure mobility of individual ions through nanotubes. The values are 3 orders of magnitude higher than the cation mobility in bulk water and the theoretical mobility through a 3 nm diameter SWNT¹⁸⁶, both of which are around $10^{-8} \text{ m}^2/\text{Vs}$. This high ion mobility is associated with atomically smooth surface of the SWNT and the resulting velocity slip at the wall.

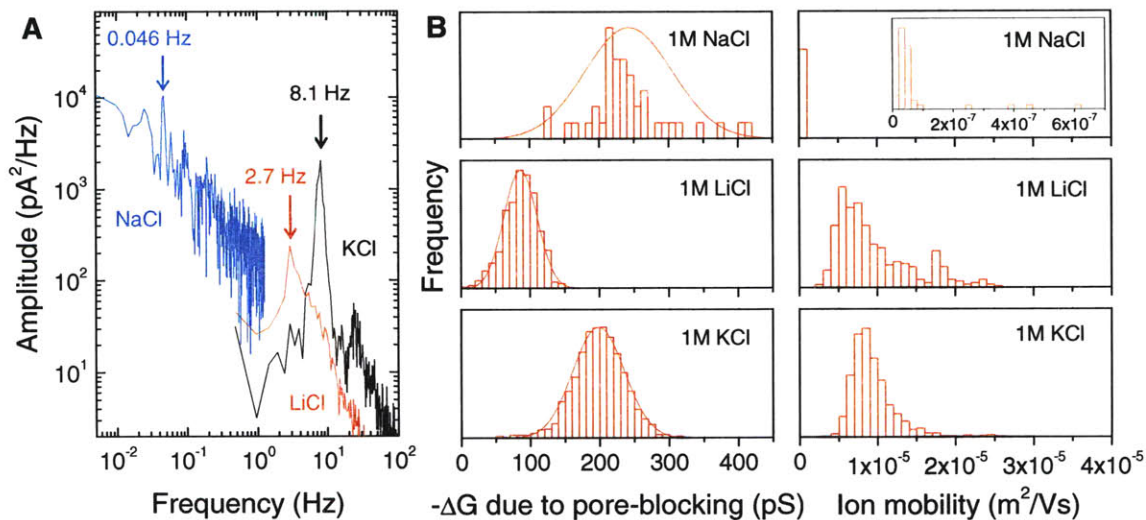


Figure 55. Analysis of current oscillations. a) Fast fourier transform (FFT) of the oscillations in Figure 50. b) Histograms of conductance decrease and ion mobility for each ion.

ΔG versus mobility is plotted for each blocking event (Figure 56a). For the Li^+ (red), which has a wide mobility distribution, it is evident that ΔG and mobility are inversely proportional to each other. Similar trend is also observed in the case of KCl. We believe the ΔG to mobility ratio increases with ion/nanotube diameter ratio (i.e. reduced cross-section area for proton conduction) as theoretically predicted in Liu et al.²¹⁰ and experimentally demonstrated in DNA passing through solid-state nanopores¹⁴². Smallest ΔG values along with large variation in mobility for Li^+ may be attributed to the small diameter of Li^+ (0.12 nm). Mobility of Na^+ , smaller by 2-3 orders of magnitude than other cations, suggests the ion fits tightly inside the nanotube (Figure 56b). However, further study using a single-tube device is required for clarification.

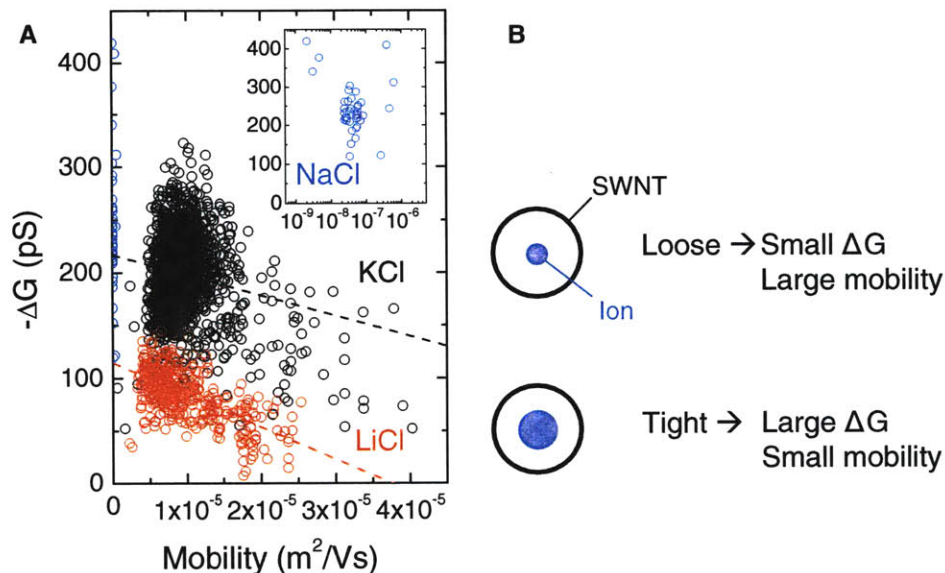


Figure 56. Conductance decrease due to pore-blocking versus ion mobility. a) ΔG and mobility are inversely proportional to each other. b) Small (large) ions fit loosely (tightly) into the nanotube and lead to small (large) ΔG and high (low) mobility.

We have considered other possible mechanisms of the current oscillation. First, the oscillation is not caused by rhythmic nanoprecipitation at pore-mouth²⁰⁸ because the salts in our study have large K_{sp} and thus do not form precipitates. Fast transition at both opening and closing is another evidence of rhythmic ionic translocation rather than precipitation. Furthermore, the inverse relationship between ΔG and mobility (Figure 56a) can be observed only when the ions translocate. Ion clusters, if they ever form, will have non-uniform size distribution and cannot explain the uniform dwell time distribution in our study. Liu et al.²¹¹ proposed that in a nanochannel with diameter of 0.74 nm dehydrated ions are stabilized by forming evenly spaced cation-anion pairs. Authors predict higher frequency for smaller ions such as LiCl. However, nanotubes in our system ($d = 1.2 \text{ nm} - 2.3 \text{ nm}$) are large enough to allow a few hydration shells, and the oscillation frequency is higher for larger ions, KCl, than for the smaller LiCl.

Even with the same sample and ions properties of the current oscillation can vary. In previous tests Na^+ had a long dwell time of $\sim 10s$ at 600 mV. Testing the identical sample at 1 V causes oscillations with dwell time of 100 ms or shorter. We believe it is due to the presence of multiple nanotubes in the sample (~ 45 nanotubes). As the voltage is varied, nanotubes with different diameter become resonant.

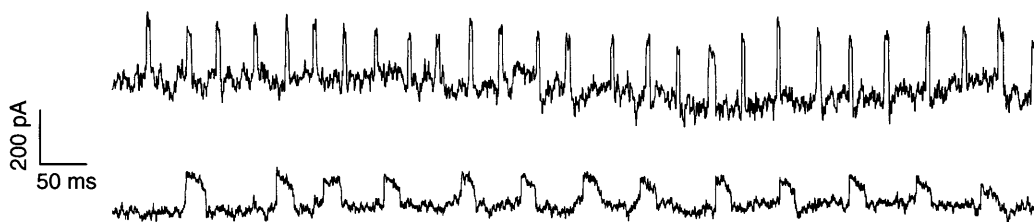


Figure 57. Current oscillation from 1M NaCl at 1V. Properties of the oscillation in the same sample vary due to presence of multiple nanotubes with different diameters.

The current oscillation in SWNT ion channels is a generic phenomenon, which is observed in multiple samples. Current oscillations observed from another sample are shown below. Again, varying frequencies and dwell times are due to multiple nanotubes in the system.

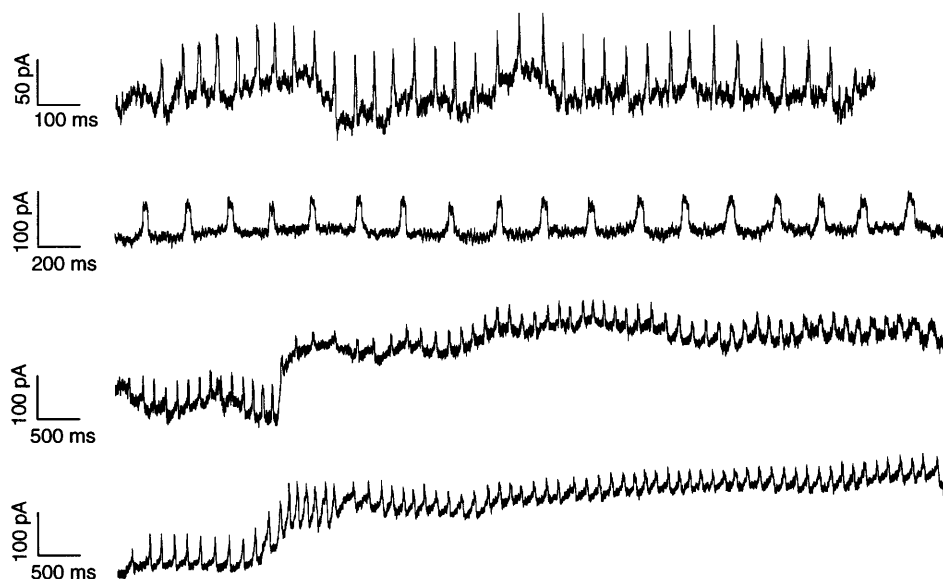


Figure 58. Current oscillation another sample tested using 1M NaCl at 200 mV.

Rhythmic process and synchronized behavior are ubiquitous in nature¹⁹⁵. If we limit our discussion to cell membranes, blocking or closing events usually follow a random Poisson process with exponential probability density. Only when the opening and closing are highly cooperative do they show synchronous oscillations. Spontaneous rhythmic oscillations are observed in calcium-regulated cation channel in skeletal muscle²¹², pores of ATP synthase subunit *c*²¹³, and opening and closing of vesicles during exo/endocytosis²¹⁴. Synthetic nanopore oscillators therefore can be applied to timing circuits for pacemaking, or signal processing. Powell et al.²⁰⁸ reported the ion current

oscillation in a solid-state nanopore where transient nano-precipitation and dissolution of divalent ions respectively blocked and opened the pore. Note that for all of the above report the nanopore itself opens and closes, and we demonstrate the first synthetic nanopore where rhythmic *translocation* of individual ions is detected.

3.4. Understanding the current oscillation: stochastic resonance

Stochastic resonance as a detection mechanism occurs when a sub-threshold signal is amplified instead of obscured by environmental noise, allowing for discrimination despite stochastic interference. There are many examples in biological systems including crayfish detecting pressure waves generated by predators¹⁵¹, paddlefish finding planktons¹⁵³, human visual perception¹⁵⁶, etc. The distinguishing attribute of these systems is that the signal to noise of the sensory output increases to an optimum with increasing noise, the signature of stochastic resonance. Bezrukov and Vodyanoy¹⁵⁴ reported that a collection of alamethicin ion channels constituted the simplest experimental system capable of stochastic signal enhancement, but it remains an open experimental question whether a single, static ion channel alone can demonstrate this important function. A nanopore formed from the interior of a single walled carbon nanotube has captivated the interest of many theorists, who have predicted enhanced water permeation, large proton fluxes, ice like water phases, and high ion rejection rates. However, experimentally it has proven difficult to observe single molecule transport from a single isolated nanotube, despite success with macroscopic ensembles forming various membranes for gas and liquid separations. In previous sub-chapters, single molecule transport through the interior of a single carbon nanotube is studied for the first time, revealing the highest proton conductivity experimentally measured to date. We observe that this nanopore system can show oscillations in the electro-osmotic current, resulting in rhythmic, mode-locked frequencies of ion transport. In this part of my thesis we demonstrate that the oscillations arise from stochastic resonance. The results prove that simple, single ion transport from an isolated nanopore is all that is needed to produce a stochastic resonant mechanism, and they also open the door to new types of chemical nano-reactors, nanofluidic conduits and single molecule sensors.

As shown in Figure 37, simply adding more open states cannot describe the oscillation observed in our system. When the system oscillates, both the dwell time (τ_{dwell}) and open-channel lifetime have narrow and symmetric distribution with maxima at non-zero values. For the nanopores with high aspect ratio, sharp distribution of the dwell time can be easily obtained due to minimum time required for translocation, $\tau_{\text{dwell}} \sim L/(E\mu)$, where L , E , μ denote pore length, electric field, blocker mobility, respectively. However, narrow distribution of the open-channel life can be obtained only when the rate of an incoming ion is highly synchronized with the presence of an ion already inside the nanopore.

These oscillations are caused by a coupling between the stochastic pore blocking and a proton diffusion limitation that develops at the pore mouth (Figure 59). As stated before, the proton conductivity through the nanotube ($\sim 10^3$ S/cm) is substantially higher than that of bulk solution (~ 0.03 S/cm²¹⁵). Therefore, an unobstructed proton current in the nanotube will necessarily deplete the proton concentration at the pore mouth. Coupling occurs because the depletion increases the relative blocking ion concentration, increasing its probability of partitioning into the nanotube, an extremely rare event otherwise. Once the nanotube is blocked, the proton concentration at the pore mouth increases rapidly while the blocking ion traverses the nanotube. When it emerges from the other side, the proton current is restored, and a subsequent blocking event suppressed by the initially high concentration of protons relative to blocking cations. Reformation of the diffusion limitation at the proton flow is restored then allows this cycle to repeat indefinitely. We constructed a stochastic simulation (Fig 59) with 6 equations and rate constants.

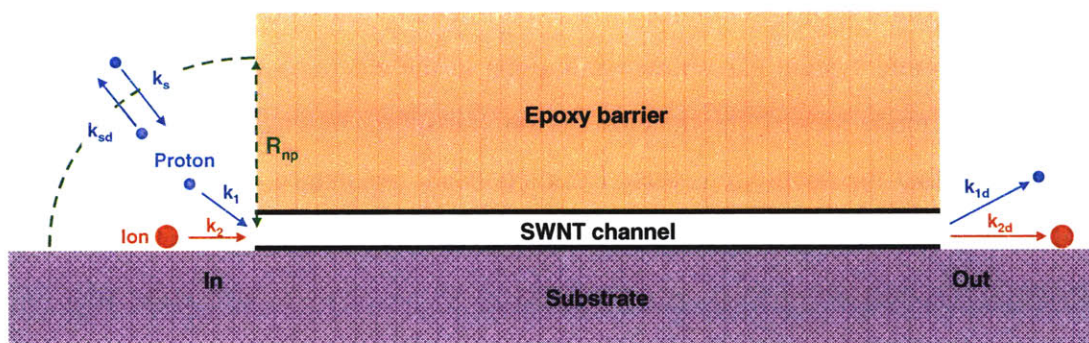
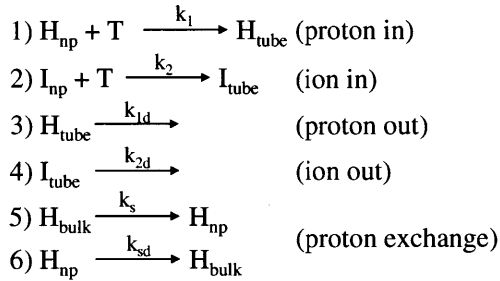


Figure 59. Proposed mechanism of the current oscillation. R_{np} is a near-pore proton depletion region. We consider 6 reactions: 1) proton in with rate constant k_1 , 2) ion in with rate constant k_2 , 3) proton out with rate constant k_{1d} , 4) ion out with rate constant k_{2d} , 5) and 6) proton exchange between R_{np} and bulk solution with rate constant k_s .

- 1) Proton in: Protons at near-pore region of radius R_{np} (H_{np}) enter the nanotube (T) with rate constant k_1 and become protons inside the tube (H_{tube}).
- 2) Ion in: Ions at the near-pore region (I_{np}) enters the nanotube with rate constant k_2 and become ions inside the tube (I_{tube}).
- 3) Proton out: Protons inside the nanotube (H_{tube}) translocate to the other side with rate constant k_{1d} .
- 4) Ion out: Ions inside the nanotube (I_{tube}) translocate to the other side with rate constant k_{2d} .
- 5) Proton exchange in: Protons in bulk (H_{bulk}) move into the near-pore region with rate constant k_s .
- 6) Proton exchange out: Protons in the near-pore region leave to bulk with rate constant k_{sd} .



Diffusion parameters (k_s and k_{sd}) are estimated from bulk proton diffusivities and the pore mouth affinity. The blocking rate constant (k_2) is small compared to the proton value (k_1). This system reconstructs the oscillation frequencies observed experimentally for certain values of the proton partitioning rate constant, and also the Gaussian distribution in arrival times observed during the oscillations events. The signature of stochastic resonance is one where the signal to noise ratio of the system increases to an optimal value upon increasing noise or random fluctuations. This is demonstrated in Figure 60 by tuning the rate of proton partitioning (k_1) into the nanotube, which controls

the inherent noise in the system. A value of k_1 that is too large or too small to create the resonance condition results in a blocking frequency that is Poisson-like and erratic. As k_1 approaches an inherent resonance condition, the distribution of open-channel lifetimes becomes Gaussian and narrow, and the blocking events occur with a locked frequency. This mathematical system can reproduce the frequency values of the oscillations (Fig 61a) by examining the FFT of the blocking cation occupancy.

We have made several assumptions.

- Assumption 1: $k_1 \gg k_2$ (Since partitioning of ions is a rare event due to the dehydration energy barrier, it is reasonable to assume that the rate constant for the proton-in (reaction 1) is much larger than the value for the ion-in (reaction 2).)
- Assumption 2: Due to fast proton conduction there is a proton depletion region of radius R_{np} near the pore-mouth.
- Assumption 3: While the SWNT is occupied by an ion ($I_{tube} = 1$), there is an accumulation of protons within R_{np} (increase the H_{np} by 1).
- Assumption 4: Since ions require minimum time for translocation through SWNTs due to high aspect ratio, there is a time delay of dwell time, τ_{dwell} , in the reaction 4.

According to Gillespie²¹⁶ time interval between each reaction is determined by

$$\tau = 1/a_{total} \times \log(1/r)$$

where $a_{total} = k_1 H_{np} T + k_2 I_{np} T + k_{1d} H_{tube} + k_{2d} I_{tube} + k_s H_{bulk} + k_{sd} H_{np}$, and r is a random number between 0 and 1. Which reaction to occur among the 6 reactions (= probability of each reaction) is determined by (rate of each reaction)/ a_{total} . The time delay, τ_{dwell} , was adopted from the dwell time distribution of the current oscillation shown in Figure 50 (Gaussian distribution with average 57 ms and standard deviation 14 ms). We ran stochastic simulations using the Gillespie algorithm with time delay²¹⁷ at varied values of k_1 , the parameter that determines noise level in our system. The values used to obtain the Figure 60 are $R_{np} = 200$ nm, pH (bulk) = 5, ion concentration = 1 M, proton diffusivity (bulk) = 10^{-10} m²/s, $k_2 = 10^{-4}$ s⁻¹, $k_{1d} = 5 \times 10^5$ s⁻¹, $k_{2d} = 500$ s⁻¹, $k_s = 7500$ s⁻¹, $k_{sd} = k_s/400$.

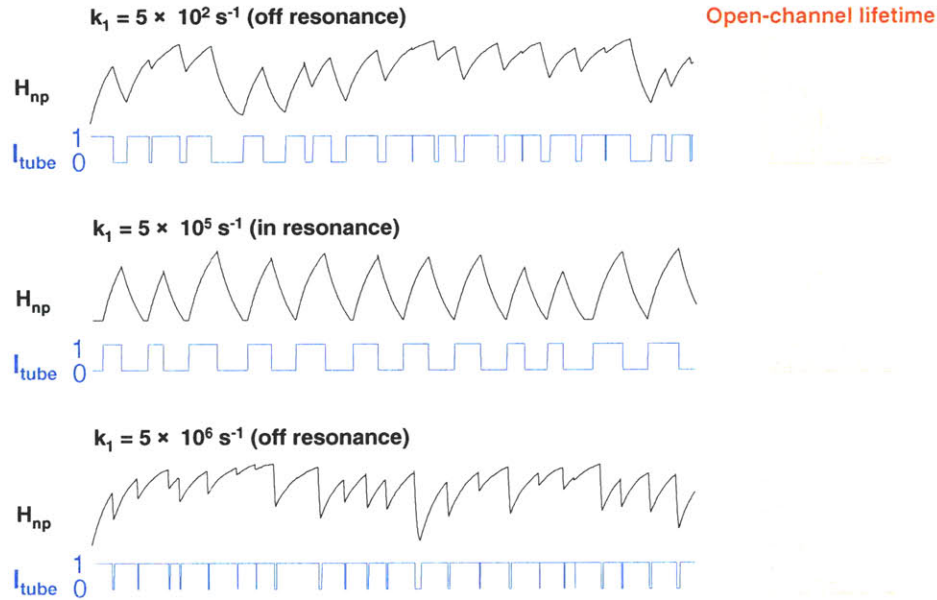


Figure 60. Protons at pore-mouth (H_{np}) and ion occupancy (I_{tube}) with varied rate constants of proton-in (k_1). When k_1 is either too small or too large (top and bottom) the H_{np} and I_{tube} do not oscillate as indicated by the exponential distribution of open-channel lifetime. At optimal k_1 (middle), when the system is in resonance, H_{np} and I_{np} oscillates with locked frequency, and distribution of the open-channel lifetime becomes Gaussian.

A summary of the stochastic resonance appears in Fig 61 where the signal to noise of the FFT fundamental is plotted versus k_1 . There is an optimal proton partitioning rate constant (k_1) that maximizes the coherent signal, and allows for oscillatory output.

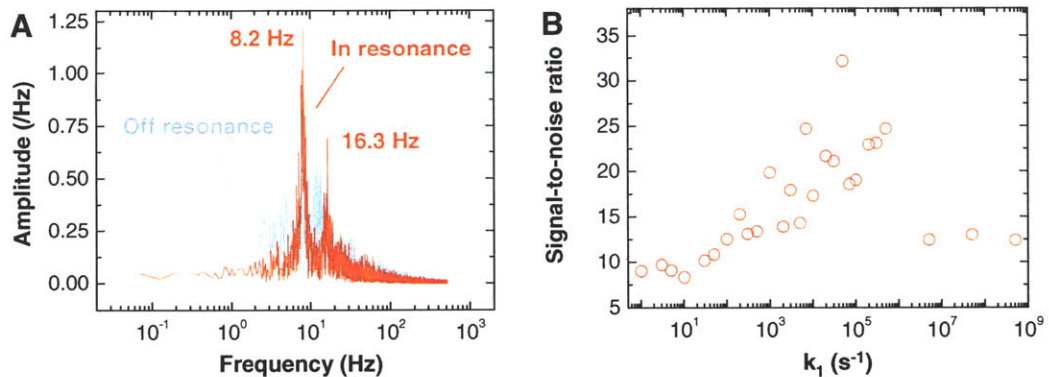


Figure 61. Signature of the stochastic resonance. a) FFT when the system is in resonance (red) versus off resonance (gray). A sharp peak is observed when the system is resonant. b) Signal to noise ratio (SNR) versus k_1 showing optimal value of k_1 at which the SNR is maximized.

We were able to generate histograms of dwell time and open-channel lifetime by collecting enough counts from the simulation. As shown in Figure 62, our model can almost accurately simulate the experimental results. The regular fluctuation of proton concentration sets up a feedback loop thereby causing the ion current oscillation. It should be noted that the major driving force of ion entrance is the proton depletion at the pore-mouth. If the depletion region is removed somehow (e.g. stirring the reservoir or testing at lower pH), ions won't be able to enter again due to $k_1 \gg k_2$.

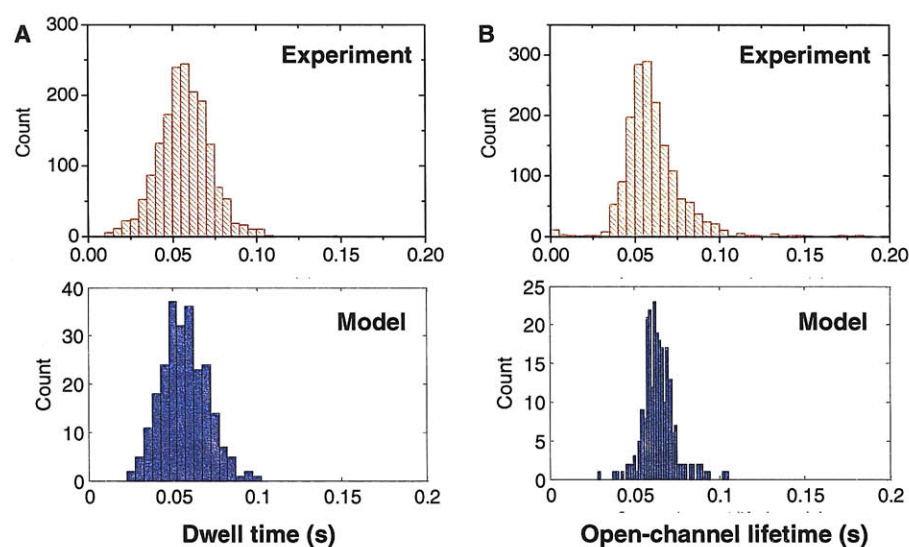


Figure 62. Comparison between experiments and our model. a) Dwell time histograms. b) Open-channel lifetime histograms. Our model can simulate the experimental results.

Figure 63 shows number of pore-blocking events at different voltages. For KCl, LiCl, and NaCl optimal voltages at which the current oscillation is very stable are 500 mV, 600 mV, and 600 mV, respectively. The presence of an optimal voltage is different from other nanopore systems in the literature where more blocking events are observed at higher voltage. We believe this is a signature of the stochastic resonance discussed in section 1.2. In our system, rather than varying the noise level to overcome a threshold, the threshold or the bias is varied at a fixed noise level. This is the first time demonstration of the stochastic resonance in synthetic nanopores.

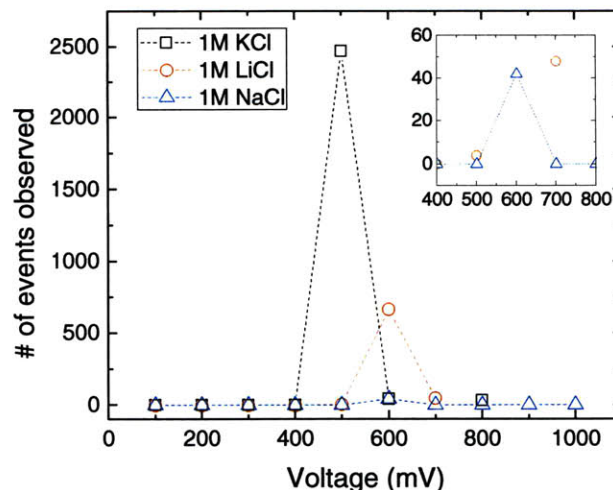


Figure 63. Number of pore-blocking events versus testing voltage. For each ion there is an optimal voltage to observe stable current oscillation. This is a signature of stochastic resonance in SWNT ion channels.

The stochastic resonance condition dramatically increases the single molecule processing rate of the nanotube ($\sim 480/\text{min}$ in resonance versus $\sim 5/\text{min}$ off resonance). This has implications for other nanopore systems, including DNA translocation and sequencing, and Coulter detectors. The ice-like phase that forms in the nanotube interior imparts the largest proton conductivity measured to date, opening possibilities for new types of proton conducting membranes for fuel cells and catalysis. This work is the first to demonstrate single ion detection in aqueous solution, and may allow for ultrasensitive detection technologies for environmental or biological monitoring of ion types differentiated by their dwell times. The experimental system here also provides an ionic resonator or waveform generator to the emerging family of devices that use ions for information processing, such as ionic transistors²¹⁸, and rectifier circuits²¹⁹. However, the ability to manipulate single small molecules (albeit only ions demonstrated in this work) may allow for the construction of chemical reactor devices that process single molecules at a time. The stochastic resonance condition necessarily ensures that only one molecule occupies the nanotube at a time, which may be useful for manipulation and feedback control schemes, as well as coupling to external measurement devices for cataloging the single molecule efflux.

Conclusion

Single walled carbon nanotubes (SWNT) are unique materials with high surface to volume ratio and all atoms residing on the surface. Due to their tubular shape both exterior and interior of SWNT are available for interaction with other molecules. The one-dimensional electronic structure of SWNT is readily disrupted even by single adsorption events. Hence, one of the promising applications of these materials has been sorption-based sensors utilizing the exterior of the SWNT. The interior of SWNT can potentially be used as a frictionless molecular conduit due to graphitic surface where molecular corrugation is minimized by high density of atoms. However, only few experimental results on the interior exist due to difficulties in designing a reliable platform.

First part of my thesis focuses on understanding and controlling the molecular binding on the exterior of carbon nanotubes for gas sensing applications. Due to the 1-D electronic nature, sensitivity of the SWNT gas sensor has not been of a big concern in this area. Our major contribution is in resolving two major problems of the SWNT gas sensors: the reversibility and the selectivity. Most SWNT sensors exhibited irreversible sensor responses meaning that flushing the environment with an analyte-free gas did not completely remove the analytes from the sensor. The irreversibility is a major cause of sensor failure and limits the long term operation of the sensor. Subsequent data from the same systems occasionally demonstrate reversible sensor responses for the same analytes, but this contradictory behavior has not been studied or even discussed in previous reports. We show for the first time the irreversible-to-reversible transition via simple surface amine chemistry. We have screened various amine functionalities and found the mechanism of reduced analyte binding energy via surface chemistry. We were able to enhance the sensitivity by several orders of magnitude, without losing the reversibility, by creating more adsorption sites with polymeric amines. The ability to fabricate highly sensitive and reversible sensors enables a new type of application: the integration of SWNT sensor with micro-fabricated gas chromatographic (GC) column, which has not been possible with irreversible sensors. The platform benefits from the separation capability of the GC, an analytical standard for the detection of diverse classes of organic molecules. Our approach eliminates the need to engineer selective binding sites for small

molecule analytes for SWNT, a difficult problem only solved for specialized cases, and therefore can potentially solve the selectivity problem.

For the second part of my thesis the SWNT interior is explored. Ever since the discovery of a single walled carbon nanotube (SWNT) in 1993, every carbon nanotube researcher has speculated on whether small molecules can ever be transported through the interior of the SWNT. Despite large interest by the nanotube and bio-membrane communities actual reports on the interior of *individual* SWNT have been limited only to theories and simulations, no doubt due to challenges in reliably fabricating and testing an experimental platform. All of the theoretical works predict the velocity of water and ions several orders of magnitude higher than the value estimated by continuum hydrodynamics. SWNT therefore holds a great promise for future applications in nanofluidic fast molecular transporters, and understanding the transport at the level of individual nanotubes should be a starting point. Here we demonstrate the first experimental evidence of transport of individual ions through the interior of a single walled carbon nanotube. SWNT in our system has aspect ratio of $\sim 10^5$, about 4 orders of magnitude higher than previously tested nanopores. The high aspect ratio allows studying molecular transport at a completely different regime due to increased characteristic time. We verified that upon external electric field above threshold hydrated individual ions can be transported through the SWNT interior with several characteristic parameters. The results suggest that the SWNT may find applications in counting and sizing small ions such as Na^+ , Li^+ , and K^+ in solution. Large current decrease upon pore-blocking is aided by highly efficient proton conduction through the SWNT interior. The estimated proton conductivity in our system was as high as ~ 1000 S/cm, several orders of higher than existing commercial proton conducting membranes. The results above suggest several promising applications such as water purification/desalination, proton exchange membrane for direct methanol fuel cells, etc. We also find that when the system is in “resonance”, stable oscillations of the ion current are observed. Frequency of the oscillations varies between systems. Our stochastic simulation suggests that the oscillation originates from synchronization between ions inside the tube and protons at the pore-mouth. The oscillation is very fragile, but stable for several minutes only at optimal electric field. This is a signature of the stochastic resonance, which has never

been observed in synthetic ion channels. We believe that our findings will open up a whole new active research area and revitalize the field. Potential applications are, to name just a few, nanofluidic devices with molecular precision, molecular storage, size-exclusive molecular transport, confined chemical reaction within the nanotube, ion rejection and desalination devices, controlling the transport by attaching end-functional groups, and so on.

References

- (1) Iijima, S.; Ichihashi, T. *Nature* **1993**, *364*, 737-737.
- (2) Ajayan, P. M.; Iijima, S. *Nature* **1993**, *361*, 333-334.
- (3) Mintmire, J. W.; Dunlap, B. I.; White, C. T. *Physical Review Letters* **1992**, *68*, 631-634.
- (4) Hamada, N.; Sawada, S.; Oshiyama, A. *Physical Review Letters* **1992**, *68*, 1579-1581.
- (5) Dresselhaus, M. S.; Avouris, P. *Carbon Nanotubes* **2001**, *80*, 1-9.
- (6) Wildoer, J. W. G.; Venema, L. C.; Rinzler, A. G.; Smalley, R. E.; Dekker, C. *Nature* **1998**, *391*, 59-62.
- (7) Odom, T. W.; Huang, J. L.; Kim, P.; Lieber, C. M. *Nature* **1998**, *391*, 62-64.
- (8) Martel, R.; Schmidt, T.; Shea, H. R.; Hertel, T.; Avouris, P. *Applied Physics Letters* **1998**, *73*, 2447-2449.
- (9) Javey, A.; Tu, R.; Farmer, D. B.; Guo, J.; Gordon, R. G.; Dai, H. J. *Nano Letters* **2005**, *5*, 345-348.
- (10) Moore, G. E. *Proceedings of the Ieee* **1998**, *86*, 82-85.
- (11) Ago, H.; Petritsch, K.; Shaffer, M. S. P.; Windle, A. H.; Friend, R. H. *Advanced Materials* **1999**, *11*, 1281.
- (12) Rowell, M. W.; Topinka, M. A.; McGehee, M. D.; Prall, H. J.; Dennler, G.; Sariciftci, N. S.; Hu, L. B.; Gruner, G. *Applied Physics Letters* **2006**, *88*, 233506.
- (13) Gabor, N. M.; Zhong, Z. H.; Bosnick, K.; Park, J.; McEuen, P. L. *Science* **2009**, *325*, 1367-1371.
- (14) Rao, A. M.; Richter, E.; Bandow, S.; Chase, B.; Eklund, P. C.; Williams, K. A.; Fang, S.; Subbaswamy, K. R.; Menon, M.; Thess, A.; Smalley, R. E.; Dresselhaus, G.; Dresselhaus, M. S. *Science* **1997**, *275*, 187-191.
- (15) O'Connell, M. J.; Bachilo, S. M.; Huffman, C. B.; Moore, V. C.; Strano, M. S.; Haroz, E. H.; Rialon, K. L.; Boul, P. J.; Noon, W. H.; Kittrell, C.; Ma, J. P.; Hauge, R. H.; Weisman, R. B.; Smalley, R. E. *Science* **2002**, *297*, 593-596.
- (16) Usrey, M. L.; Lippmann, E. S.; Strano, M. S. *Journal of the American Chemical Society* **2005**, *127*, 16129-16135.
- (17) Yano, T. A.; Inouye, Y.; Kawata, S. *Nano Letters* **2006**, *6*, 1269-1273.
- (18) Heller, D. A.; Baik, S.; Eurell, T. E.; Strano, M. S. *Advanced Materials* **2005**, *17*, 2793.
- (19) Kim, J. H.; Heller, D. A.; Jin, H.; Barone, P. W.; Song, C.; Zhang, J.; Trudel, L. J.; Wogan, G. N.; Tannenbaum, S. R.; Strano, M. S. *Nature Chemistry* **2009**, *1*, 473-481.
- (20) Barone, P. W.; Baik, S.; Heller, D. A.; Strano, M. S. *Nature Materials* **2005**, *4*, 86-92.
- (21) Dresselhaus, M. S.; Dresselhaus, G.; Avouris, P. *Carbon nanotubes : synthesis, structure, properties, and applications*; Springer: Berlin ; New York, 2001.
- (22) Moore, V. C.; Strano, M. S.; Haroz, E. H.; Hauge, R. H.; Smalley, R. E.; Schmidt, J.; Talmon, Y. *Nano Letters* **2003**, *3*, 1379-1382.
- (23) Nish, A.; Hwang, J. Y.; Doig, J.; Nicholas, R. J. *Nature Nanotechnology* **2007**, *2*, 640-646.

- (24) Zheng, M.; Jagota, A.; Strano, M. S.; Santos, A. P.; Barone, P.; Chou, S. G.; Diner, B. A.; Dresselhaus, M. S.; McLean, R. S.; Onoa, G. B.; Samsonidze, G. G.; Semke, E. D.; Usrey, M.; Walls, D. J. *Science* **2003**, *302*, 1545-1548.
- (25) Bachilo, S. M.; Strano, M. S.; Kittrell, C.; Hauge, R. H.; Smalley, R. E.; Weisman, R. B. *Science* **2002**, *298*, 2361-2366.
- (26) Heller, D. A.; Jeng, E. S.; Yeung, T. K.; Martinez, B. M.; Moll, A. E.; Gastala, J. B.; Strano, M. S. *Science* **2006**, *311*, 508-511.
- (27) Liu, J.; Casavant, M. J.; Cox, M.; Walters, D. A.; Boul, P.; Lu, W.; Rimberg, A. J.; Smith, K. A.; Colbert, D. T.; Smalley, R. E. *Chemical Physics Letters* **1999**, *303*, 125-129.
- (28) Meitl, M. A.; Zhou, Y. X.; Gaur, A.; Jeon, S.; Usrey, M. L.; Strano, M. S.; Rogers, J. A. *Nano Letters* **2004**, *4*, 1643-1647.
- (29) Rao, S. G.; Huang, L.; Setyawan, W.; Hong, S. H. *Nature* **2003**, *425*, 36-37.
- (30) Xin, H. J.; Woolley, A. T. *Nano Letters* **2004**, *4*, 1481-1484.
- (31) Hedberg, J.; Dong, L. F.; Jiao, J. *Applied Physics Letters* **2005**, *86*, 143111.
- (32) Yu, G. H.; Cao, A. Y.; Lieber, C. M. *Nature Nanotechnology* **2007**, *2*, 372-377.
- (33) Krupke, R.; Hennrich, F.; von Lohneysen, H.; Kappes, M. M. *Science* **2003**, *301*, 344-347.
- (34) Jin, Z.; Chu, H. B.; Wang, J. Y.; Hong, J. X.; Tan, W. C.; Li, Y. *Nano Letters* **2007**, *7*, 2073-2079.
- (35) Gascoyne, P. R. C.; Vykoukal, J. *Electrophoresis* **2002**, *23*, 1973-1983.
- (36) Zhang, Z. B.; Liu, X. J.; Campbell, E. E. B.; Zhang, S. L. *Journal of Applied Physics* **2005**, *98*, 056103.
- (37) Dong, L. F.; Chirayos, V.; Bush, J.; Jiao, J.; Dubin, V. M.; Chebian, R. V.; Ono, Y.; Conley, J. F.; Ulrich, B. D. *Journal of Physical Chemistry B* **2005**, *109*, 13148-13153.
- (38) Suehiro, J.; Zhou, G. B.; Hara, M. *Journal of Physics D-Applied Physics* **2003**, *36*, L109-L114.
- (39) Suehiro, J.; Zhou, G. B.; Imakiire, H.; Ding, W. D.; Hara, M. *Sensors and Actuators B-Chemical* **2005**, *108*, 398-403.
- (40) Shin, D. H.; Kim, J. E.; Shim, H. C.; Song, J. W.; Yoon, J. H.; Kim, J.; Jeong, S.; Kang, J.; Baik, S.; Han, C. S. *Nano Letters* **2008**, *8*, 4380-4385.
- (41) Wu, Z. C.; Chen, Z. H.; Du, X.; Logan, J. M.; Sippel, J.; Nikolou, M.; Kamaras, K.; Reynolds, J. R.; Tanner, D. B.; Hebard, A. F.; Rinzler, A. G. *Science* **2004**, *305*, 1273-1276.
- (42) Chiang, I. W.; Brinson, B. E.; Huang, A. Y.; Willis, P. A.; Bronikowski, M. J.; Margrave, J. L.; Smalley, R. E.; Hauge, R. H. *Journal of Physical Chemistry B* **2001**, *105*, 8297-8301.
- (43) Kong, J.; Cassell, A. M.; Dai, H. J. *Chemical Physics Letters* **1998**, *292*, 567-574.
- (44) Dresselhaus, M. S.; Dresselhaus, G.; Eklund, P. C. *Science of fullerenes and carbon nanotubes*; Academic Press: San Diego, 1996.

- (45) Holt, J. K.; Park, H. G.; Wang, Y. M.; Stadermann, M.; Artyukhin, A. B.; Grigoropoulos, C. P.; Noy, A.; Bakajin, O. *Science* **2006**, *312*, 1034-1037.
- (46) Srivastava, N.; Li, H.; Kreupl, F.; Banerjee, K. *Ieee Transactions on Nanotechnology* **2009**, *8*, 542-559.
- (47) Heller, D. A.; Mayrhofer, R. M.; Baik, S.; Grinkova, Y. V.; Usrey, M. L.; Strano, M. S. *Journal of the American Chemical Society* **2004**, *126*, 14567-14573.
- (48) Wang, X. S.; Li, Q. Q.; Xie, J.; Jin, Z.; Wang, J. Y.; Li, Y.; Jiang, K. L.; Fan, S. S. *Nano Letters* **2009**, *9*, 3137-3141.
- (49) Hong, B. H.; Lee, J. Y.; Beetz, T.; Zhu, Y. M.; Kim, P.; Kim, K. S. *Journal of the American Chemical Society* **2005**, *127*, 15336-15337.
- (50) Huang, S. M.; Woodson, M.; Smalley, R.; Liu, J. *Nano Letters* **2004**, *4*, 1025-1028.
- (51) Qi, P.; Vermesh, O.; Grecu, M.; Javey, A.; Wang, O.; Dai, H. J.; Peng, S.; Cho, K. J. *Nano Letters* **2003**, *3*, 347-351.
- (52) Barone, P. W.; Baik, S.; Heller, D. A.; Strano, M. S. *Nature Materials* **2005**, *4*, 86-U16.
- (53) Peng, S.; Cho, K. J. *Nano Letters* **2003**, *3*, 513-517.
- (54) Peng, S.; Cho, K. J.; Qi, P. F.; Dai, H. J. *Chemical Physics Letters* **2004**, *387*, 271-276.
- (55) Collins, P. G.; Bradley, K.; Ishigami, M.; Zettl, A. *Science* **2000**, *287*, 1801-1804.
- (56) Chopra, S.; McGuire, K.; Gothard, N.; Rao, A. M.; Pham, A. *Applied Physics Letters* **2003**, *83*, 2280-2282.
- (57) Novak, J. P.; Snow, E. S.; Houser, E. J.; Park, D.; Stepnowski, J. L.; McGill, R. A. *Applied Physics Letters* **2003**, *83*, 4026-4028.
- (58) Tournus, F.; Latil, S.; Heggie, M. I.; Charlier, J. C. *Physical Review B* **2005**, *72*, 075431.
- (59) Kong, J.; Franklin, N. R.; Zhou, C. W.; Chapline, M. G.; Peng, S.; Cho, K. J.; Dai, H. J. *Science* **2000**, *287*, 622-625.
- (60) Auvray, S.; Borghetti, J.; Goffman, M. F.; Filoramo, A.; Derycke, V.; Bourgoïn, J. P.; Jost, O. *Applied Physics Letters* **2004**, *84*, 5106-5108.
- (61) Auvray, S.; Derycke, V.; Goffman, M.; Filoramo, A.; Jost, O.; Bourgoïn, J. P. *Nano Letters* **2005**, *5*, 451-455.
- (62) Star, A.; Han, T. R.; Joshi, V.; Gabriel, J. C. P.; Gruner, G. *Advanced Materials* **2004**, *16*, 2049-+.
- (63) Dresselhaus, M. S.; Dresselhaus, G.; Eklund, P. C. *Science of fullerenes and carbon nanotubes*; Academic Press: San Diego, 1996.
- (64) Saito, R.; Dresselhaus, G.; Dresselhaus, M. S. *Physical Properties of Carbon Nanotubes*; Imperial College Press: London, 1998.
- (65) Shim, M.; Javey, A.; Kam, N. W. S.; Dai, H. J. *Journal of the American Chemical Society* **2001**, *123*, 11512-11513.
- (66) Tans, S. J.; Devoret, M. H.; Dai, H. J.; Thess, A.; Smalley, R. E.; Geerligs, L. J.; Dekker, C. *Nature* **1997**, *386*, 474-477.
- (67) Cantalini, C.; Valentini, L.; Armentano, I.; Kenny, J. M.; Lozzi, L.; Santucci, S. *Journal of the European Ceramic Society* **2004**, *24*, 1405-1408.

- (68) Bekyarova, E.; Davis, M.; Burch, T.; Itkis, M. E.; Zhao, B.; Sunshine, S.; Haddon, R. C. *Journal of Physical Chemistry B* **2004**, *108*, 19717-19720.
- (69) Lu, Y. J.; Li, J.; Han, J.; Ng, H. T.; Binder, C.; Partridge, C.; Meyyappan, M. *Chemical Physics Letters* **2004**, *391*, 344-348.
- (70) Snow, E. S.; Perkins, F. K.; Houser, E. J.; Badescu, S. C.; Reinecke, T. L. *Science* **2005**, *307*, 1942-5.
- (71) Han, W. Q.; Cumings, J.; Huang, X. S.; Bradley, K.; Zettl, A. *Chemical Physics Letters* **2001**, *346*, 368-372.
- (72) Snow, E. S.; Perkins, F. K.; Houser, E. J.; Badescu, S. C.; Reinecke, T. L. *Science* **2005**, *307*, 1942-1945.
- (73) Snow, E. S.; Perkins, F. K. *Nano Letters* **2005**, *5*, 2414-2417.
- (74) Staii, C.; Johnson, A. T. *Nano Letters* **2005**, *5*, 1774-1778.
- (75) Robinson, J. A.; Snow, E. S.; Badescu, S. C.; Reinecke, T. L.; Perkins, F. K. *Nano Letters* **2006**, *6*, 1747-1751.
- (76) Lee, C. Y.; Baik, S.; Zhang, J. Q.; Masel, R. I.; Strano, M. S. *Journal of Physical Chemistry B* **2006**, *110*, 11055-11061.
- (77) Bradley, K.; Gabriel, J. C. P.; Star, A.; Gruner, G. *Applied Physics Letters* **2003**, *83*, 3821-3823.
- (78) Zhang, J.; Boyd, A.; Tselev, A.; Paranjape, M.; Barbara, P. *Applied Physics Letters* **2006**, *88*, 123112.
- (79) Nguyen, H. Q.; Huh, J. S. *Sensors and Actuators B-Chemical* **2006**, *117*, 426-430.
- (80) Cattanach, K.; Kulkarni, R. D.; Kozlov, M.; Manohar, S. K. *Nanotechnology* **2006**, *17*, 4123-4128.
- (81) Zhang, T.; Nix, M. B.; Yoo, B. Y.; Deshusses, M. A.; Myung, N. V. *Electroanalysis* **2006**, *18*, 1153-1158.
- (82) Chen, R. J.; Franklin, N. R.; Kong, J.; Cao, J.; Tomblor, T. W.; Zhang, Y. G.; Dai, H. J. *Applied Physics Letters* **2001**, *79*, 2258-2260.
- (83) Masel, R. I. *Principles of adsorption and reaction on solid surfaces*; Wiley: New York, 1996.
- (84) All but one of the responses in Fig. 9a (from Qi et al.) show systematic changes with analyte concentration. Curiously, the 10 ppb response is virtually identical to the 5 ppb case. The data are shown to overlap in Fig 9a, and this causes unexplained discontinuities in the response function (Fig 9b) and its derivative (Fig 9d). For this reason, we limit the discussion to the reported behavior below 10 ppb.
- (85) In Fig 9c, the parameters $S_{max}=0.43$, $k=3.02 \times 10^{-6}/\text{ppt}$ and $K=8.2 \times 10^{-3}/\text{ppt}$ were used as an illustration.
- (86) Novak et al. are unsure of the NH_3 concentration dosed for the data in reproduced in Fig 10b. Using parameters for the DMMP case, one can estimate a value of 100 ppb. This value was used to generate the model curves for comparison.
- (87) Chang, H.; Lee, J. D.; Lee, S. M.; Lee, Y. H. *Applied Physics Letters* **2001**, *79*, 3863-3865.
- (88) Peng, S.; Cho, K. J. *Nanotechnology* **2000**, *11*, 57-60.
- (89) Saito, R.; Dresselhaus, G.; Dresselhaus, M. S. *Physical properties of carbon nanotubes*; Imperial College Press: London, 1998.

- (90) Dresselhaus, M. S.; Dresselhaus, G.; Eklund, P. C. *Science of fullerenes and carbon nanotubes*; Academic Press: San Diego ; London, 1996.
- (91) Heinze, S.; Tersoff, J.; Martel, R.; Derycke, V.; Appenzeller, J.; Avouris, P. *Physical Review Letters* **2002**, *89*, -.
- (92) Krupke, R.; Hennrich, F.; Weber, H. B.; Kappes, M. M.; von Lohneysen, H. *Nano Letters* **2003**, *3*, 1019-1023.
- (93) Baik, S.; Usrey, M.; Rotkina, L.; Strano, M. *Journal of Physical Chemistry B* **2004**, *108*, 15560-15564.
- (94) Response to dichloromethane is either negative or positive in some cases, but the response is small comparing to SOCl₂ response
- (95) Lee, C. Y.; Strano, M. S. *Langmuir* **2005**, *21*, 5192-5196.
- (96) Responses from two different gap sizes are plotted together since they fall on the same line.
- (97) The r² values are 0.937, 0.977, and 0.992 for system 1), 2), and 3) respectively.
- (98) Zhang, Z. B.; Cardenas, J.; Campbell, E. E. B.; Zhang, S. L. *Applied Physics Letters* **2005**, *87*, -.
- (99) 100 ppm SOCl₂ did show slight decrease, but it was not evident enough to explain preferential decrease in Raman feature which are discussed in this work
- (100) Strano, M. S. *Journal of the American Chemical Society* **2003**, *125*, 16148-16153.
- (101) Heller, D. A.; Barone, P. W.; Swanson, J. P.; Mayrhofer, R. M.; Strano, M. S. *Journal of Physical Chemistry B* **2004**, *108*, 6905-6909.
- (102) Strano, M. S.; Dyke, C. A.; Usrey, M. L.; Barone, P. W.; Allen, M. J.; Shan, H. W.; Kittrell, C.; Hauge, R. H.; Tour, J. M.; Smalley, R. E. *Science* **2003**, *301*, 1519-1522.
- (103) Brown, S. D. M.; Jorio, A.; Corio, P.; Dresselhaus, M. S.; Dresselhaus, G.; Saito, R.; Kneipp, K. *Physical Review B* **2001**, *63*, 155414.
- (104) Dettlaff-Weglikowska, U.; Skakalova, V.; Graupner, R.; Jhang, S. H.; Kim, B. H.; Lee, H. J.; Ley, L.; Park, Y. W.; Berber, S.; Tomanek, D.; Roth, S. *Journal of the American Chemical Society* **2005**, *127*, 5125-5131.
- (105) Datta, S. *Nanotechnology* **2004**, *15*, S433-S451.
- (106) Orlikowski, D.; Mehrez, H.; Taylor, J.; Guo, H.; Wang, J.; Roland, C. *Physical Review B* **2001**, *63*, 155414.
- (107) Ferry, D. K.; Goodnick, S. M. *Transport in nanostructures*; Cambridge University Press: Cambridge, U.K. ; New York, 1997.
- (108) a = 1 nm and electron energy of 1 meV, $\phi=2\pi/5$ are assumed in this calculation. Using other values gives a similar trend. See Ferry et al. for detailed calculations.
- (109) Bo, X. Z.; Lee, C. Y.; Strano, M. S.; Goldfinger, M.; Nuckolls, C.; Blanchet, G. B. *Applied Physics Letters* **2005**, *86*, -.
- (110) Hu, L.; Hecht, D. S.; Gruner, G. *Nano Letters* **2004**, *4*, 2513-2517.
- (111) These detection limits are from devices made by deposition of HiPco SWNT suspended in SDS.
- (112) Li, J.; Lu, Y. J.; Ye, Q.; Cinke, M.; Han, J.; Meyyappan, M. *Nano Letters* **2003**, *3*, 929-933.

- (113) Pearson, G. S.; Magee, R. S. *Pure and Applied Chemistry* **2002**, *74*, 187-316.
- (114) Shi, W.; Johnson, J. K. *Physical Review Letters* **2003**, *91*, 015504.
- (115) Bienfait, M.; Zeppenfeld, P.; Dupont-Pavlovsky, N.; Muris, M.; Johnson, M. R.; Wilson, T.; DePies, M.; Vilches, O. E. *Physical Review B* **2004**, *70*, 035410.
- (116) Zambano, A. J.; Talapatra, S.; Migone, A. D. *Physical Review B* **2001**, *64*, 075415.
- (117) Jiang, J. W.; Sandler, S. I. *Physical Review B* **2003**, *68*, 245412.
- (118) Seo, K.; Park, K. A.; Kim, C.; Han, S.; Kim, B.; Lee, Y. H. *Journal of the American Chemical Society* **2005**, *127*, 15724-15729.
- (119) Price, B. K.; Tour, J. M. *Journal of the American Chemical Society* **2006**, *128*, 12899-12904.
- (120) Arrieta, A.; Aizpurua, J. M.; Palomo, C. *Tetrahedron Letters* **1984**, *25*, 3365-3368.
- (121) El-Sakka, I. A.; Hassan, N. A. *Journal of Sulfur Chemistry* **2005**, *26*, 33-97.
- (122) Ghosh, M. *Polymer Bulletin* **1988**, *19*, 1-6.
- (123) Bernstein, P. A.; Lever, A. B. P. *Inorganic Chemistry* **1995**, *34*, 933-937.
- (124) Dampier, F. W.; Cole, T. A. *Journal of the Electrochemical Society* **1987**, *134*, 2383-2387.
- (125) Luo, N.; Stewart, M. J.; Hirt, D. E.; Husson, S. M.; Schwark, D. W. *Journal of Applied Polymer Science* **2004**, *92*, 1688-1694.
- (126) Waqif, M.; Saad, A. M.; Bensitel, M.; Bachelier, J.; Saur, O.; Lavalley, J. C. *Journal of the Chemical Society-Faraday Transactions* **1992**, *88*, 2931-2936.
- (127) Morenocastilla, C.; Carrascomarin, F.; Utreraidalgo, E.; Riverautila, J. *Langmuir* **1993**, *9*, 1378-1383.
- (128) Kukovecz, A.; Kramberger, C.; Georgakilas, V.; Prato, M.; Kuzmany, H. *European Physical Journal B* **2002**, *28*, 223-230.
- (129) SOCl₂ was not utilized for this purpose. Although SOCl₂ is a nerve and blister agent simulant, its corrosive properties made it impractical for use in a more expensive injector apparatus associated with a commercial mass spectrometer.
- (130) Bansal, L.; El-Sherif, M. *Ieee Sensors Journal* **2005**, *5*, 648-655.
- (131) Jiang, J. W.; Sandler, S. I.; Schenk, M.; Smit, B. *Physical Review B* **2005**, *72*, 045447.
- (132) Rappe, A. K.; Casewit, C. J.; Colwell, K. S.; Goddard, W. A.; Skiff, W. M. *Journal of the American Chemical Society* **1992**, *114*, 10024-10035.
- (133) Gasteiger, J.; Marsili, M. *Tetrahedron* **1980**, *36*, 3219-3228.
- (134) Accelry <http://www.accelrys.com/products/cerius2/>
- (135) Vanderhoff, G. R.; Vanzoonen, P.; Grob, K. *Hrc-Journal of High Resolution Chromatography* **1994**, *17*, 37-42.
- (136) Berneche, S.; Roux, B. *Nature* **2001**, *414*, 73-77.
- (137) Zhou, Y. F.; Morais-Cabral, J. H.; Kaufman, A.; MacKinnon, R. *Nature* **2001**, *414*, 43-48.
- (138) Ho, C.; Qiao, R.; Heng, J. B.; Chatterjee, A.; Timp, R. J.; Aluru, N. R.; Timp, G. *Proceedings of the National Academy of Sciences of the United States of America* **2005**, *102*, 10445-10450.

- (139) Zhang, B.; Wood, M.; Lee, H. *Analytical Chemistry* **2009**, *81*, 5541-5548.
- (140) Heng, J. B.; Dimitrov, V.; Grinkova, Y. V.; Ho, C.; Kim, T.; Muller, D.; Sligar, S.; Sorsch, T.; Twesten, R.; Timp, R.; Timp, G. *2003 Ieee International Electron Devices Meeting, Technical Digest* **2003**, 767-770
1000.
- (141) Heng, J. B.; Ho, C.; Kim, T.; Timp, R.; Aksimentiev, A.; Grinkova, Y. V.; Sligar, S.; Schulten, K.; Timp, G. *Biophysical Journal* **2004**, *87*, 2905-2911.
- (142) Wanunu, M.; Sutin, J.; McNally, B.; Chow, A.; Meller, A. *Biophysical Journal* **2008**, *95*, 4716-4725.
- (143) Robertson, J. W. F.; Rodrigues, C. G.; Stanford, V. M.; Rubinson, K. A.; Krasilnikov, O. V.; Kasianowicz, J. J. *Proceedings of the National Academy of Sciences of the United States of America* **2007**, *104*, 8207-8211.
- (144) Branton, D.; Deamer, D. W.; Marziali, A.; Bayley, H.; Benner, S. A.; Butler, T.; Di Ventra, M.; Garaj, S.; Hibbs, A.; Huang, X. H.; Jovanovich, S. B.; Krstic, P. S.; Lindsay, S.; Ling, X. S. S.; Mastrangelo, C. H.; Meller, A.; Oliver, J. S.; Pershin, Y. V.; Ramsey, J. M.; Riehn, R.; Soni, G. V.; Tabard-Cossa, V.; Wanunu, M.; Wiggin, M.; Schloss, J. A. *Nature Biotechnology* **2008**, *26*, 1146-1153.
- (145) Sakmann, B.; Neher, E. *Single-channel recording*; 2nd ed.; Plenum Press: New York, 1995.
- (146) Gration, K. A. F.; Lambert, J. J.; Ramsey, R. L.; Rand, R. P.; Usherwood, P. N. R. *Nature* **1982**, *295*, 599-601.
- (147) Benzi, R.; Sutera, A.; Vulpiani, A. *Journal of Physics a-Mathematical and General* **1981**, *14*, L453-L457.
- (148) Gammaitoni, L.; Hanggi, P.; Jung, P.; Marchesoni, F. *Reviews of Modern Physics* **1998**, *70*, 223-287.
- (149) Bulsara, A. R.; Gammaitoni, L. *Physics Today* **1996**, *49*, 39-45.
- (150) Hanggi, P. *Chemphyschem* **2002**, *3*, 285-290.
- (151) Douglass, J. K.; Wilkens, L.; Pantazelou, E.; Moss, F. *Nature* **1993**, *365*, 337-340.
- (152) Levin, J. E.; Miller, J. P. *Nature* **1996**, *380*, 165-168.
- (153) Russell, D. F.; Wilkens, L. A.; Moss, F. *Nature* **1999**, *402*, 291-294.
- (154) Bezrukov, S. M.; Vodyanoy, I. *Nature* **1995**, *378*, 362-364.
- (155) Hidaka, I.; Nozaki, D.; Yamamoto, Y. *Physical Review Letters* **2000**, *85*, 3740-3743.
- (156) Simonotto, E.; Riani, M.; Seife, C.; Roberts, M.; Twitty, J.; Moss, F. *Physical Review Letters* **1997**, *78*, 1186-1189.
- (157) Whitby, M.; Quirke, N. *Nature Nanotechnology* **2007**, *2*, 87-94.
- (158) Regan, B. C.; Aloni, S.; Ritchie, R. O.; Dahmen, U.; Zettl, A. *Nature* **2004**, *428*, 924-927.
- (159) Barreiro, A.; Rurali, R.; Hernandez, E. R.; Moser, J.; Pichler, T.; Forro, L.; Bachtold, A. *Science* **2008**, *320*, 775-778.
- (160) Yum, K.; Yu, M. F. *Physical Review Letters* **2005**, *95*, -.
- (161) Striolo, A. *Nano Letters* **2006**, *6*, 633-639.
- (162) Alexiadis, A.; Kassinos, S. *Chemical Reviews* **2008**, *108*, 5014-5034.
- (163) Hummer, G.; Rasaiah, J. C.; Noworyta, J. P. *Nature* **2001**, *414*, 188-190.
- (164) Ugarte, D.; Chatelain, A.; deHeer, W. A. *Science* **1996**, *274*, 1897-1899.

- (165) Ajayan, P. M.; Ebbesen, T. W.; Ichihashi, T.; Iijima, S.; Tanigaki, K.; Hiura, H. *Nature* **1993**, *362*, 522-525.
- (166) Majumder, M.; Chopra, N.; Andrews, R.; Hinds, B. J. *Nature* **2005**, *438*, 930-930.
- (167) Fornasiero, F.; Park, H. G.; Holt, J. K.; Stadermann, M.; Grigoropoulos, C. P.; Noy, A.; Bakajin, O. *Proceedings of the National Academy of Sciences of the United States of America* **2008**, *105*, 17250-17255.
- (168) Kim, B. M.; Sinha, S.; Bau, H. H. *Nano Letters* **2004**, *4*, 2203-2208.
- (169) Waghe, A.; Rasaiah, J. C.; Hummer, G. *Journal of Chemical Physics* **2002**, *117*, 10789-10795.
- (170) Joseph, S.; Aluru, N. R. *Nano Letters* **2008**, *8*, 452-458.
- (171) Agmon, N. *Chemical Physics Letters* **1995**, *244*, 456-462.
- (172) Dellago, C.; Naor, M. M.; Hummer, G. *Physical Review Letters* **2003**, *90*, -.
- (173) Koga, K.; Gao, G. T.; Tanaka, H.; Zeng, X. C. *Nature* **2001**, *412*, 802-805.
- (174) Kobayashi, C.; Saito, S. J.; Ohmine, I. *Journal of Chemical Physics* **2000**, *113*, 9090-9100.
- (175) Smith, B. W.; Monthieux, M.; Luzzi, D. E. *Nature* **1998**, *396*, 323-324.
- (176) Guan, L. H.; Suenaga, K.; Shi, Z. J.; Gu, Z. N.; Iijima, S. *Physical Review Letters* **2005**, *94*, -.
- (177) Sun, B. Y.; Sato, Y.; Suenaga, K.; Okazaki, T.; Kishi, N.; Sugai, T.; Bandow, S.; Iijima, S.; Shinohara, H. *Journal of the American Chemical Society* **2005**, *127*, 17972-17973.
- (178) Ito, T.; Sun, L.; Crooks, R. M. *Analytical Chemistry* **2003**, *75*, 2399-2406.
- (179) Ito, T.; Sun, L.; Henriquez, R. R.; Crooks, R. M. *Accounts of Chemical Research* **2005**, *38*, 687-687.
- (180) Fan, R.; Karnik, R.; Yue, M.; Li, D. Y.; Majumdar, A.; Yang, P. D. *Nano Letters* **2005**, *5*, 1633-1637.
- (181) Somada, H.; Hirahara, K.; Akita, S.; Nakayama, Y. *Nano Letters* **2009**, *9*, 62-65.
- (182) Begtrup, G. E.; Gannett, W.; Yuzvinsky, T. D.; Crespi, V. H.; Zettl, A. *Nano Letters* **2009**, *9*, 1835-1838.
- (183) Harrison, D. J.; Fluri, K.; Seiler, K.; Fan, Z. H.; Effenhauser, C. S.; Manz, A. *Science* **1993**, *261*, 895-897.
- (184) Weinberger, R. *Practical capillary electrophoresis*; 2nd ed.; Academic Press: San Diego, Calif. ; London, 2000.
- (185) Qiao, R.; Aluru, N. R. *Nano Letters* **2003**, *3*, 1013-1017.
- (186) Chen, Y. F.; Ni, Z. H.; Wang, G. M.; Xu, D. Y.; Li, D. Y. *Nano Letters* **2008**, *8*, 42-48.
- (187) Miller, S. A.; Young, V. Y.; Martin, C. R. *Journal of the American Chemical Society* **2001**, *123*, 12335-12342.
- (188) Miller, S. A.; Martin, C. R. *Journal of Electroanalytical Chemistry* **2002**, *522*, 66-69.
- (189) Heslot, F.; Fraysse, N.; Cazabat, A. M. *Nature* **1989**, *338*, 640-642.
- (190) Brochard, F. *Journal of Chemical Physics* **1986**, *84*, 4664-4672.

- (191) Malliani, A.; Pagani, M.; Lombardi, F.; Cerutti, S. *Circulation* **1991**, *84*, 482-492.
- (192) Campbell, S. S.; Murphy, P. J. *Science* **1998**, *279*, 396-399.
- (193) Steriade, M.; McCormick, D. A.; Sejnowski, T. J. *Science* **1993**, *262*, 679-685.
- (194) Post, E.; Forchhammer, M. C. *Nature* **2002**, *420*, 168-171.
- (195) Glass, L. *Nature* **2001**, *410*, 277-284.
- (196) Iijima, S.; Ichihashi, T. *Nature* **1993**, *363*, 603-605.
- (197) Koshino, M.; Tanaka, T.; Solin, N.; Suenaga, K.; Isobe, H.; Nakamura, E. *Science* **2007**, *316*, 853-853.
- (198) Majumder, M.; Chopra, N.; Andrews, R.; Hinds, B. J. *Nature* **2005**, *438*, 44-44.
- (199) Beckstein, O.; Tai, K.; Sansom, M. S. P. *Journal of the American Chemical Society* **2004**, *126*, 14694-14695.
- (200) Lin, C. H.; Lee, G. B.; Chang, B. W.; Chang, G. L. *Journal of Micromechanics and Microengineering* **2002**, *12*, 590-597.
- (201) Kasianowicz, J. J.; Robertson, J. W. F.; Chan, E. R.; Reiner, J. E.; Stanford, V. M. *Annual Review of Analytical Chemistry* **2008**, *1*, 737-766.
- (202) He, Y.; Gillespie, D.; Boda, D.; Vlassiouk, I.; Eisenberg, R. S.; Siwy, Z. S. *Journal of the American Chemical Society* **2009**, *131*, 5194-5202.
- (203) Vermesh, U.; Choi, J. W.; Vermesh, O.; Fan, R.; Nagaraj, J.; Heath, J. R. *Nano Letters* **2009**, *9*, 1315-1319.
- (204) Song, C.; Corry, B. *Journal of Physical Chemistry B* **2009**, *113*, 7642-7649.
- (205) Liu, H. M.; Murad, S.; Jameson, C. J. *Journal of Chemical Physics* **2006**, *125*, -.
- (206) Corry, B. *Journal of Physical Chemistry B* **2008**, *112*, 1427-1434.
- (207) Wong, S. S.; Joselevich, E.; Woolley, A. T.; Cheung, C. L.; Lieber, C. M. *Nature* **1998**, *394*, 52-55.
- (208) Powell, M. R.; Sullivan, M.; Vlassiouk, I.; Constantin, D.; Sudre, O.; Martens, C. C.; Eisenberg, R. S.; Siwy, Z. S. *Nature Nanotechnology* **2008**, *3*, 51-57.
- (209) Smeets, R. M. M.; Keyser, U. F.; Wu, M. Y.; Dekker, N. H.; Dekker, C. *Physical Review Letters* **2006**, *97*, -.
- (210) Liu, H.; Qian, S. Z.; Bau, H. H. *Biophysical Journal* **2007**, *92*, 1164-1177.
- (211) Liu, L.; Chen, X.; Lu, W. Y.; Han, A. J.; Qiao, Y. *Physical Review Letters* **2009**, *102*, -.
- (212) McGeoch, J. E. M.; Guidotti, G. *Journal of Biological Chemistry* **1992**, *267*, 832-841.
- (213) McGeoch, J. E. M.; Guidotti, G. *Brain Research* **1997**, *766*, 188-194.
- (214) Henkel, A. W.; Meiri, H.; Horstmann, H.; Lindau, M.; Almers, W. *EMBO Journal* **2000**, *19*, 84-93.
- (215) Pisani, L.; Valentini, M.; Hofmann, D. H.; Kuleshova, L. N.; D'Aguzzo, B. *Solid State Ionics* **2008**, *179*, 465-476.
- (216) Gillespie, D. T. *Journal of Physical Chemistry* **1977**, *81*, 2340-2361.
- (217) Bratsun, D.; Volfson, D.; Tsimring, L. S.; Hasty, J. *Proceedings of the National Academy of Sciences of the United States of America* **2005**, *102*, 14593-14598.

(218) Karnik, R.; Fan, R.; Yue, M.; Li, D. Y.; Yang, P. D.; Majumdar, A. *Nano Letters* **2005**, *5*, 943-948.

(219) Siwy, Z.; Heins, E.; Harrell, C. C.; Kohli, P.; Martin, C. R. *Journal of the American Chemical Society* **2004**, *126*, 10850-10851.